

**Diffractively produced Z bosons in the muon decay channel in  
p $\bar{p}$  collisions at  $\sqrt{s} = 1.96$  TeV, and the measurement of the  
efficiency of the DØ Run II Luminosity Monitor**

A thesis submitted to the University of Manchester for the degree of Doctor of  
Philosophy in the Faculty of Engineering and Physical Sciences

2006

Tamsin Edwards

School of Physics and Astronomy

# Contents

<b>1</b>	<b>Introduction</b>	<b>16</b>
<b>2</b>	<b>Diffractive Scattering and the Pomeron</b>	<b>19</b>
2.1	Regge Theory . . . . .	20
2.1.1	Some concepts used in Regge theory . . . . .	21
2.1.2	Scattering amplitude . . . . .	23
2.1.3	Regge trajectories . . . . .	24
2.1.4	Total scattering cross section . . . . .	28
2.1.5	The pomeron . . . . .	28
2.2	Diffractive Scattering . . . . .	31
2.2.1	Rapidity gaps . . . . .	32
2.2.2	Previous analyses of diffractive <b>W/Z</b> boson production . .	33
2.2.3	Fractional momentum loss of the proton . . . . .	34
2.3	Simulation of diffractive <b>Z</b> boson production . . . . .	35
2.3.1	Rapidity gap survival . . . . .	39
<b>3</b>	<b>The DØ Experiment at the Tevatron</b>	<b>41</b>
3.1	The Tevatron Accelerator . . . . .	41
3.2	The DØ Detector . . . . .	45
3.2.1	Tracking system . . . . .	46
3.2.2	Preshower detectors . . . . .	49

3.2.3	Calorimeter . . . . .	49
3.2.4	Luminosity Monitor . . . . .	56
3.2.5	Muon detector system . . . . .	57
3.2.6	Forward Proton Detector . . . . .	59
3.3	Triggering . . . . .	60
<b>4</b>	<b>Efficiency of the Luminosity Monitor</b>	<b>62</b>
4.1	LM And/Or Terms . . . . .	63
4.2	Cross Sections and Luminosity . . . . .	64
4.2.1	Inelastic $p\bar{p}$ cross section . . . . .	66
4.2.2	LM acceptance . . . . .	68
4.3	LM Efficiency . . . . .	69
4.3.1	Detector efficiencies . . . . .	70
4.3.2	Parameter variation . . . . .	76
4.3.3	Combined detector efficiency . . . . .	81
4.3.4	Classification efficiency . . . . .	81
<b>5</b>	<b>Analysis of Diffractive <math>Z \rightarrow \mu^+\mu^-</math> Interactions</b>	<b>89</b>
5.1	Z Boson Candidate Selection . . . . .	90
5.1.1	Dataset . . . . .	90
5.1.2	Selection Criteria . . . . .	90
5.2	Reconstructing the Momentum Loss . . . . .	93
5.2.1	Muon information . . . . .	96
5.2.2	Calorimeter information . . . . .	97
5.3	POMWIG simulation of diffractive $Z \rightarrow \mu^+\mu^-$ . . . . .	102
5.3.1	Acceptance cuts . . . . .	105
5.4	Rapidity Gap Requirement . . . . .	106
5.4.1	Choice of event kinematics . . . . .	108

5.5	Momentum Loss Correction . . . . .	110
5.6	Components of the Cross Section . . . . .	119
5.6.1	Number of candidates . . . . .	122
5.6.2	Systematic investigations . . . . .	123
5.6.3	Efficiency of rapidity gap requirement . . . . .	131
5.6.4	Efficiency of muon detection . . . . .	134
5.6.5	Cosmic muon background . . . . .	135
5.6.6	Other efficiencies and backgrounds . . . . .	137
5.7	Result . . . . .	138
5.7.1	Corrected number of candidates . . . . .	138
5.7.2	Contribution from non-diffractive events . . . . .	139
5.8	Discussion . . . . .	140
<b>6</b>	<b>Summary</b>	<b>146</b>
<b>A</b>	<b>Diffractive Scattering at DØ</b>	<b>147</b>
A.1	Introduction . . . . .	147
A.2	Diffractive <b>Z</b> boson production . . . . .	148
A.2.1	Event selection and data analysis . . . . .	148
A.2.2	Results . . . . .	150

# List of Figures

2.1	Crossing symmetry between (a) $s$ -channel and (b) crossed $t$ -channel processes . . . . .	22
2.2	Chew-Frautschi plot of resonances in $\pi^-\pi^0 \rightarrow \bar{p}n$ scattering [14] .	25
2.3	Relationship between $s$ and $t$ channel processes in the $J - t$ plane	26
2.4	Chew-Frautschi plot of $\pi^-p \rightarrow \pi^0n$ scattering [14] . . . . .	27
2.5	Total cross section for $p\bar{p}$ (upper curve) and $pp$ scattering as a function of centre of mass energy [24] . . . . .	29
2.6	POMWIG uses the factorisation model of single diffraction [33] .	36
2.7	Leading order and next-to-leading order diagrams for diffractive Z boson production . . . . .	38
3.1	The Fermilab accelerator complex . . . . .	42
3.2	The Tevatron beam structure, showing the three superbunches each with 12 bunches . . . . .	44
3.3	Diagram of the DØ detector . . . . .	45
3.4	The central tracking system, consisting of the silicon microstrip tracker, central fiber tracker and solenoid magnet. Other detectors are also shown. . . . .	47
3.5	The silicon microstrip tracker . . . . .	47
3.6	The calorimeter (quarter cut-away view) . . . . .	51
3.7	Projection of the calorimeter towers in the $ieta - layer$ plane . . .	53
3.8	A typical calorimeter cell . . . . .	54

3.9	One detector of the Luminosity Monitor ( $r$ - $\phi$ view), showing the scintillator wedges, photomultiplier tubes and central beam pipe . . . . .	56
3.10	Exploded view of the muon tracking chambers . . . . .	59
4.1	Diagrams of single diffraction and double diffraction . . . . .	67
4.2	$E_{\text{sum}}$ for the efficient sample $N \cdot S$ . . . . .	72
4.3	$E_{\text{sum}}$ for the inefficient+SD samples (a) $\overline{N} \cdot S$ and (b) $N \cdot \overline{S}$ and the noise sample $\overline{N} \cdot \overline{S}$ , normalised at the first bin. . . . .	73
4.4	$E_{\text{sum}}$ for the (a) North and (b) South subtracted histograms. The fit function is the sum of two exponentials, in the range 1.5-20 GeV. One exponential is shown as a dashed line. . . . .	75
4.5	Effect of parameter variations on North and South detector efficiencies . . . . .	78
4.6	Effect of varying fit range and integration boundary on the lower limits of the North and South detector efficiencies . . . . .	79
4.7	Single detector efficiency limits as a function of time . . . . .	80
4.8	$E_{\text{sum}}$ for the $N \cdot S \cdot \overline{FastZ}$ sample and the normalised efficient sample, $N \cdot S \cdot FastZ$ . . . . .	83
4.9	$E_{\text{sum}}$ for the $N \cdot S \cdot PHalo$ sample and the normalised efficient sample, $N \cdot S \cdot FastZ$ . . . . .	85
4.10	$E_{\text{sum}}$ for the $N \cdot S \cdot AHalo$ sample and the normalised efficient sample, $N \cdot S \cdot FastZ$ . . . . .	86
4.11	$E_{\text{sum}}$ for the $N \cdot S \cdot none$ sample and the normalised efficient sample, $N \cdot S \cdot FastZ$ . . . . .	87
5.1	$Z \rightarrow \mu^+ \mu^-$ candidate events, showing the (a) pseudorapidity, with two entries per event, and (b) invariant mass of the two highest $p_T$ muons . . . . .	94
5.2	$Z \rightarrow \mu^+ \mu^-$ candidate events, showing the (a) rapidity and (b) transverse momentum of the $Z$ boson candidate . . . . .	95
5.3	Transverse momentum of muons not associated with the $Z$ boson decay that are at least loose quality with a matched track in the central tracking detector . . . . .	96

5.4	Cell energies in the range $-2.6 < \eta < 0$ in the layers (a) EM1 and (b) CH1 for empty bunch crossing, minimum bias and dijet events. The distributions are normalised to unity. . . . .	98
5.5	Cell energy in the EM1 layer for empty BX events before hot cell killing is performed. The layers are divided into four regions, with boundaries at $\eta = 0$ (North-South) and $ \eta  = 3.2$ (Central-Forward) . . . . .	100
5.6	Cell energy in the EM1 layer for empty BX events after hot cell killing is performed. The layers are divided into four regions, with boundaries at $\eta = 0$ (North-South) and $ \eta  = 3.2$ (Central-Forward) . . . . .	101
5.7	Energy of cells in all $Z \rightarrow \mu^+\mu^-$ events, before the threshold is applied . . . . .	102
5.8	Observed momentum loss $\xi_{obs}$ in all $Z \rightarrow \mu^+\mu^-$ events . . . . .	103
5.9	Fraction of the observed momentum loss contributed by the muons, in all $Z \rightarrow \mu^+\mu^-$ events . . . . .	103
5.10	Average momentum loss $\xi_{obs}$ versus (a) number of vertices and (b) instantaneous luminosity in all $Z \rightarrow \mu^+\mu^-$ events . . . . .	107
5.11	Pseudorapidity of most forward particle in POMWIG $Z \rightarrow \mu^+\mu^-$ events with (a) $\xi < 0.05$ and (b) $\xi < 0.03$ . . . . .	109
5.12	Pseudorapidity of most forward particle in POMWIG $Z \rightarrow \mu^+\mu^-$ events with (a) $\xi < 0.02$ and (b) $\xi < 0.01$ . . . . .	109
5.13	Observed momentum loss $\xi_{obs}$ in $Z \rightarrow \mu^+\mu^-$ events with a rapidity gap. The POMWIG prediction is shown, scaled to the data distribution. . . . .	111
5.14	Pseudorapidity of most forward cell in $Z \rightarrow \mu^+\mu^-$ events with momentum loss $\xi_{obs} < 0.02$ , where the antiproton-side distribution is reversed and added to the proton distribution. The POMWIG prediction is also shown, scaled to the data distribution, which includes a requirement that particles are within $ \eta  < 4.45$ . . . . .	112
5.15	POMWIG prediction for the fraction of true beam $\xi$ which is reconstructed in the detector, $\xi_{reco}/\xi$ , as a function of $\xi_{reco}$ . . . . .	114
5.16	Momentum loss in $Z \rightarrow \mu^+\mu^-$ events with a rapidity gap . . . . .	115

5.17	Average momentum loss versus (a) number of vertices and (b) instantaneous luminosity in $Z \rightarrow \mu^+\mu^-$ events with a rapidity gap .	116
5.18	Diffraction candidate event, showing the (a) calorimeter in $\eta$ - $\phi$ view, with muons superimposed, and the (b) calorimeter and central tracking in side view, where the outgoing proton direction is towards the right of the figure . . . . .	118
5.19	Fraction of the momentum loss $\xi_{obs}$ contributed by the muons, in diffractive $Z \rightarrow \mu^+\mu^-$ candidate events . . . . .	119
5.20	Diffractive $Z \rightarrow \mu^+\mu^-$ candidate events, showing the (a) pseudorapidity of each muon and (b) invariant mass of the $Z$ boson candidate. The POMWIG prediction is shown, scaled to the data distribution. . . . .	120
5.21	Diffractive $Z \rightarrow \mu^+\mu^-$ candidate events, showing the (a) rapidity and (b) transverse momentum of the $Z$ boson candidate. The POMWIG prediction is shown, scaled to the data distribution. . .	121
5.22	Difference in $ieta$ between the two most forward cells in all $Z \rightarrow \mu^+\mu^-$ events . . . . .	126
5.23	Difference in $ieta$ between the two most forward cells in $Z \rightarrow \mu^+\mu^-$ events with a rapidity gap . . . . .	127
5.24	Average momentum loss versus (a) number of vertices and (b) instantaneous luminosity in $Z \rightarrow \mu^+\mu^-$ events with a rapidity gap, in which the most forward cell is excluded from the analysis . . .	129
5.25	Balance of transverse momentum, $p_T^Z - p_T^{hadrons}$ , for diffractive candidate events, where the hadron $p_T$ is measured with the calorimeter cells. The POMWIG prediction is shown, scaled to the data distribution. . . . .	132
5.26	Pseudorapidity of two highest $p_T$ muons in POMWIG $Z \rightarrow \mu^+\mu^-$ events with $\xi < 0.02$ : the geometric acceptance of the muon detector is approximately $ \eta  < 2$ . . . . .	136
5.27	Acolinearity of the dimuon pair in diffractive $Z \rightarrow \mu^+\mu^-$ candidate events . . . . .	137
5.28	Reconstructed $\xi$ distribution in PYTHIA non-diffractive $Z \rightarrow \mu^+\mu^-$ events . . . . .	140



A.1	Log of energy sum in the outgoing antiproton direction ( $-5.3 < \eta < -2.6$ ), comparing events with no visible interactions with events in which both protons dissociate. Areas are normalised to unity. An energy sum cut is applied at 10 GeV for rapidity gap candidates. . . . .	150
A.2	The dimuon invariant mass distribution for Z boson candidates with (a) no rapidity gap and (b) a single rapidity gap. A rapidity gap is defined as one LM detector off and energy sum less than 10 GeV in the same region (see text for details). . . . .	151

# List of Tables

2.1	The default parameters in POMWIG . . . . .	37
3.1	Pseudorapidity coordinate $ieta$ in the calorimeter . . . . .	52
4.1	Luminosity Monitor L1 And/Or terms . . . . .	64
4.2	LM detector acceptances for different components of the inelastic $p\bar{p}$ cross section. The uncertainties are assigned according to the various predictions of the Monte Carlos used [50]. . . . .	69
4.3	Summary of event samples . . . . .	71
4.4	Classification efficiencies measured using various fit ranges . . . .	84
4.5	Efficiencies due to events being misclassified as <i>PHalo</i> , <i>AHalo</i> or <i>none</i> . . . . .	84
5.1	Effect of hot cell killing on the number of rapidity gap candidates, in runs where hot cell killing is available . . . . .	124
5.2	Effect of varying the data cell energy threshold, $E_{data}$ , and the MC particle energy threshold, $E_{MC}$ , on the number of candidates $N_{corr}$ , with the percentage change shown in the final column. . . . .	130
5.3	Efficiencies and backgrounds taken from the inclusive $Z \rightarrow \mu^+\mu^-$ cross section . . . . .	138

# Abstract

The first analysis of diffractively produced  $Z$  bosons in the muon decay channel is presented, using data taken by the DØ detector at the Tevatron at  $\sqrt{s} = 1.96$  TeV. The data sample corresponds to an integrated luminosity of  $109 \text{ pb}^{-1}$ .

The diffractive sample is defined using the fractional momentum loss  $\xi$  of the intact proton or antiproton measured using the calorimeter and muon detector systems. In a sample of 10791  $(Z/\gamma)^* \rightarrow \mu^+\mu^-$  events, 24 diffractive candidate events are found with  $\xi < 0.02$ .

The first work towards measuring the cross section times branching ratio for diffractive production of  $(Z/\gamma)^* \rightarrow \mu^+\mu^-$  is presented for the kinematic region  $\xi < 0.02$ . The systematic uncertainties are not yet sufficiently understood to present the cross section result.

In addition, the first measurement of the efficiency of the Run II DØ Luminosity Monitor is presented, which is used in all cross section measurements. The efficiency is:

$$\varepsilon_{LM} = (90.9 \pm 1.8)\% .$$

# Declaration

No portion of the author's work described in this thesis has been submitted in support of an application for another degree or qualification in this, or any other, institute of learning.

# Copyright Statement

(i) Copyright in text of this thesis rests with the Author. Copies (by any process) either in full, or of extracts, may be made **only** in accordance with instructions given by the Author and lodged in the John Rylands University Library of Manchester. Details may be obtained from the Librarian. This page must form part of any such copies made. Further copies (by any process) of copies made in accordance with such instructions may not be made without the permission (in writing) of the Author.

(ii) The ownership of any intellectual property rights which may be described in this thesis is vested in the University of Manchester, subject to any prior agreement to the contrary, and may not be made available for use by third parties without the written permission of the University, which will prescribe the terms and conditions of any such agreement.

(iii) Further information on the conditions under which disclosures and exploitation may take place is available from the Head of School of Physics and Astronomy.

# Acknowledgements

I'd like to thank my supervisor Brian Cox, for being inspiring and fun to work with, and for the energy, excitement and bright ideas that kept me going through the final stages. Thanks to my 'surrogate' supervisor Andrew Brandt for treating me as one of his own, giving me huge amounts of advice and support, and generally being a lovely person to work with. Thanks to my other supervisor Terry Wyatt for explaining everything so clearly and giving me good physics advice.

Many members of DØ took time to help me despite their own hectic schedules. From my time with the Luminosity group, thanks to Brendan for being a warm person with sound advice and for propping me up at that poster session; thanks to Michael Begel, for taking time to explain things and give my work such thorough attention; and thanks to Heidi Schellman, Rich Partridge, Michelle, Tim and Sahal for general help and silliness in meetings. In the QCD and diffractive groups, I'd like to thank Drew Alton for his reliability and practical help; Christophe Royon, for good ideas; and Duncan Brown for his advice and support. A big thanks to Martijn Mulders, for taking an interest in my analysis, working hard on it, and being incredibly enthusiastic when we took it to Brazil. Thanks to Markus Wobisch, Marco Verzocchi, Jan Stark, Krisztian Peters, and everyone else from DØ that contributed.

Thanks to my Manchester friends: Michiel Sanders, for endless code debugging but mostly for helping me with the Fermi Singers; Simon Dean for many great chats and giving advice and lifts without hesitation; Paul Telford, for being funny and helping me out; and a huge thanks to James Monk, who I leaned on a lot during the final stages and who gave me help, hard work and lovely cups of tea.

Thanks to Stefan Söldner-Rembold for giving me enormously useful advice, support and editorial checking at the end. And special thanks to Gavin Hesketh, who gave me physics help beyond the call of duty and a lot of very happy memories.

I'd also like to thank Fred Loebinger, who was a reason for me coming to Manchester and then staying so long: thanks for being warm, energetic, encouraging and giving so much. Thanks to the other Manchester staff for being friendly, and always ready to chat or to help a confused student.

Thanks to PPARC for the funding, and to all the PPARC staff that helped with everything over the years.

Thanks to Smudge, for being there for me with tea or gin when I needed it. Thanks to Amber, for amazing talks, warm friendship and silliness. Thanks to Martin, for cheering me up and getting me to do so much in Chicago. Thanks Dustin, for being a kindred spirit and making me laugh all the time. Thanks to Matt, for being so lovely and so silly. Thanks to the rest of the Fermiposse and beyond, who have all given me fun, sanity in desperate times, and practical help: Stephen, Marilyn, Nicola, Aidan, Helen, Philip P, Lucio, Ben, Kyle, Simon W, Lydia, Anant, Sam, Kathy, Kirby, Lenka and many others. Thanks to the Brazilian girls (*'as meninas'*), Helena, Renata and Ana, for being sweet friends that I wish I'd got to know more. Thanks to the Fermi Singers for giving me support and enthusiasm during one of the most challenging, rewarding times in my life. Thanks to Adam, for cartwheels in the street and being a thoughtful and important friend. Thanks to Sarah and Claire, for being a massive part of my life, to Matt Green for cups of tea and loyal friendship, and to Linda for being a sweetheart. And special thanks to Emily, for being fun and brilliant, perceptive and caring, and helping me in so many ways.

Thanks to Mum, for making me happy and being enthusiastic about everything I do; to Damian, for being inspiring; to Dad for getting interested in quantum physics and saying all the right things; to Kate for being a good friend and to Tristan for asking me about bosons.

Thanks to Jon, who helped me through my dark days and made everything into something worth smiling about.

# Chapter 1

## Introduction

Historically, electron-proton colliders have been at the forefront of probing the nature of the proton. The parton distribution functions (pdfs) of the proton, which form an essential part of experimental knowledge at hadron colliders, are derived primarily from the high precision measurements of deep inelastic electron-proton scattering at HERA [1, 2]. It is also possible to define *diffractive* parton distributions of the proton: these have the added constraint that the proton remains intact after the collision [3]. The diffractive pdfs have been extracted from diffractive deep inelastic scattering data at HERA [4, 5]; at the H1 experiment, they were extracted under the assumption of Regge factorisation (Section 2).

Transferring the diffractive pdfs to the Tevatron has not been straightforward because factorisation does not hold in hadron-hadron (in this case proton-antiproton) collisions. This breakdown in factorisation, often termed ‘gap survival probability’, is generally understood to be due to multi-parton interactions destroying the outgoing intact proton, and it results in much lower observed rates for diffractive



processes than would be expected from the HERA measurements [6]. Understanding diffractive scattering, and the nature of the factorisation breakdown, is of interest in its own right. In addition, diffractive scattering has been suggested as a powerful tool for searching for new physics at the LHC [7, 8, 9], so a better understanding of the way in which the diffractive pdfs at HERA can be interpreted at hadron-hadron colliders is becoming even more important.

Understanding diffractive scattering at hadron colliders requires the measurement of as many diffractive production processes as possible. One of the cleanest but most rare diffractive processes is  $Z$  boson production. Unlike diffractive  $W$  boson production, which has a larger cross section, diffractive  $Z$  boson production was not unambiguously observed in the Tevatron Run I data. Eight candidate events were seen at DØ [10], and no observation was published at CDF. All previous Tevatron analyses have relied on the observation of rapidity gaps, which are large regions in the event with no particles, and the results have been expressed in terms of the gap fraction: the fraction of events of a particular type with a rapidity gap. In this thesis the first definitive observation of diffractive  $Z$  production is made, using data taken by the DØ experiment, and the first steps are taken towards measuring a diffractive cross section in a well defined kinematic range, in the spirit of the measurements by the H1 collaboration [2].

The structure of this thesis is as follows. In chapter 2, an overview of diffractive scattering is presented, introducing the pomeron and reggeon in Regge theory and describing the phenomenological models used to correct the experimental data and compare with the HERA expectations. Chapter 3 contains a description of the Run II DØ detector, focusing on the detector components used in this analysis, and a description of the Tevatron accelerator. In chapter 4, the first measurement of the

efficiency of the Run II DØ Luminosity Monitor is presented. The work presented in this thesis forms the basis of the luminosity determination at DØ which is used in all cross section measurements in Run II. In section 5, the observation of candidate events for diffractive production of  $Z$  bosons in the muon channel and work towards measuring the cross section times branching ratio are described. The data are compared for the first time to a Monte Carlo simulation in which the HERA diffractive parton distributions are used as input.

## Chapter 2

# Diffractive Scattering and the Pomeron

The aim of this thesis is to search for diffractive  $Z$  boson production in  $p\bar{p}$  collisions using the DØ detector at the Tevatron. Diffraction does not have a clear experimental definition, but in  $p\bar{p}$  interactions the simplest definition is that one of the initial protons remains intact after the collision:  $p + \bar{p} \rightarrow p + X$  (or the charge conjugate).<sup>1</sup>

This chapter presents an overview of diffractive scattering. Section 2.1 introduces Regge theory, which predates quantum chromodynamics (QCD) and describes the behaviour of scattering amplitudes as the centre of mass energy tends to infinity. This discussion is relevant to the normalisation of cross section measurements at the Tevatron, through the behaviour of the total  $p\bar{p}$  cross section (Section 4), and it provides a theoretical framework in which to describe diffractive scattering. The

---

<sup>1</sup> Both initial beam particles are referred to as protons unless it is necessary to distinguish them.

pomeron and reggeon, quasi-particles that are exchanged in diffractive scattering, are introduced. Section 2.2 discusses the observation of diffractive interactions: the experimental signatures, and the kinematic region of low  $\xi$ , the fractional momentum loss of the proton, in which diffractive scattering dominates. The previous measurements of diffractive  $W$  and  $Z$  boson production are briefly discussed. Section 2.3 describes the simulation of diffractive  $Z$  boson production in  $p\bar{p}$  collisions using the event generator POMWIG, which uses the H1 diffractive parton distributions under the assumption of Regge factorisation; the breakdown of factorisation, or ‘gap survival probability’ is also discussed.

## 2.1 Regge Theory

In the mid-1950s, experimentalists knew of several strongly interacting particles. The first to be discovered were the proton, neutron, pion and antiproton. Many others followed, and the hadrons proliferated into an unwieldy and worryingly large group. Some hadrons were pronounced fundamental and others composite, somewhat arbitrarily [11], and little was known of the mechanism of the strong force. Scattering experiments of the time (such as  $\pi^\pm p$ ,  $pp$ ,  $p\bar{p}$ ) could measure the total cross sections and the final states. But a theory with predictive power was needed.

Tullio Eugenio Regge, born in 1931 in Turin, was to provide such a theory. Regge considered the initial and final states of a scattering process, applied some basic postulates, and proposed a general relationship for the behaviour of hadron-hadron ( $h$ - $h$ ) scattering cross sections as a function of centre of mass energy. Crucially, he did this without knowing the underlying interaction mechanism. This was

years before the advent of quark theory (1964), which first posited that nucleons were composites of three quarks, or QCD (1966), the quantum field theory that describes the strong force as an interaction mediated by gluons [12, 13]. A full derivation of Regge theory can be found in [14] but for this thesis a statement of the results will be sufficient.

### 2.1.1 Some concepts used in Regge theory

#### Interaction topologies

In a  $2 \rightarrow 2$  interaction  $a + b \rightarrow c + d$ , two of the Mandelstam kinematic variables are defined in terms of the particle four momenta as

$$s = (p_a + p_b)^2, \quad t = (p_a - p_c)^2 \quad (2.1)$$

where  $\sqrt{s}$  is the centre of mass energy and  $t$  is the square of the four momentum transfer between  $a$  and  $c$  (the third kinematic variable,  $u = (p_a - p_d)^2$ , is not independent). This gives rise to an important distinction between interaction topologies. In the  $s$ -channel, particles  $a$  and  $b$  annihilate and produce a real particle (or ‘resonance’) which subsequently decays. The term resonance is used because the scattering amplitude for the process rises sharply when  $\sqrt{s} \approx m$ , just as for resonant frequencies. The  $t$ -channel involves the exchange of a virtual particle between  $a$  and  $b$ , and kinematically the square of the four momentum transfer is negative.

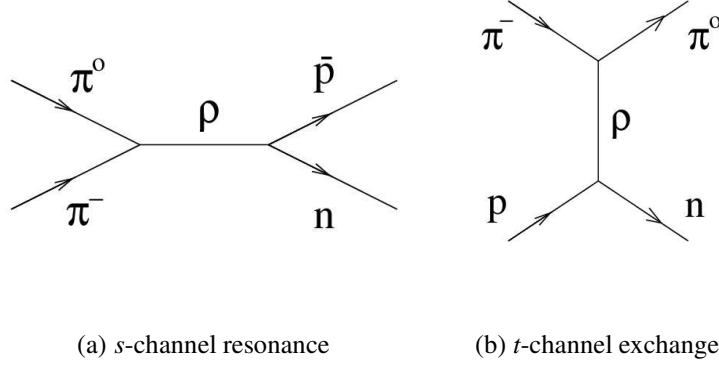


Figure 2.1: Crossing symmetry between (a)  $s$ -channel and (b) crossed  $t$ -channel processes

### Crossing symmetry

Fig. 2.1 has examples of  $s$ - and  $t$ -channel interactions, the amplitudes for which are related through *crossing symmetry*. Crossing symmetry states that the scattering amplitudes for the  $s$ -channel process  $a + b \rightarrow c + d$  and the  $t$ -channel in the ‘crossed’ process  $a + \bar{c} \rightarrow \bar{b} + d$ , with  $s$  and  $t$  interchanged [15], are equal. The allowed resonances have the same quantum numbers as the allowed virtual exchanges. In other words, crossing symmetry states that the amplitudes  $\mathcal{A}(s, t)$  are equal for the  $s$ -channel and crossed  $t$ -channel processes even though they are quite different physical processes.

### Optical theorem

The optical theorem is a relationship between the total cross section  $\sigma_{tot}$  and the imaginary part of the forward scattering amplitude  $\mathcal{A}(s, 0)$ :

$$\sigma_{tot} \approx \frac{\Im m \mathcal{A}(s, 0)}{s}, \quad (2.2)$$

where the amplitude is *forward* because the momentum transfer  $t$  is zero. Momentum transfer is related to the centre of mass frame scattering angle  $\theta$  by

$$\cos \theta = 1 + \frac{2t}{s} ,$$

so  $t = 0$  corresponds to zero scattering angle.

### 2.1.2 Scattering amplitude

The central aim of Regge theory is to describe the behaviour of scattering amplitudes in the ‘Regge limit’,  $s \rightarrow \infty$  with  $s/t$  fixed. The amplitude for  $t$ -channel exchange is written as a sum of partial wave amplitudes that correspond to all the possible exchanges with different angular momenta. In the case of  $\pi^- p \rightarrow \pi^0 n$  scattering these include the exchange of the light mesons with the appropriate quantum numbers  $\rho$ ,  $\omega$ ,  $f_2$ ,  $a_2$  and so on. The  $s$ -channel amplitude for the related crossed process, in this case  $\pi^- \pi^0 \rightarrow \bar{p} n$  scattering, is then obtained through crossing symmetry by interchanging  $t$  and  $s$ .

Regge generalised the amplitude with the concept of *complex* orbital angular momentum [16, 17]. Particles can have only integer  $l$ , but in the complex  $l$ -plane the scattering amplitude may have poles (singularities at which the amplitude tends to infinity) that have central significance in this theory. They are called *Regge poles*,  $\alpha_n(t)$ . In the Regge limit, only the right-most pole in the complex  $l$ -plane – the one with the largest real part – contributes to the amplitude. So the main result of Regge theory is a rather simple statement about the way a scattering amplitude depends on  $s$ :

$$\mathcal{A}(s, t) \sim s^{\alpha(t)} \quad s \gg |t| \quad (2.3)$$

It should be noted that Eq. 2.3 applies to *all* scattering processes, because it does not claim to know anything about the underlying mechanism.

### 2.1.3 Regge trajectories

At Berkeley in the early 1960s, Geoffrey Chew claimed that all hadrons should be treated equally instead of being divided – as in the field theory approach – into groups of elementary and composite particles [18].<sup>2</sup> With this in mind, he and his postdoctoral student Steven Frautschi felt that Regge theory was the most promising approach to the strong interaction, and they proceeded to test and extend the theory with scattering data. The Chew-Frautschi plot [11, 19] in Fig. 2.2 shows the total angular momentum,  $J$ , versus the mass squared,  $M^2$ , for particular sets of hadrons: in this case, the meson resonances in  $\pi^-\pi^0 \rightarrow \bar{p}n$  scattering.

It was a remarkable result, because the data lie on a straight line. So for hadrons with the same quantum numbers,  $J$  is proportional to  $M^2$ . The linear function is called a *Regge trajectory*; in this particular case it is the  $\rho$ -trajectory, denoted  $\alpha_R(t)$  here. From the data the parameters of the  $\rho$ -trajectory  $\alpha_R(t) = \alpha_R(0) + \alpha'_R t$  are

$$\alpha_R(0) = 0.55$$

$$\alpha'_R = 0.86 \text{ GeV}^{-2}$$

where  $\alpha_R(0)$  is the intercept on the  $J$  axis,  $\alpha'_R$  is the gradient, and the particles are at  $\alpha(M^2) = J$ .

The true power of the Regge approach comes when the  $s$ -channel amplitude for  $\pi^-\pi^0 \rightarrow \bar{p}n$  scattering in Fig. 2.1 is related via crossing symmetry to the  $t$ -channel

---

<sup>2</sup> “My standpoint here... is that every nuclear particle should receive equal treatment under the law.”



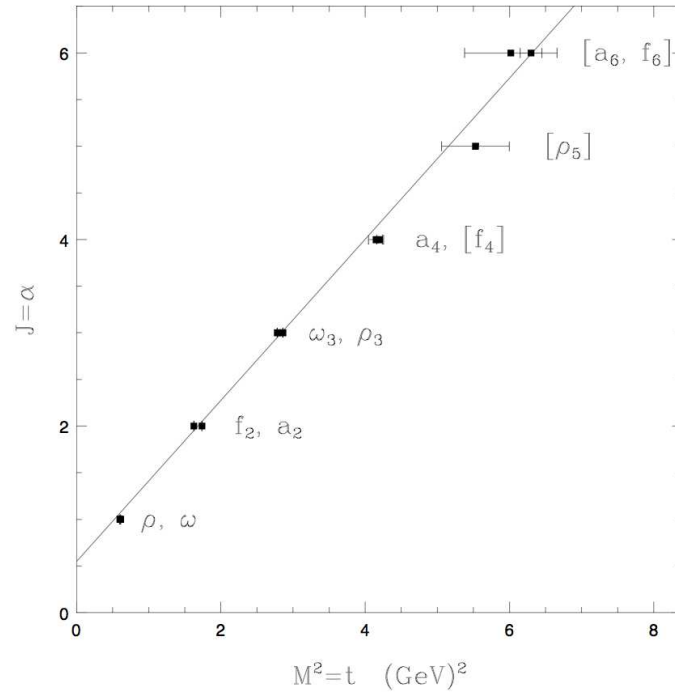


Figure 2.2: Chew-Frautschi plot of resonances in  $\pi^- \pi^0 \rightarrow \bar{p} n$  scattering [14]

process for  $\pi^- p \rightarrow \pi^0 n$  scattering. As stated before, their amplitudes are equal when  $s$  and  $t$  are interchanged. But because the energy dependence of the amplitude is driven by the Regge trajectory (Eq. 2.3), the two processes are also connected in the Chew-Frautschi plane. The  $s$ -channel  $\pi^- \pi^0$  data lie in the  $t > 0$  region in Fig. 2.3. Crossing symmetry predicts that the  $t$ -channel  $\pi^- p$  data lie in the  $t < 0$  region along the extrapolated Regge trajectory. This is due to a property of the amplitude called analyticity, whereby it can be continued across the  $t = 0$  boundary. The prediction is verified with the data in Fig. 2.4 [14].

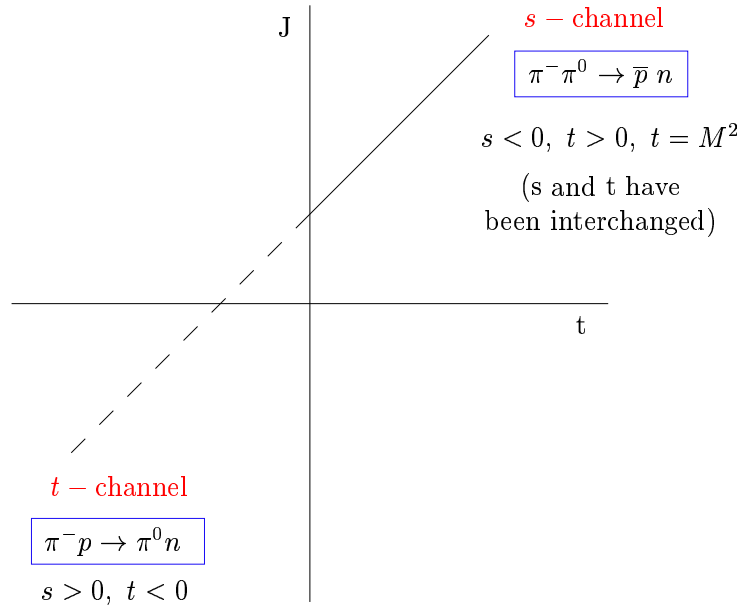


Figure 2.3: Relationship between  $s$  and  $t$  channel processes in the  $J - t$  plane

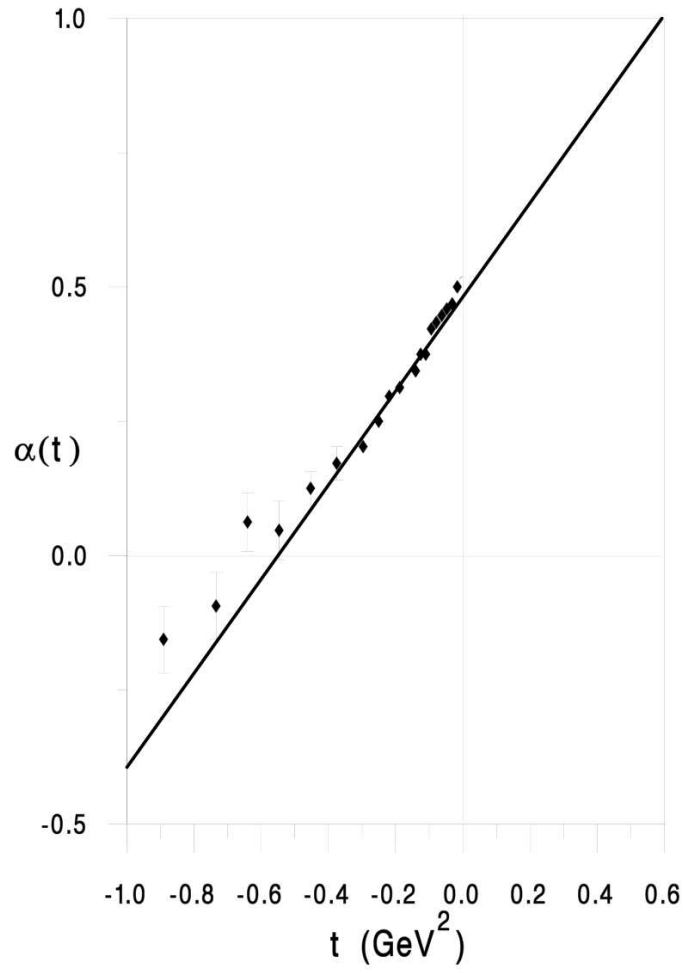


Figure 2.4: Chew-Frautschi plot of  $\pi^- p \rightarrow \pi^0 n$  scattering [14]

### 2.1.4 Total scattering cross section

The final piece in the theory is the total cross section. Substituting Eq. 2.3 at  $t = 0$  into Eq. 2.2, the total cross section behaves as

$$\sigma_{tot} \sim s^{\alpha(0)-1} \quad (2.4)$$

where  $\alpha(0)$  is the intercept of the Regge trajectory that mediates the interaction. This is less than unity for the  $\rho$ -trajectory so the total cross section decreases with increasing  $s$  for this type of exchange. In fact, it had already been noted by Pomeranchuk and Okun in 1956 that the total cross section for  $h$ - $h$  scattering would decrease as  $s$  increases when charge is exchanged [20].

This picture of a decreasing total cross section with centre of mass energy in reggeon exchange is successful, but as the data show for  $pp$  and  $p\bar{p}$  scattering in Fig. 2.5 the total cross section starts increasing from around 20-30 GeV. This behaviour had also been predicted by Pomeranchuk, at a time when the highest experimental energy was about 1 GeV [21].

### 2.1.5 The pomeron

Pomeranchuk realised in 1958 that the cross sections of a particle and antiparticle on a given target are equal to each other at asymptotically high energy [22]. This is known as the Pomeranchuk Theorem and it was the only theoretical result, derived from first principles, in the field of strong interactions at the time [23]. For these cross sections to be the same the exchanged objects must couple equally with particles and antiparticles. Therefore they must have the quantum numbers of the vacuum: no charge, no colour, and zero spin, isospin and baryon number. Clearly

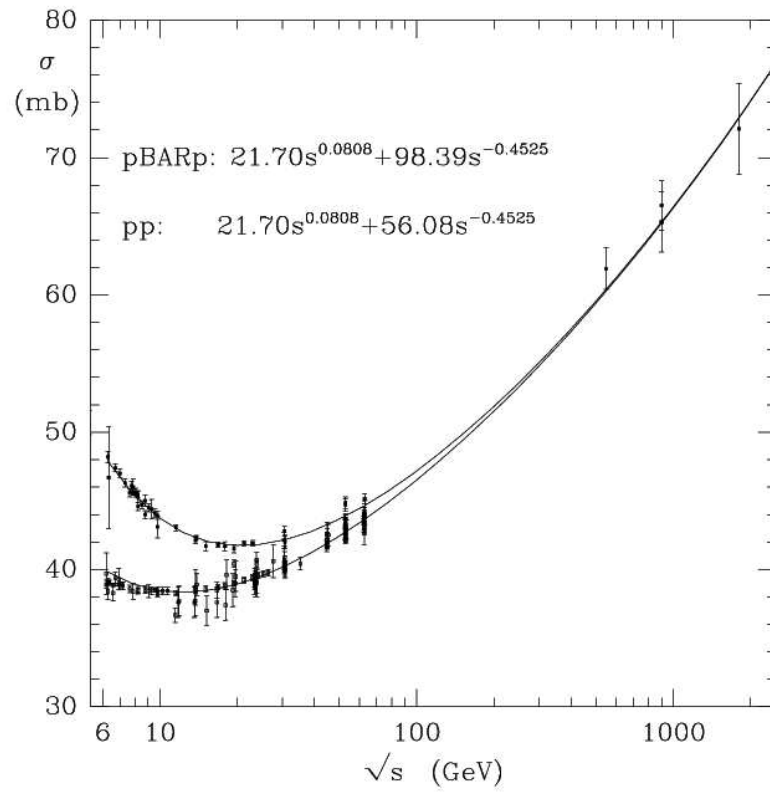


Figure 2.5: Total cross section for  $p\bar{p}$  (upper curve) and  $pp$  scattering as a function of centre of mass energy [24]

these particles must lie on a different kind of Regge trajectory, one that has an intercept greater than unity so that the cross section will rise. The trajectory and its corresponding quasi-particle were given the name *pomeron* after Pomeranchuk.

Fig. 2.5 shows a fit to the  $pp$  and  $p\bar{p}$  data by Donnachie and Landshoff [24] using

$$\sigma_{pp(p\bar{p})} = A s^{\alpha_P(0)-1} + B_{pp(p\bar{p})} s^{\alpha_R(0)-1} \quad (2.5)$$

where A is the coefficient for pomeron exchange, which is the same in both scattering processes, and B is the contribution from reggeon exchange. At low energies reggeon exchange dominates and  $\sigma_{tot}$  decreases; at high energies pomeron exchange drives the cross section upwards. The fit yields

$$\alpha_P(0) = 1.08$$

and the coefficients shown in the figure. The gradient of the trajectory is determined [14] from the differential cross section  $d\sigma/dt$  to be

$$\alpha'_P = 0.25 \text{ GeV}^{-2} .$$

Regge intercepts are universal: all kinds of scattering that are mediated by the same trajectory have the same power law in  $\sigma_{tot}$ .

The pomeron trajectory is more complicated than that of the reggeon. With an intercept of 1.08, the cross section would continue to rise and eventually violate unitarity at very high centre of mass energy. The rise of the total hadronic cross sections must be tamed with increasing  $s$  by multiple pomeron exchanges: when two, three or more pomerons are exchanged in the same interaction they contribute to the cross section with alternating signs and increasing magnitude as  $s \rightarrow \infty$ . For this reason  $\alpha_P(0)$  is really an *effective* intercept, and it changes slowly with

*s*. At currently accessible centre of mass energies it is more or less constant; multiple pomeron exchanges are only about 10% of the total cross section at  $\sqrt{s} = 1.8$  TeV [25].

Furthermore, there appear to be two trajectories for the pomeron. The *soft pomeron* described above has the intercept  $\alpha_P(0) = 1.08$ . In 1997, experiments at HERA [26] probed the proton with a virtual photon (emitted from an electron) and found that the pomeron intercept appears to increase with the virtuality of the photon and the energy dependence of the total cross section steepens accordingly. The next year, Sandy Donnachie from Manchester and Peter Landshoff from Cambridge proposed [27] that this behaviour could be described if there is an additional *hard pomeron* with  $\alpha_P(0) \sim 1.4$ .

The physical particles on the soft and hard pomeron trajectories have not been identified; they may be composites of two or more gluons ('glueballs') [28]. The lowest object on the soft trajectory would be  $J = 2$  with a mass of about 2 GeV, and there has been a glueball candidate for this state [29].<sup>3</sup> Another glueball candidate with slightly higher mass [30] may lie on the hard pomeron trajectory [27].

## 2.2 Diffractive Scattering

Pomeron and reggeon exchanges are colourless, so the hadrons from which they are emitted may stay intact. A diffractive  $p\bar{p}$  interaction is often defined experimentally as one in which a proton emerges intact from the collision, and this type of event can be observed using detectors located along the trajectory of the

---

<sup>3</sup> As is the convention, natural units are used throughout:  $c = \hbar = 1$ , so that mass, momentum and energy are expressed in eV ( $1\text{eV} = 1.602 \times 10^{-19} J$ )

scattered proton. A system of spectrometers, in which the proton momentum is measured in the accelerator magnetic field, has been built for this purpose at DØ (Section 3.2.6) but this is undergoing commissioning at the time of this analysis.

### 2.2.1 Rapidity gaps

Diffraction interactions often have another experimental signature, which is a rapidity gap: a large region with no particles close to the outgoing intact proton. This can be understood as a lack of colour connections in the region between the outgoing proton and the dissociative system. In addition, a rapidity gap is kinematically required in a system of particles with low invariant mass with respect to the centre of mass energy of the collision, and diffractive interactions can be defined theoretically in this way ( $s \gg M_X^2$ , the Regge limit). In non-diffractive interactions, the distribution of final state particles is approximately uniform in rapidity, and gaps are exponentially suppressed: the probability of a rapidity gap of size  $\Delta y$  is proportional to  $e^{-a\Delta y}$  for some constant  $a$  [31].

The rapidity  $y$  of a particle can be defined in terms of its energy  $E$  and longitudinal momentum  $p_L$ ,

$$y = \frac{1}{2} \ln \frac{(E + p_L)}{(E - p_L)},$$

and if the coordinates of the system are defined with the  $z$ -axis along the collision axis, then  $p_L = p_z$  where  $p_z$  is the  $z$  component of the momentum. It is also convenient to define the transverse energy,  $E_T = E \sin \theta$ , where  $\theta$  is the polar angle with respect to the  $z$ -axis. Pseudorapidity  $\eta$  is defined in terms of the polar angle,

$$\eta = -\ln(\tan(\frac{\theta}{2})),$$



and it is often used as a coordinate in detectors. In the limit  $m/E \rightarrow 0$ , rapidity and pseudorapidity are equal. Regions of high pseudorapidity, close to the outgoing beam particles, are referred to as forward; the region  $|\eta| \sim 0$  is referred to as central.

### 2.2.2 Previous analyses of diffractive W/Z boson production

Previous observations of diffractively produced  $W$  and  $Z$  bosons, using data from Run I at the Tevatron, have relied on the presence of a rapidity gap in the event. The CDF collaboration published results for diffractive  $W$  boson production in the electron decay channel [32], presenting the ratio ( $R_W$ ) of  $W$  boson events with a rapidity gap to those without:

$$R_W = (1.15 \pm 0.55)\% .$$

The DØ collaboration observed diffractive  $W$  boson production in the electron decay channel and a sample of 8 diffractive  $Z \rightarrow e^+e^-$  candidate events [10]. They quoted their results in terms of the ‘gap fractions’  $F_W$  ( $F_Z$ ) of  $W$  ( $Z$ ) boson events with a rapidity gap:

$$F_W = (0.89^{+0.19}_{-0.17})\%$$

$$F_Z = (1.44^{+0.61}_{-0.52})\% .$$

The results from CDF and DØ cannot be compared with each other because CDF applied a correction for diffractive events that do not have a rapidity gap whereas DØ published the uncorrected result.

### 2.2.3 Fractional momentum loss of the proton

The fractional longitudinal momentum loss of the intact proton,  $\xi$ , may be defined as

$$\xi = 1 - p_f/p_i ,$$

where  $p_i$  and  $p_f$  are the initial and final longitudinal momenta of the outgoing proton. The momentum loss  $\xi$  can be measured experimentally as  $\xi \sim M_X^2/s$  so a predominantly diffractive sample, which has a low mass final state, can be defined experimentally by requiring events to have low  $\xi$ . The region  $\xi \lesssim 0.01$  is dominated by pomeron exchange, and larger momentum loss corresponds to larger contributions from reggeon exchange. The rapidity gap size  $\Delta y$  increases as  $\Delta y \sim \ln(1/\xi)$ , so low  $\xi$  (pomeron) interactions are characterised by large rapidity gaps. Reggeon interactions tend to have smaller rapidity gaps, because they occur at higher  $\xi$ .

The fractional momentum loss can be reconstructed using

$$\xi \approx \frac{1}{\sqrt{s}} \sum_i E_T^i e^{\eta^i} \quad (2.6)$$

where the sum is over particles in the final state, and  $E_T^i$  and  $\eta^i$  are the transverse energy and pseudorapidity of the  $i$ th particle. This approximation assumes that the energy of the incoming proton is large [31]. The dominant contributions to the ‘ $\xi$  sum’ are from particles close to the scattered proton, which have large pseudorapidities, and particles with large  $E_T$ . The contribution from particles in the opposite direction to the intact proton is small, so a lack of detector coverage in this region does not have a large effect on the measurement.

In this thesis, the first steps towards measuring the diffractive  $(Z/\gamma)^*$  boson production cross section (multiplied by the branching ratio for the muon decay chan-

nel) are presented. The cross section is defined kinematically by  $\xi$ , where the lowest accessible  $\xi$  value in this analysis is  $\xi \sim M_Z^2/s$ , and the upper limit is chosen such that there is a sufficiently large forward rapidity gap for observation (Section 5.4.1).

## 2.3 Simulation of diffractive Z boson production

The Monte Carlo event generator POMWIG [33] is the only Monte Carlo generator currently available that can simulate diffractive Z boson production at the Tevatron. As mentioned in Section 1, it is possible to define diffractive parton distribution functions (pdfs) in diffractive deep inelastic electron-proton scattering. These are proton pdfs with the additional constraint that the proton remains intact [3]. The H1 Collaboration at HERA [4] measured the diffractive deep inelastic scattering cross section, and parameterised the data using a Regge factorisation ansatz (sometimes referred to as the Ingelman-Schlein model [34]). In Regge factorisation, the interaction is separated into two parts: the emission of a pomeron or reggeon from the proton, and the interaction of the pomeron or reggeon with the other beam proton. A diagram for this in  $pp$  collisions is shown in Fig. 2.6. At the upper vertex, a pomeron is emitted with squared momentum transfer  $t$ , and a fraction  $\xi$  (referred to as  $x_{IP}$  at HERA) of the proton momentum. The ‘probability’ for this to occur can be described in terms of a ‘pomeron flux factor’  $F(x_{IP}, t)$ .<sup>4</sup> The pomeron takes part in a hard scale (high  $p_T$ ) interaction with the other proton, in which the pomeron structure function  $F_2^{IP}(\beta, Q^2)$  describes the probability of a

---

<sup>4</sup> The pomeron flux factor is not absolutely normalised, and so can be greater than unity. The term probability is therefore used loosely.

parton in the pomeron with a fraction of the pomeron momentum,  $\beta$ , being struck by a parton in the proton with virtuality  $Q^2$ .

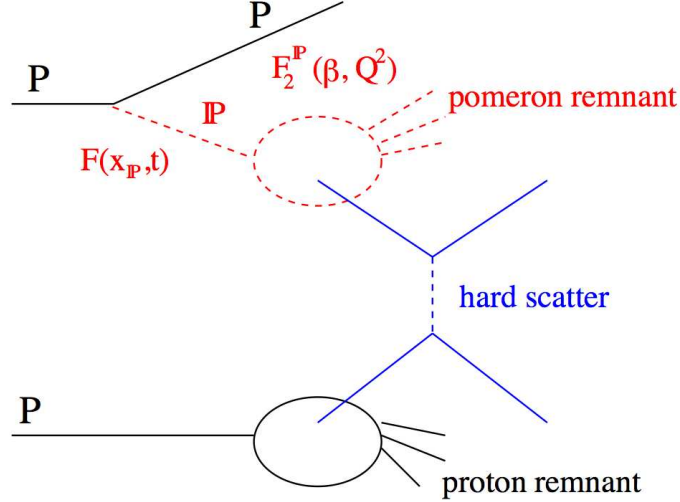


Figure 2.6: POMWIG uses the factorisation model of single diffraction [33]

The pomeron and reggeon flux terms are parameterised as

$$f_{IP}(\xi) = N \int_{t_{\min}}^{t_{\max}} \frac{e^{\beta_{IP}(t)}}{\xi^{2\alpha_{IP}(t)-1}} dt \quad (2.7)$$

$$f_{IR}(\xi) = C_{IR} \int_{t_{\min}}^{t_{\max}} \frac{e^{\beta_{IR}(t)}}{\xi^{2\alpha_{IR}(t)-1}} dt \quad (2.8)$$

where  $\alpha_{IP}(t) = \alpha_{IP}(0) + \alpha'_{IP}t$  and  $\alpha_{IR}(t) = \alpha_{IR}(0) + \alpha'_{IR}t$ . The diffractive cross section is then expressed as the sum of the pomeron and reggeon flux terms and the structure functions of the pomeron and reggeon. The normalisation of the pomeron flux,  $N$ , is set such that the generated deep inelastic scattering cross section matches the H1 measurement at  $\xi = 0.003$ . The reggeon normalisation term,  $C_{IR} = 48$ , was fitted to data by the H1 Collaboration [4]. It should be noted that H1 had little data in the higher  $\xi$  range ( $\xi \gtrsim 0.01$ ) which is probed in diffractive Z boson production at the Tevatron [33]. The normalisation of the reggeon flux

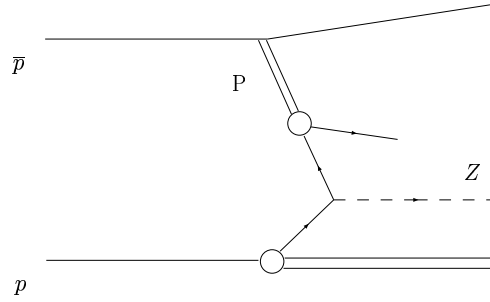
Quantity	Value
$\alpha_{IP}$	1.20
$\alpha_{IR}$	0.57
$\alpha'_{IP}$	0.26
$\alpha'_{IR}$	0.90
$B_{IP}$	4.6
$B_{IR}$	2.0
$C_{IR}$	48

Table 2.1: The default parameters in POMWIG

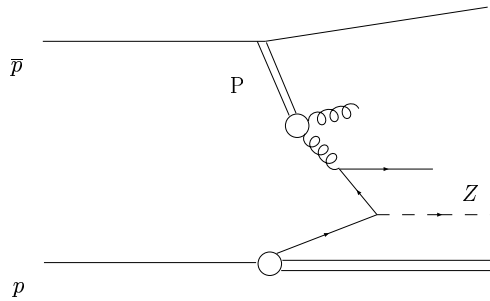
is therefore one of the largest uncertainties in the predictions of POMWIG in the Tevatron kinematic range. The pomeron structure function was fitted to data, and a pion structure function was used for the reggeon [35]. Throughout this analysis, the POMWIG default parameters (Table 2.3) are used. H1 produced three separate pomeron structure function fits: the default fit, known as ‘fit 2’, is used in the analysis; ‘fit 3’, which has a larger gluon content at high  $\beta$ , is used to cross-check the systematic uncertainties (Sections 5.6.3 and 5.6.4).

Diffraction  $W$  and  $Z$  boson production can be, with large statistics, a sensitive probe of the structure of the pomeron (and reggeon in the higher  $\xi$  region). At leading order (LO), diffractive  $W$  and  $Z$  bosons are produced from a quark in the pomeron or reggeon. At next to leading order (NLO), a gluon from the pomeron or reggeon splits into a  $q\bar{q}$  pair before the interaction (Fig. 2.7).

There has been only one prediction of the cross section for diffractively produced  $Z$  bosons, by Bruni and Ingelman in 1993 [36]. In the kinematic range



(a) LO:  $q\bar{q} \rightarrow Z$



(b) NLO:  $q g \rightarrow q + Z$

Figure 2.7: Leading order and next-to-leading order diagrams for diffractive Z boson production

$\sqrt{s} = 1.8 \text{ TeV}$ ,  $\xi < 0.1$  and  $|t| < 1 \text{ GeV}^2$ , and with the requirement that the two muons have  $|\eta| < 3$  and  $p_T > 20 \text{ GeV}$ , they predict that the cross section times branching ratio for diffractive  $Z \rightarrow \mu^+\mu^-$  production is 28 pb for a quark-dominated pomeron, 1 pb for a pomeron made of hard gluons, and 0.4 pb for a pomeron made of soft gluons. The corresponding diffractive fractions are 13%, 0.5% and 0.2% of their total  $Z \rightarrow \mu^+\mu^-$  cross section. These predictions did not include an estimate of gap survival probability, however. This is discussed in the following section.

### 2.3.1 Rapidity gap survival

The Collins factorisation theorem [3] which allows diffractive pdfs to be defined does not apply in hadron-hadron collisions. The reason for this ‘factorisation breakdown’ is generally accepted to be due to collisions between spectator partons in the colliding protons, causing the outgoing proton to dissociate and therefore destroying the proton and the rapidity gap [37, 38, 39]; it is given the name ‘gap survival probability.’ This would seem to imply that POMWIG cannot be used at the Tevatron. In diffractive dijet production at the Tevatron, for example, POMWIG has been shown to overestimate the magnitude of the cross section by a factor of approximately 10 [40, 41]. However, the kinematic distributions of quantities such as the rapidities and  $E_T$  of the jets are correctly predicted by POMWIG, albeit within large uncertainties. This suggests that gap survival can be accounted for by an overall multiplicative factor: in the case of diffractive dijet production, the gap survival probability is  $s \sim 0.1$ . It is one of the aims of this thesis to assess the extent to which gap survival probability is process-specific; it is the first comparison of diffractively produced electroweak boson data with a

Monte Carlo simulation that uses the H1 diffractive parton distributions.



## Chapter 3

# The DØExperiment at the Tevatron

### 3.1 The Tevatron Accelerator

The Tevatron, 40 miles west of Chicago, is a synchrotron accelerator that collides protons with antiprotons. At  $\sqrt{s} = 1.96$  TeV, it has the highest centre of mass energy of any accelerator currently operating in the world, and it generates collisions at an average rate of 1.7 million times per second. The Tevatron accelerator components are housed in a tunnel with a circumference of about 6 km underneath the restored prairie lands at the Fermi National Accelerator Laboratory (Fermilab) in Batavia, Illinois. The Fermilab chain of accelerators is shown in Figure 3.1.

At the beginning of the Tevatron chain is a bottle of hydrogen gas, about the size of a fire extinguisher, inside the Cockcroft-Walton accelerator. The Cockcroft-Walton turns hydrogen molecules into  $H^+$  ions and accelerates them through a series of potential differences to an energy of 750 keV. After this is the Linac, a long line of radio frequency (RF) cavities: these are tubes separated by gaps,

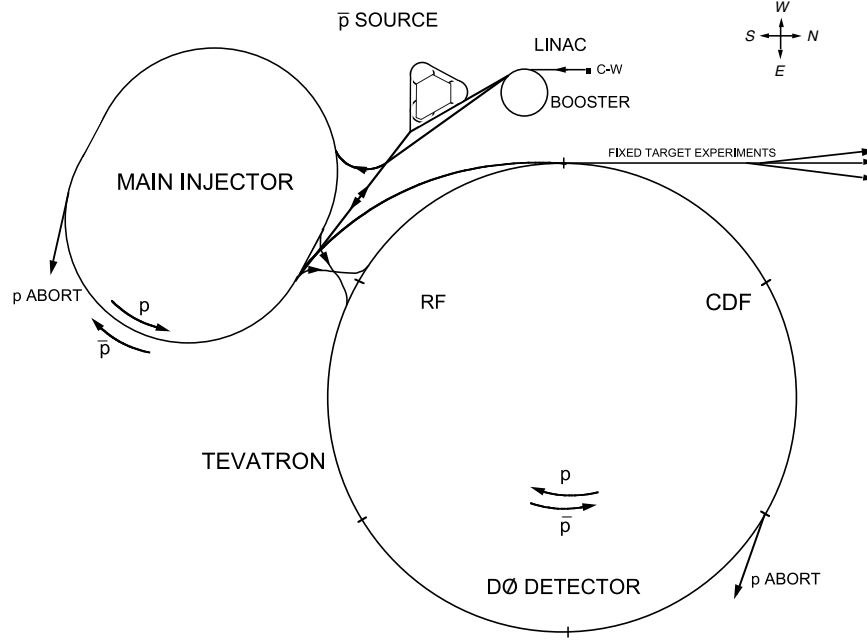


Figure 3.1: The Fermilab accelerator complex

with an alternating electric field at low frequency. The field is aligned to give a positive gradient in the gaps, accelerating the particles and forcing them into discrete groups called bunches [42]. The bunched ions are accelerated by the Linac to 400 MeV, stripped of their electrons, and injected into the Booster, which is a small synchrotron accelerator that accelerates the protons to 9 GeV.

The proton bunches enter the Main Injector, a larger synchrotron with two modes: in the first, protons are accelerated to 120 GeV and sent to the  $\bar{p}$  source; in the second, they are accelerated to 150 GeV and injected into the Tevatron ring or fixed target experiments. Antiprotons are created by firing protons into a nickel target, using tens of thousands of protons to produce each one. The antiprotons are accumulated and stored at 9 GeV until they are needed for a period of collisions, known as a *store*, for which they are sent to the Main Injector for acceleration to

150 GeV and injection into the Tevatron ring [43]. Inside the Tevatron a set of RF cavities accelerates the  $p$  and  $\bar{p}$  beams to 980 GeV by boosting the particles when they pass; the field frequency is matched to the increasing rotational frequency of the beam.

The Tevatron magnets are superconducting. Dipole magnets deflect the beam into a circular path by exerting a horizontal Lorentz force  $\underline{F} = q \underline{v} \times \underline{B}$ , where  $q$  is the charge and  $\underline{v} \times \underline{B}$  is the vector cross product between the velocity and magnetic field. The magnetic field is increased to match the increasing particle energy. Quadrupole magnets focus the beam by deflecting stray particles back into the correct path. There are also sextupole magnets for higher order corrections.

Each beam has 36 bunches distributed in three groups of 12 called superbunches. The relative position of the bunches is marked by time periods of 132 ns called ticks, of which there are 159 in the ring. Within a superbunch, the bunch spacing is three ticks (396 ns, which corresponds to about 120 m). The beam structure is illustrated in Figure 3.2.

The  $p$  and  $\bar{p}$  beams are kept apart in a helical orbit everywhere except the two interaction regions. These are named by their locations on the ring: DØ, where there is a detector of the same name and BØ, where there is the Collider Detector at Fermilab (CDF). This analysis uses data taken by the DØ detector during Run II. The official start of Run II was March 2001. For Run II the Tevatron has a higher centre of mass energy ( $\sqrt{s}$  has increased from 1.8 to 1.96 TeV), increased luminosity, and decreased bunch crossing spacing (from 3.5  $\mu$ s to 396 ns), and many parts of the DØ and CDF detectors have been replaced.

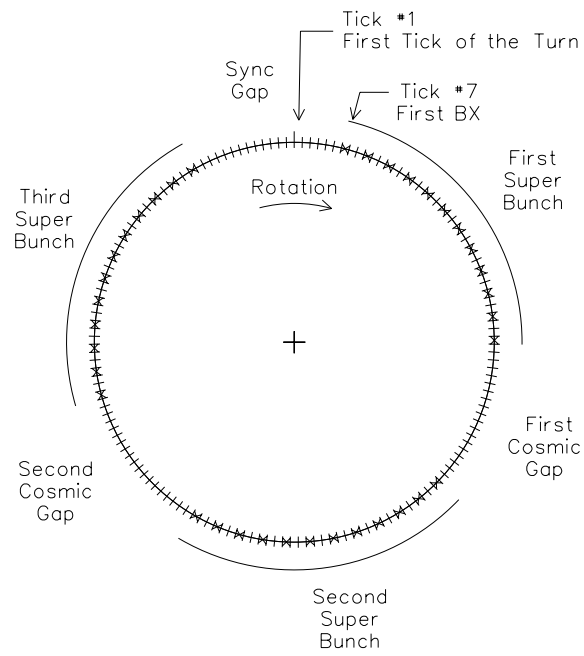


Figure 3.2: The Tevatron beam structure, showing the three superbunches each with 12 bunches

## 3.2 The DØ Detector

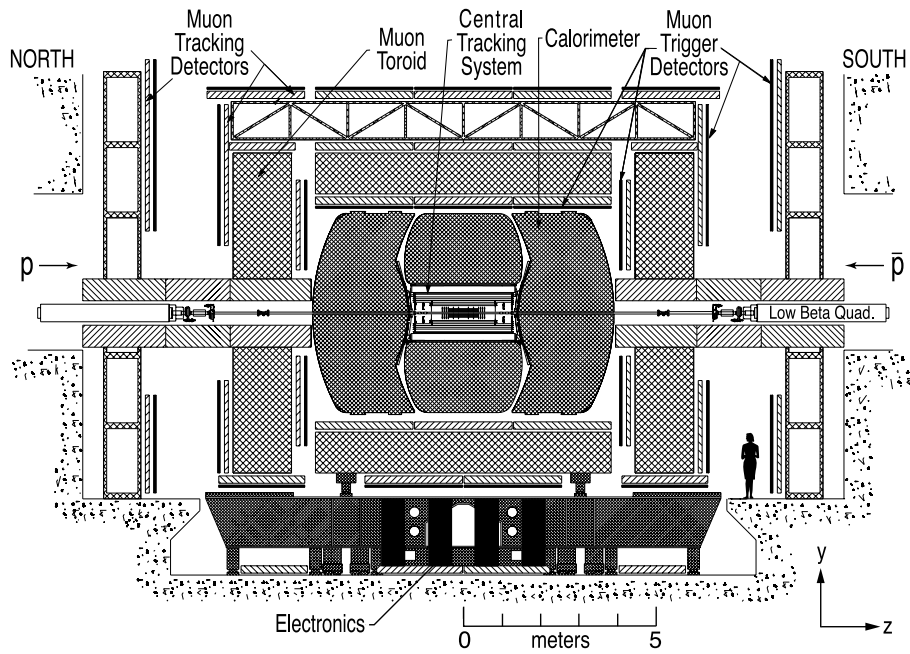


Figure 3.3: Diagram of the DØ detector

The DØ detector is nearly four storeys high and surrounds a 20 m section of the beam on the east side of the Tevatron ring (Fig. 3.3). There are several concentric layers, including a tracking system, with two detectors and a solenoid magnet; a calorimeter; and a muon detector system with a toroid magnet. There is a forward proton detector to detect outgoing intact beam particles located at a distance of several metres along the beam line in either direction.

DØ uses a right-handed coordinate system in which the  $z$ -axis points along the proton beam direction, toward the south end of the detector. North and south are used to denote the outgoing  $\bar{p}$  and  $p$  directions respectively. The  $x$ -axis is in the horizontal plane, pointing out of the Tevatron ring (east) and the  $y$ -axis points upwards. The azimuthal angle  $\phi$  ranges from  $0 - 2\pi$ . The detector coordinate

system is centred on  $(x, y, z) = (0, 0, 0)$ , and the ‘physics’ coordinate system is centred on the interaction vertex.

The detector subsystems are described in the following sections. More details on all aspects of the DØ detector can be found in [44].

### 3.2.1 Tracking system

The central tracker is the first system encountered by particles that emerge from the beryllium beam pipe, measuring the trajectories of charged particles in a magnetic field. There is an inner detector, the silicon microstrip tracker (SMT), an outer detector, the central fiber tracker (CFT) and a superconducting solenoid magnet which encloses them (Fig. 3.4).

The SMT is a high resolution detector surrounding the interaction region. It is constructed in two parts: barrels, which are cylinders around the beam pipe, and discs, which are transverse to the beam (Fig. 3.5). The six barrels are arranged longitudinally along the interaction region. Each has four concentric detector layers, of which some are single-sided and some double-sided. There are 12 small discs with double-sided detector wedges called F-disks in the central region and four large discs with back-to-back single-sided wedges, H-disks, in the forward region. The outer radius of the barrel sections and F-disks is about 10 cm, and for H-disks it is 26 cm. The pseudorapidity coverage is  $|\eta| \lesssim 2.5$ .

Each detector layer is a thin wafer of silicon with parallel strips across its surface. Single sided layers have only an  $n$ -side, a surface with a positive voltage bias and  $n$ -type doping to increase the number of mobile electrons. Double sided layers also have a  $p$ -side, which are doped to increase the number of positive electron

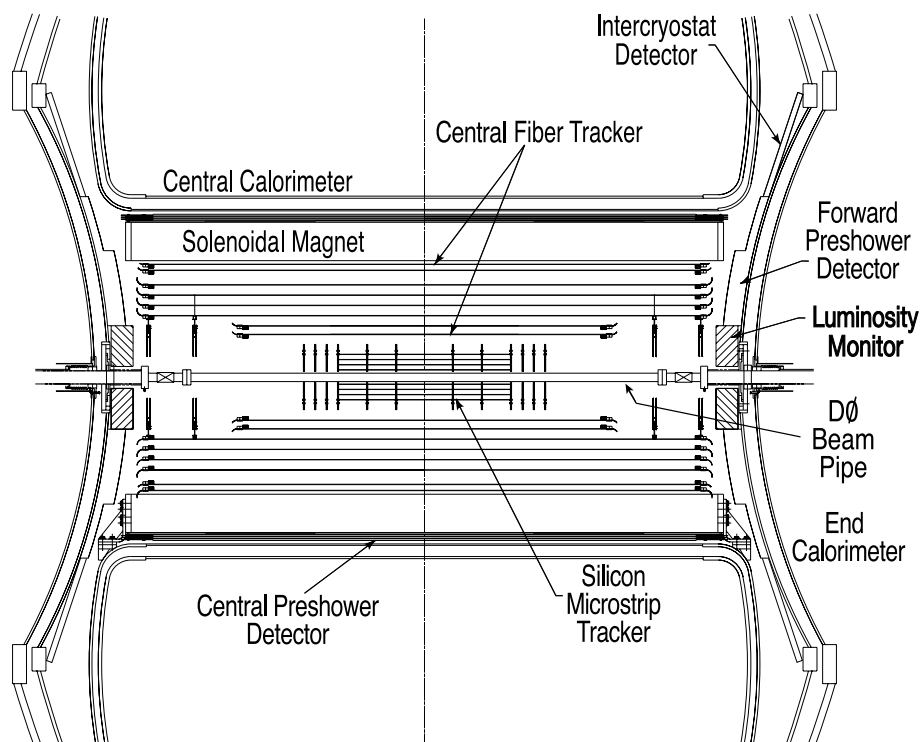


Figure 3.4: The central tracking system, consisting of the silicon microstrip tracker, central fiber tracker and solenoid magnet. Other detectors are also shown.

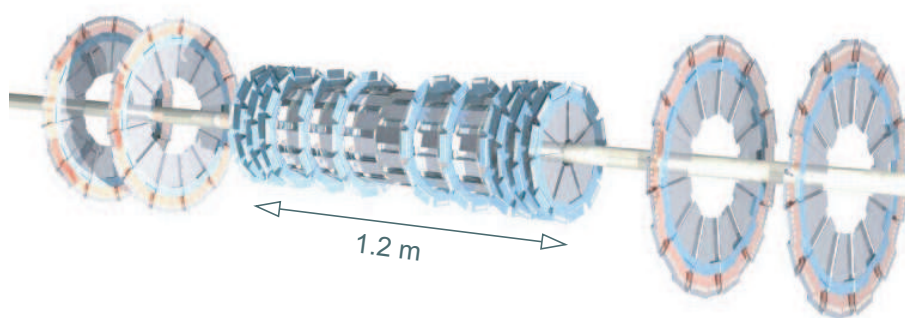


Figure 3.5: The silicon microstrip tracker

holes and have a negative voltage applied. When a charged particle passes through the silicon it creates electron-hole pairs: the electrons collect on the  $n$ -side and the holes on the  $p$ -side. The charge is sampled by ‘SVXIIe’ chips mounted directly on the detector. The SMT is cooled to less than about 5°C to reduce radiation damage.

The CFT spans the region 20 – 50 cm from the beam pipe and  $|\eta| \lesssim 1.7$ . It has scintillating fibres arranged in *doublet layers*: two layers of fibres, where one is offset from the other so as to leave no gaps. There are eight concentric cylinders in the CFT, each of which has an axial doublet layer and a stereo doublet layer at either +3° or -3°. The scintillating fibres are made of polystyrene and double clad in acrylic and fluoro-acrylic, with mirrored coating at one end. The cladding materials have lower refractive indices than the polystyrene. Excited atoms in the fibres emit yellow-green light, which is trapped and reflected to the read out ends and taken by clear waveguides to the visible light photon counters (VLPCs). These are avalanche photodiodes that convert the photons into a charge signal, which is read out with SVXIIe chips.

The superconducting solenoid is nearly three metres long, with an inner diameter of about a metre. The field is about 2T, axial and uniform over most of the tracking volume.

The detector signals (hits) in the tracking system are used to reconstruct the paths of charged particles, for calculation of particle momenta, particle identification and reconstruction of the position of the interaction vertex or vertices. The tracking system can measure the  $z$  position of the primary vertex with a resolution of about 35 $\mu$ m. The momentum of a particle with charge  $e$  in a magnetic field  $B$  is determined from the radius of curvature of its trajectory  $R$  by equating the Lorentz



force and the centripetal force  $mv^2/R$ . This yields the relationship  $p = eBR$ . High momentum charged particles have almost straight tracks, so it is more difficult to determine  $R$  and the momentum uncertainty is greater.

### 3.2.2 Preshower detectors

The central and forward preshower detectors measure the energy and position of particles before they enter the calorimeter, improving the energy resolution and detecting low  $p_T$  electromagnetic showers. The central preshower is mounted on the outside of the solenoid ( $|\eta| < 1.3$ ), and the forward preshower on the calorimeter end caps ( $1.5 < |\eta| < 2.5$ ), as shown in Fig. 3.4. They are made of scintillating strips read out by VLPCs. The preshower detectors are not used in this analysis.

### 3.2.3 Calorimeter

The DØ calorimeter system measures particle energy by inducing showering in its dense material layers. The three main parts are the central calorimeter (CC), which encircles the interaction region up to  $|\eta| \approx 1$ , and the two end calorimeters extending to  $|\eta| \approx 5$ , which are called ECN and ECS at the north and south ends. Each is enclosed in a separate cryostat. There is some detector coverage between the main calorimeters from the massless gaps (CCMG and ECMG) and intercryostat detector (ICD). All of the calorimeter detector systems are from Run I except the ICD.

## Calorimeter geometry

The fine segmentation of the calorimeter allows shower position and shape measurement. Radially, it is several layers deep: starting from the inside these are the *electromagnetic* section (EM) which has 4 layers; the *fine hadronic* section (FH) with 2 – 4 layers; and the *coarse hadronic* section (CH) which has 1 – 3 layers. Each layer is divided into small units called cells. Most cells have an area  $\Delta\eta \times \Delta\phi = 0.1 \times 0.1$ . This geometry, with *towers* of cells radiating from the centre of the detector, is known as pseudo-projective because the cells lie along lines of pseudorapidity but their boundaries do not (Fig. 3.6).

Each cell has the unique detector coordinates (*layer*, *ieta*, *iphi*), where *ieta* and *iphi* are integers corresponding to location in  $\eta$  and  $\phi$ . In general, each *ieta* value corresponds to a detector  $\eta$  width of  $\Delta\eta = 0.1$ . The range is from  $-37$  to  $37$  with no null value. Similarly, *iphi* ranges from  $1$  –  $64$  and each integer corresponds to a detector  $\phi$  width  $\Delta\phi = 2\pi/64 \approx 0.1$ . There are two regions where the cells have different sizes. In the forward region  $|\eta| > 3.2$  the cells are larger in  $\Delta\eta$  because of the diminishing physical size of pseudorapidity units (Table 3.1), and their azimuthal width doubles to  $\Delta\phi = 0.2$ . In the central region  $|\eta| < 2.6$  the third EM layer is divided more finely with  $\Delta\eta \times \Delta\phi = 0.05 \times 0.05$ . This is to define the EM showers more precisely at the depth of their maximum energy deposition.

Figure 3.7 illustrates the calorimeter geometry. Towers are drawn as an *ieta*–*layer* projection, demonstrating the correspondence between *ieta* and detector  $\eta$  and the coverage of the various layers. The CCCH is the central calorimeter coarse hadronic region. The end calorimeter hadronic region has three concentric cylinders around the beam pipe: the inner module (ECIH) at highest pseudorapidity,

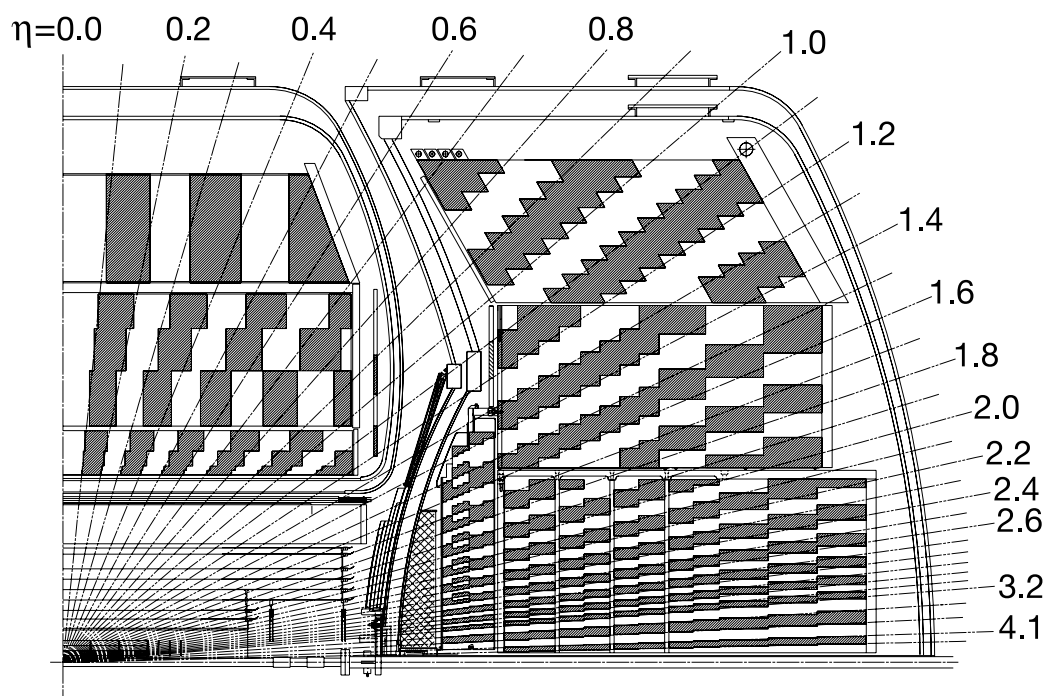


Figure 3.6: The calorimeter (quarter cut-away view)

$ i\eta $	$ \eta $ range
1	0.0 – 0.1
2	0.1 – 0.2
..	..
32	3.1 – 3.2
33	3.2 – 3.42
34	3.42 – 3.7
35	3.7 – 4.1
36	4.1 – 4.45
37	4.45 – 5.2

Table 3.1: Pseudorapidity coordinate  $i\eta$  in the calorimeter

which has up to four hadronic layers and one coarse hadronic layer, the middle module (ECMH) which has four fine hadronic layers and one coarse hadronic layer, and the outer module (ECOH) which has up to three coarse layers.

The calorimeter has the furthest reach in pseudorapidity of all the central DØ systems. Only the Forward Proton Detector (Sec. 3.2.6) has higher  $\eta$  coverage. As shown in Figure 3.7, the EM layers extend to  $|\eta| = 4.1$ , the first two FH layers to  $|\eta| = 4.45$ , and the last two FH layers and one CH layer extend to  $|\eta| = 5.2$ .

### Calorimeter Cells

A typical calorimeter cell is shown in Figure 3.8. The cell is filled with liquid argon, with an absorber plate connected to ground and a readout plate at +2.0 kV. A charged particle passing through the cell leaves a trail of ionisation in the liquid

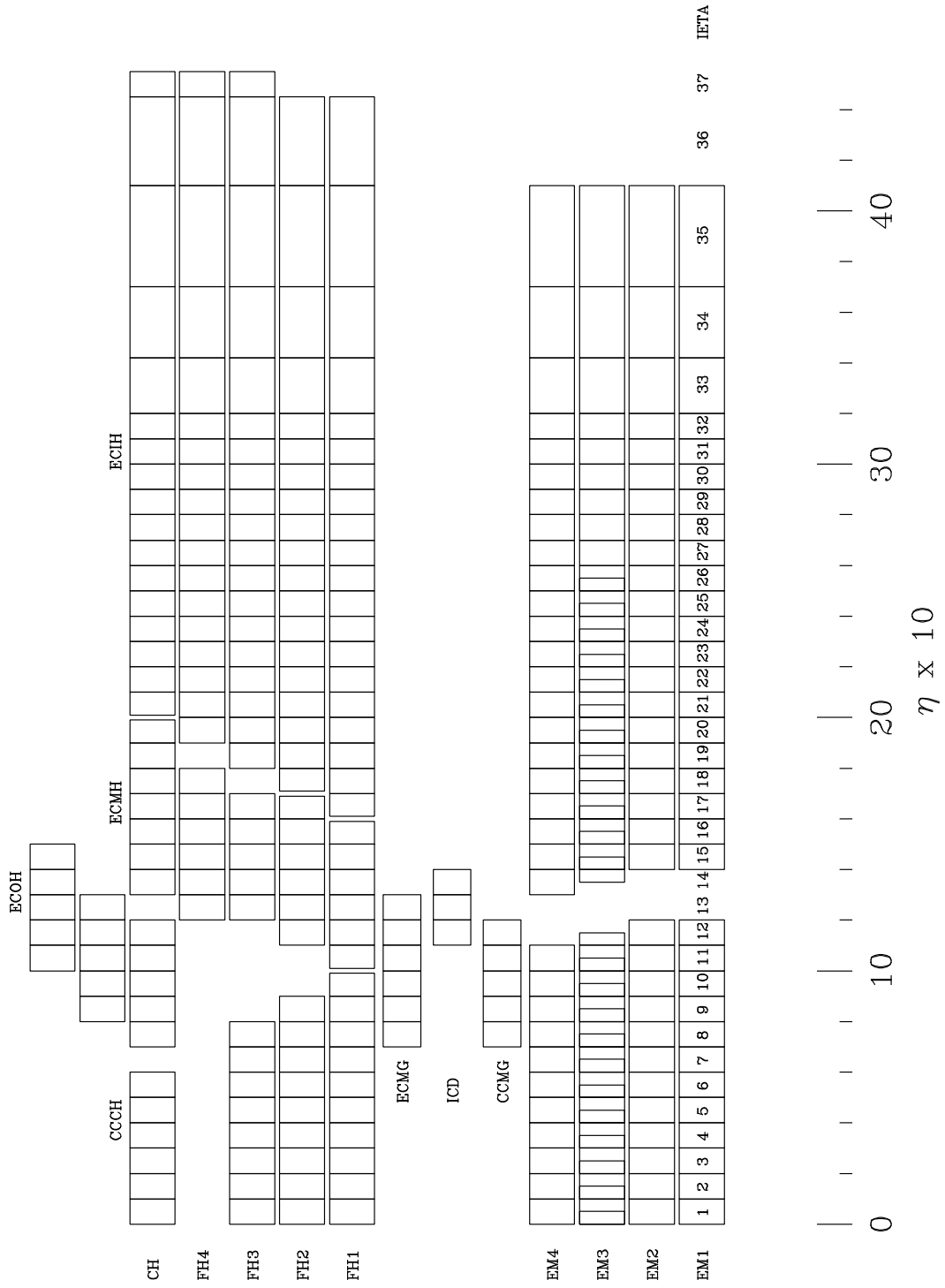


Figure 3.7: Projection of the calorimeter towers in the  $i\eta$  - layer plane

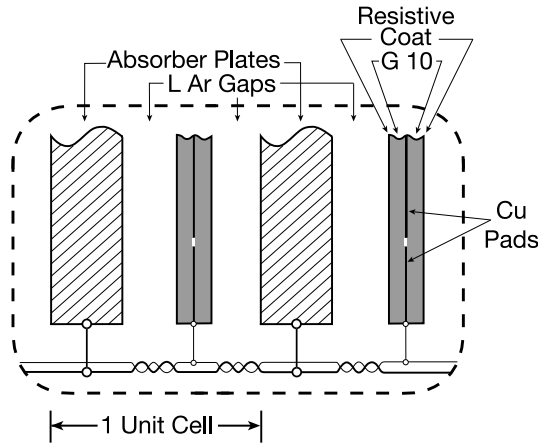


Figure 3.8: A typical calorimeter cell

argon, and the electrons drift to the readout plate. The dense absorber induces showering so all the energy of the incident particle is measured. The absorber in the EM is uranium, in the FH it is uranium-niobium alloy, and in the central and end CH it is copper and stainless steel respectively. The liquid argon gaps are 2.3 mm wide, with an electron drift time of 450 ns. The absorber plates are 3-6 mm wide in the EM and FH layers and about 47 mm wide in the CH so as to ensure all the energy is sampled within the calorimeter. For the readout, drift electrons induce a charge on copper pads etched onto a fiberglass board (G10) with a resistive coat of epoxy.

### Calorimeter electronics

Each calorimeter cell is a capacitor. The charge is sent to a preamplifier which amplifies and shapes the signal so that all channels have a similar shape: the charge rises during the drift time 450 ns and decays over a period of about  $15 \mu s$ , which is about three quarters of the Tevatron cycle. The drift time is longer than

the bunch spacing (396 ns), and all of the calorimeter electronics are new for Run II to meet the demands of the increased crossing rate.

The preamplifier output is sent to a baseline subtractor (BLS) board, which performs several functions. A shaper circuit takes the first two thirds (260 ns) of the signal and produces a shorter signal that peaks 320 ns after the interaction and decays over three bunch crossing (BX) periods. The shaper signal is sampled every tick (132 ns) with every third sample occurring at the peak. The samples are used for baseline subtraction. Baseline subtraction compensates for pile-up, which is signal from previous interactions. The baseline is the stored sample from the previous bunch crossing, three ticks before the current signal. The subtraction can result in negative energy signals for the channel. The BLS board sends the signal to be digitized for readout.

Cells are subjected to *zero suppression* to reduce the amount of information recorded for each interaction. Each cell is monitored during beam collision time, and the signal is only stored if it is at least  $1.5\sigma$  from the mean of the noise. During data processing the ‘T42’ algorithm performs a more sophisticated level of suppression [45]. Cell are kept if the signal is  $4\sigma$  from the mean, or if they are a nearest neighbour of these with a signal  $2.5\sigma$  from the mean. Cells with negative energies are discarded.

### **Massless gaps and intercryostat detector**

The massless gaps are individual calorimeter cells positioned inside the cryostats before the first absorber layers. They cover the region  $0.8 \lesssim |\eta| \lesssim 1.4$ . The intercryostat detector (ICD) is mounted on the calorimeter end caps in the region

$1.1 < |\eta| < 1.4$ . It is made of scintillating tiles, which are read out by wavelength shifting fibres connected to photomultiplier tubes (PMTs). The massless gaps and ICD provide information on shower energy in the regions between the central and end calorimeters.

### 3.2.4 Luminosity Monitor

The Luminosity Monitor (LM) detects charged particles in the forward region to determine the luminosity of the experiment. It comprises two detectors and a logic system. Each of the detectors is an array of 24 plastic scintillator wedges and photomultiplier tubes (Fig. 3.9) situated near the beam pipe at approximately  $\pm 140$  cm from the centre of DØ. They are mounted on the calorimeter end caps (Fig. 3.4) and cover the pseudorapidity region  $2.7 < |\eta| < 4.4$ . Chapter 4 describes the first measurement of the LM efficiency for Run II.

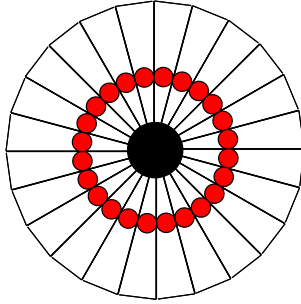


Figure 3.9: One detector of the Luminosity Monitor ( $r$ - $\phi$  view), showing the scintillator wedges, photomultiplier tubes and central beam pipe



### 3.2.5 Muon detector system

The muon system is the outermost detector system. It is cuboid with three layers named A, B and C, where A is the innermost, and toroid magnets between the A and B layers. There are layers of scintillators for timing measurements and wire drift chambers for tracking. It is divided into a central region ( $|\eta| < 1.0$ ) and two forward regions ( $1.0 < |\eta| < 2.0$ ).

The tracking system comprises proportional drift tube (PDT) detectors in the central region, mini drift tube (MDT) detectors in the forward region, and the toroid magnets. The tubes are arranged inside large drift chambers (Fig. 3.10). Each chamber in the A-layer has four decks of tubes, except those in the bottom A-layer which have three, and chambers in the B- and C-layers have three decks. There is a region in the bottom A-layer, with  $4.25 < \phi < 5.15$  and  $|\eta| \lesssim 1.25$ , which has no detectors due to the calorimeter support structure.

PDT detectors are aluminium enclosures with an anode wire at the centre (at 4.7 kV) and two cathode pads above and below (at 2.3 kV), filled with a gas mixture that is predominantly argon. The MDT detectors are tubes with eight anode wires and an outer cathode structure at  $-3.2$  kV. They are filled with a gas mixture that is predominantly tetrafluoromethane. Charged particles ionise the gas and electrons drift to the anodes. Signals from the anode wires are amplified, discriminated, and sent to digitisation boards.

The central toroid is a square annulus surrounding the central A-layers, about 3 m from the beam pipe and over a metre thick. The end toroids are squares with dimensions  $8\text{ m} \times 8\text{ m} \times 1.5\text{ m}$ . The magnetic field is about 1.8 T.

Hits in the muon tracking system are combined with information from the cen-

tral tracker to identify muons and measure their momenta in the presence of the toroidal magnetic field. The A-layer hits are matched to a central track to confirm the muon position, and compared with hits in the B and C layers to determine the path deflection. Thus the muon system provides muon identification and an independent measurement of the momentum from the central tracking system.

The scintillating counters are finely segmented detectors that are used for triggering and for rejecting ‘out-of-time’ backgrounds. In the central region there are two groups: in the A-layer are the *A $\phi$  counters*, and in the C-layer and bottom section of the B-layer there are the *outer counters*. In the forward region there are *pixel counters* in all three layers. Each counter is a sheet of scintillator that emits blue light, with embedded wavelength shifting fibres (or bars, in the pixel counters) to transport the light to photomultiplier tubes.

Two sources of out-of-time backgrounds are early hits from upstream beam losses in the tunnel, and late hits from beam remnants scattering off the edges of the calorimeter. The scintillator counters provide absolute time measurements to reject these signals. In addition, muons originating from cosmic rays can come through the detector at any time. They hit the upper part of the detector and then the lower, in contrast to muons from a collision which hit the upper and lower sections at the same time, and can be rejected by requiring the difference between the scintillator times measured in the upper and lower sections to be approximately zero.

The muon system is protected from upstream showering in the beam pipe with shielding made from iron, polystyrene and lead. The shielding extends from the outer edge of the calorimeter to the end of the DØ collision hall.

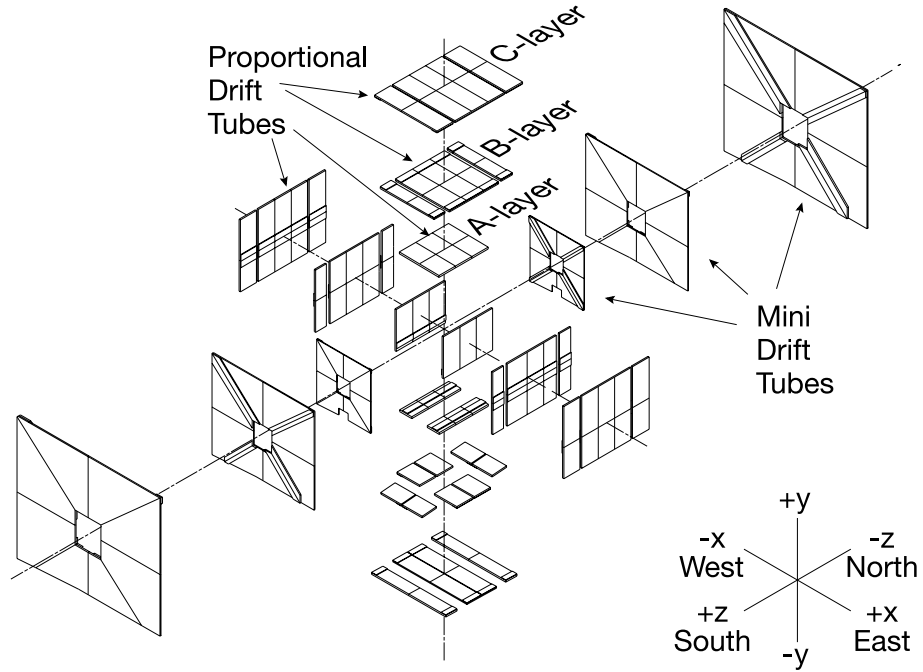


Figure 3.10: Exploded view of the muon tracking chambers

### 3.2.6 Forward Proton Detector

The Forward Proton Detector (FPD) detects intact protons from elastic and diffractive scattering. It is a series of momentum spectrometers that make use of accelerator magnets in conjunction with position detectors along the beam line [46]. In total the FPD has nine spectrometers, each comprising two scintillating fibre tracking detectors, that can be moved to within a few millimetres of the beam. Reconstructed particle four-vectors are used to calculate  $\xi$  and  $t$  of the scattered protons (Section 2). The FPD has been used in measuring  $d\sigma/dt$  for elastic scattering [47], and is currently being commissioned for use in diffractive analyses.

### 3.3 Triggering

The DØ trigger system selects events from the collision rate of 1.7 MHz to be written to tape at a rate of 50 Hz. An event is a bunch crossing time window in which the detector signals are read out, in which there may or may not be an interaction. There are three trigger stages with increasing levels of sophistication and decreasing event acceptance rates.

The first stage is Level 1 (L1), a fast hardware trigger with 256 binary channels called the L1 And/Or terms. Each has a loose (unrestrictive) requirement such as a small amount of energy in the calorimeter or a few tracking hits, and if the condition is met the channel is set to unity. The terms can be combined for more complicated requirements. The Level 1 decisions reduce the event rate to about 1.5 kHz. Events accepted at L1 pass to Level 2, which reconstructs simple physics objects from different sub-detectors and reduces the event rate further to about 850 Hz [48]. Events accepted at L2 have all the detector elements read out for the Level 3 decision. The L3 algorithms for reconstructing physics objects are similar to those used in offline reconstruction for physics analysis.

Triggers combine requirements from one or more of these levels to select different types of interaction. Every trigger includes three L1 *exposure* terms, which ensure the event is within a bunch crossing time window, that L1 is ready to make a decision, and that zero suppression is enabled in the calorimeter. Most physics triggers require several other terms. Four examples are described below. The first two are used by the experiment for measuring luminosity (Sec. 4.2) and all are used in this thesis.

**zero bias** The zero bias trigger selects events from random bunch crossings. This

trigger does not require beams to be colliding: empty bunch crossings are read out and can be used for detector noise studies.

**minimum bias** The minimum bias trigger requires that the L1 term *FastZ* is set, which is a coincidence in the Luminosity Monitor (described in Section 4). This trigger selects soft inelastic collisions.

**JT\_15TT** At L1, the JT\_15TT trigger requires two calorimeter trigger towers with  $E_T > 3$  GeV. Trigger towers are made from a fast readout of the calorimeter signals and have  $\Delta\eta \times \Delta\phi = 0.2 \times 0.2$ . This trigger also requires that at least one jet with  $E_T > 15$  GeV is found at L3.

**2MU\_A\_L2M0** The dimuon trigger 2MU\_A\_L2M0 requires two hits in the muon scintillators at L1, and at least one ‘medium’ quality muon (Section 5) found at L2.

The conditions for many triggers accept large numbers of events that would overwhelm the data storage rate, so there are *prescale* factors for these. Prescales reduce the rate by selecting a preset fraction of the events. These are changed for each trigger as the store progresses and the instantaneous luminosity decreases, to optimise the recorded rate for various types of interaction. All trigger term results are read out with the event information, and prescales are stored for luminosity calculations.

## Chapter 4

# Efficiency of the Luminosity Monitor

The primary purpose of the Luminosity Monitor (LM) is to count inelastic  $p\bar{p}$  collisions in order to calculate the integrated luminosity of the experiment. Diffractive physics analyses also use the LM output for triggering, to collect events with rapidity gaps. The LM system has been almost completely replaced for Run II. The two detectors are new, and the electronics remain from Run I with reduced functionality: previously the output included the number of sections hit on each side, but at the time of this analysis there is just a binary signal for each detector.

This section describes the first measurement of the efficiency of the Luminosity Monitor in Run II [49]. This contributed to an overall effort in 2003 to determine each factor in the luminosity calculation of the experiment [50].

## 4.1 LM And/Or Terms

The LM has two detectors, North and South, covering the range  $2.7 < |\eta| < 4.4$ . Each detector has 24 scintillator wedges with PMTs, from which the charge is summed, amplified and discriminated (converted to digital by applying a threshold). The signals are used as input for several Level 1 And/Or terms of which five are relevant here. Two correspond to the detectors  $N$  and  $S$ , referred to here as the *detector terms*. The others, *timing terms*, are assigned by the difference in time of arrival between the North and South signals.

If both detectors are hit the time difference gives the longitudinal position of the collision. For an interaction occurring at  $z_{vtx}$  the North and South signals arrive at

$$t_N = t_0 + \frac{l + z_{vtx}}{c}$$
$$t_S = t_0 + \frac{l - z_{vtx}}{c}$$

where  $l$  is the distance of the detectors from the centre of the interaction region (140 cm). The time difference  $\Delta t = t_N - t_S$  is proportional to the  $z$  position of the interaction,  $\Delta t = 2 z_{vtx} / c$ .

An inelastic collision at the centre of the interaction region has  $\Delta t \approx 0$ , and this is referred to as a *coincidence*. In this case the timing term called *FastZ* is set (‘fired’), which is used for the luminosity calculation, the minimum bias trigger and some other physics triggers. In addition  $z_{vtx}$  is stored in five And/Or terms, and if there are multiple interactions  $z_{vtx}$  is the average position of the vertices. When one detector signal arrives significantly before the other this is consistent with beam losses, known as halo. Losses occur when upstream beam particles scatter from residual gas molecules, other beam particles, or accelerator components,

causing showering into the DØ detector. Muons from these showers are very penetrating and they can hit both LM detectors. These events trigger the timing terms for halo: if South is hit before North it fires *AHalo*, and if North is first, it fires *PHalo*. Only the first hit to each detector is recorded so an event can fire at most only one of *FastZ*, *AHalo* or *PHalo*. A consequence is that if there is an early hit from beam losses before an inelastic collision the event is categorised as halo. There are gaps between the classification ranges, so some events in which both detectors were hit do not fire a timing term. The detector and timing terms are summarised in Table 4.1.

L1 term	Detectors fired	Vertex position (cm)
<i>N</i>	North	n/a
<i>S</i>	South	n/a
<i>FastZ</i>	North & South	$ z_{vtx}  < 97$
<i>AHalo</i>	North & South	$116 < z_{vtx} < 166$
<i>PHalo</i>	North & South	$-166 < z_{vtx} < -116$

Table 4.1: Luminosity Monitor L1 And/Or terms

## 4.2 Cross Sections and Luminosity

A cross section for a given type of interaction may be defined as

$$\sigma = \frac{dN}{dt} \cdot \frac{1}{\mathcal{L}} \quad (4.1)$$

where  $dN/dt$  is the rate of interactions and  $\mathcal{L}$  is the instantaneous luminosity. Some of the parameters that affect the luminosity are experimental design choices



such as bunch crossing frequency, number of bunches, and ‘focal length’ of the quadrupole magnets next to the interaction region. Others vary by crossing, such as the number of beam particles per bunch, bunch length and transverse bunch size. The beam properties are not known sufficiently precisely to calculate the instantaneous luminosity so it is measured with the LM from collision data.

Determining instantaneous luminosity uses Eq. 4.1 for inelastic  $p\bar{p}$  collisions:

$$\mathcal{L} = \frac{1}{\sigma_{eff}} \frac{dN_{meas}}{dt}$$

where  $\sigma_{eff}$  is the effective inelastic cross section, known at DØ as the luminosity constant, and  $dN_{meas}/dt$  is the rate of inelastic collisions measured with the *FastZ* term. The effective cross section includes factors for the LM efficiency  $\varepsilon_{LM}$  and geometric acceptance  $A_{LM}$ ,

$$\sigma_{eff} = \varepsilon_{LM} A_{LM} \sigma_{inel} .$$

Instantaneous luminosity decreases during a store because the number of beam particles decreases. It is calculated in units of time called luminosity blocks (LB), which are 60 or fewer seconds long. Over this short time it is assumed that the instantaneous luminosity is constant, so the expression  $\int \mathcal{L} dt = \mathcal{L} \Delta t$  holds for each tick in each LB. Many ticks have no beam, but ticks that do have beam have different luminosities because the number of beam particles in each bunch varies. The rate of interactions in a particular tick in an LB is given by

$$\left( \frac{dN_{meas}}{dt} \right)_{tick, LB} = \mu_{tick, LB} \times f$$

where  $\mu$  is the average number of interactions per tick and  $f$  is the frequency of the tick, the Tevatron rotational frequency 47.8 kHz. The average number of

interactions per tick is derived from the *FastZ* rate through Poisson statistics, because the number of times that *FastZ* fires in a tick over one LB is a measure of the probability of at least one interaction occuring,

$$\left( \frac{N_{FastZ}}{N_{ticks}} \right)_{tick, LB} = P(n > 0) ,$$

where  $n$  is the number of interactions, and this is related to  $\mu$  with

$$P(n) = \frac{\mu^n}{n!} e^{-\mu}$$

$$P(n > 0) = 1 - P(0) = 1 - e^{-\mu} .$$

So the integrated luminosity for a LB is a sum over all the ticks, calculated with the *FastZ* rate in each tick and the luminosity constant. For a cross section measurement all the luminosity blocks that the analysis triggers are exposed to are added together, taking into account the prescale factors of the triggers, to give the total integrated luminosity. Luminosity blocks are too small for normal reference to data periods, so the next largest unit is the *run*. A run is up to four hours in length, but may be shorter if beam or detector conditions necessitate a break in recording data. A store is about one day in length.

The measurement of the LM efficiency is described here. The determination of the acceptance and inelastic cross section are included for completeness.

### 4.2.1 Inelastic $p\bar{p}$ cross section

Inelastic  $p\bar{p}$  interactions may be divided into the following categories, which have different characteristics with respect to proton dissociation and rapidity gaps:

**Single Diffraction (SD)**  $p + \bar{p} \rightarrow p + X$  (and charge conjugate)

In single diffraction, one of the protons emits a pomeron and stays intact, and the pomeron scatters with the other beam proton. The particles in the system  $X$  are boosted along the collision axis, and there is a forward rapidity gap in the region of the intact proton (Fig. 4.1(a)).

**Double Diffraction (DD)**  $p + \bar{p} \rightarrow X + Y$

Double diffractive interactions have a central rapidity gap: a pomeron is exchanged and both protons dissociate (Fig. 4.1(b)).

**Double Pomeron Exchange**  $p + \bar{p} \rightarrow p + X + \bar{p}$

In double pomeron exchange both protons emit a pomeron and remain intact. The two pomerons scatter, producing a central system with rapidity gaps in both forward directions.

**Non-diffractive (ND)**  $p + \bar{p} \rightarrow X$

In non-diffractive interactions, both protons dissociate and particles are produced without any rapidity gaps.

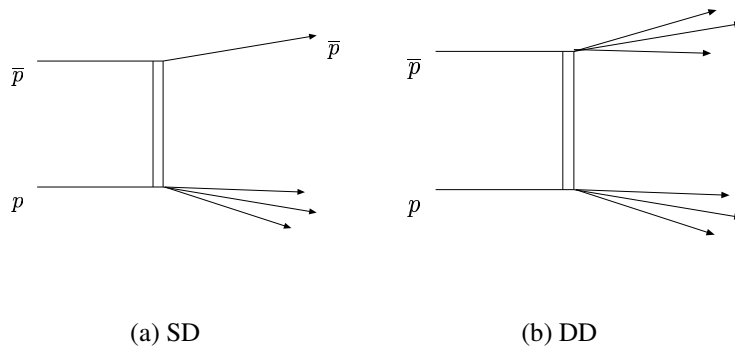


Figure 4.1: Diagrams of single diffraction and double diffraction

The inelastic  $p\bar{p}$  cross section is determined from measurements at  $\sqrt{s} = 1.8$  TeV by the E811 and CDF experiments at Fermilab. The two disagree at the level of  $2.8\sigma$  [50] and are averaged using the PDG prescription for non-compatible measurements. The average is scaled to  $\sqrt{s} = 1.96$  TeV with the result

$$\sigma_{inel} = (60.7 \pm 2.4) \text{ mb } (\sqrt{s} = 1.96 \text{ TeV}) .$$

Details are in [51].

The CDF experiment measured two components of the inelastic cross section, for single diffractive and double diffractive interactions:

$$\sigma_{SD} = (9.6 \pm 0.5) \text{ mb } (\sqrt{s} = 1.8 \text{ TeV})$$

$$\sigma_{DD} = (7.2 \pm 2.0) \text{ mb } (\sqrt{s} = 1.8 \text{ TeV})$$

These were not scaled to 1.96 TeV because the uncertainties are larger than the scaling factor, and the energy dependence of diffractive cross sections was considered to be not sufficiently well understood.

### 4.2.2 LM acceptance

The LM acceptance is defined as the fraction of inelastic events in which at least one charged particle hits each detector, and it is calculated with Monte Carlo event generators. Acceptance varies from process to process because of the different number and rapidity distributions of particles. The inelastic cross section is divided into three parts: single diffractive (SD), double diffractive (DD) and non-diffractive (ND). It is assumed there is negligible acceptance for double pomeron exchange. Thus the acceptance is defined as

$$A_{LM}\sigma_{inel} = A_{SD}\sigma_{SD} + A_{DD}\sigma_{DD} + A_{ND}\sigma_{ND}$$

where the non-diffractive cross section is  $\sigma_{ND} = \sigma_{inel} - \sigma_{SD} - \sigma_{DD}$ .

The acceptances are determined using an average of two Monte Carlo generators: PYTHIA [52] with the full detector simulation, and MBR [53] with a parameterised detector model. The results are in Table 4.2. The single diffraction acceptance is reasonably large, because the rapidity gap can be smaller than the range of the LM and because particles can scatter into the gap. The result for the cross section times acceptance is

$$A \sigma = 50.58 \pm 3.01 \text{ mb}.$$

Process	Acceptance
Non-Diffractive	$0.982 \pm 0.013$
Single Diffractive	$0.313 \pm 0.137$
Double Diffractive	$0.624 \pm 0.130$

Table 4.2: LM detector acceptances for different components of the inelastic  $p\bar{p}$  cross section. The uncertainties are assigned according to the various predictions of the Monte Carlos used [50].

### 4.3 LM Efficiency

The LM efficiency is the fraction of inelastic events within acceptance in which *FastZ* fires, which includes two components. The first is the *detector efficiency* for the charge from a particle hitting the North or South detector to pass the discrimination threshold (Section 4.3.1). The second is the efficiency, in events in

which both detectors fire, for the vertex to be reconstructed within the  $\pm 97$  cm range of *FastZ*. This is the *classification efficiency* (Section 4.3.4).

### 4.3.1 Detector efficiencies

Events are determined to be within acceptance by using the calorimeter to measure energy deposited behind each LM detector. The energy of a cell is added to the forward energy sum  $E_{\text{sum}}$  (North or South) if it passes the following selection requirements:

- EM layers
- $2.7 < |\eta_{\text{cell}}| < 4.1$
- $E_{\text{cell}} > 100$  MeV.

The data were collected with the zero bias trigger during the period 24<sup>th</sup> April – 24<sup>th</sup> June 2003. Runs defined as bad by the Jet/Missing  $E_T$  and Calorimeter groups are excluded, leaving a data sample of about 1.6 M events. Events that fire *PHalo* or *AHalo* are also excluded.

The events are divided into the four possible combinations of North and South detector signals. These are classified as follows: firstly, in the  $N \cdot S$  events both detector terms have fired and thus are defined as efficient. In  $N \cdot \bar{S}$  and  $\bar{N} \cdot S$  events either one of the detectors is inefficient or only one detector is hit; the latter are single diffractive interactions or empty bunch crossings in which halo hits one detector. The last group,  $\bar{N} \cdot \bar{S}$ , are empty bunch crossings and some inefficient events: both detectors inefficient, or single diffractive with one detector inefficient.

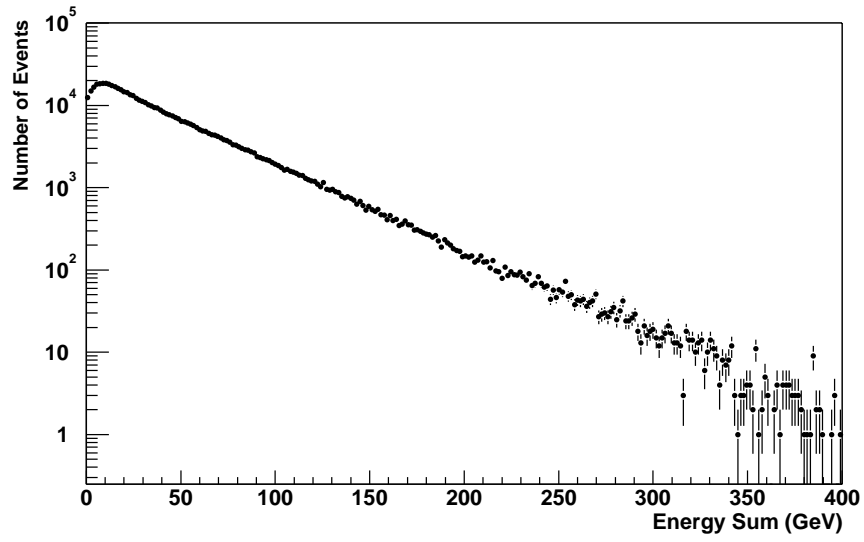
The categories are summarised in Table 4.3. They are referred to as the ‘efficient’, ‘inefficient+SD’ and ‘noise’ samples respectively.

Sample	A/O terms	Events
Efficient	$N \cdot S$	<ul style="list-style-type: none"> <li>• Both detectors efficient</li> </ul>
Inefficient+SD	$\overline{N} \cdot S$ $N \cdot \overline{S}$	<ul style="list-style-type: none"> <li>• One detector inefficient</li> <li>• SD hits one detector (not inefficient)</li> <li>• Halo hits one detector (not inefficient)</li> </ul>
Noise	$\overline{N} \cdot \overline{S}$	<ul style="list-style-type: none"> <li>• Both detectors inefficient</li> <li>• SD + one detector inefficient</li> <li>• Empty bunch crossing (not inefficient)</li> </ul>

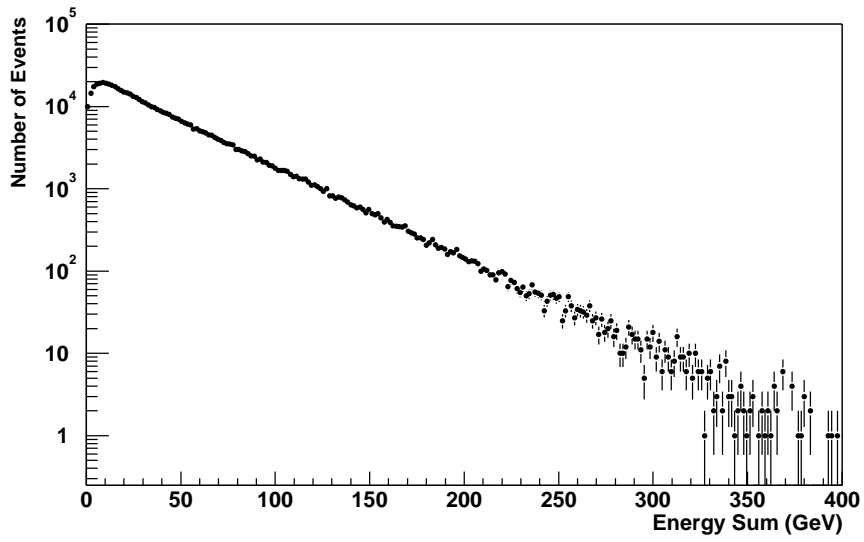
Table 4.3: Summary of event samples

The energy sum for efficient events is shown in Figure 4.2, with the North side in the upper figure and the South side below. The data extend to very high energies, and the distribution is exponential over most of the range.

The next group, inefficient+SD, are shown in Figure 4.3. The upper figure shows the North energy in  $\overline{N} \cdot S$  events, and the lower shows the South energy in  $N \cdot \overline{S}$  events. These are peaked at low energy and show a similar shape to the efficient sample in the rest of the range. It is a two component mixture: events with very little forward activity (single diffractive, or empty bunch crossings) and events with proton dissociation where the detector is inefficient. Overlaid on the figures are the North and South energy sums in the noise sample. This is dominated by events with very little forward energy. The noise distribution has been scaled such that the two are normalised at the first bin.



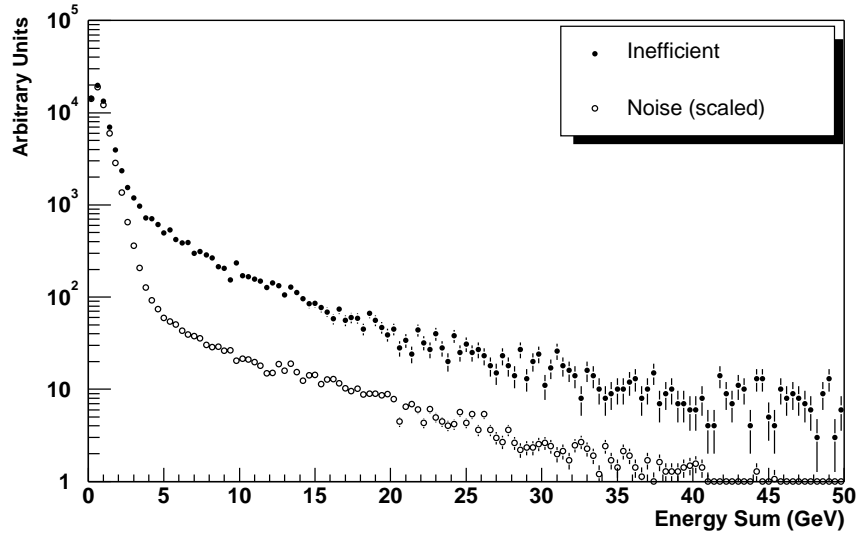
(a) North



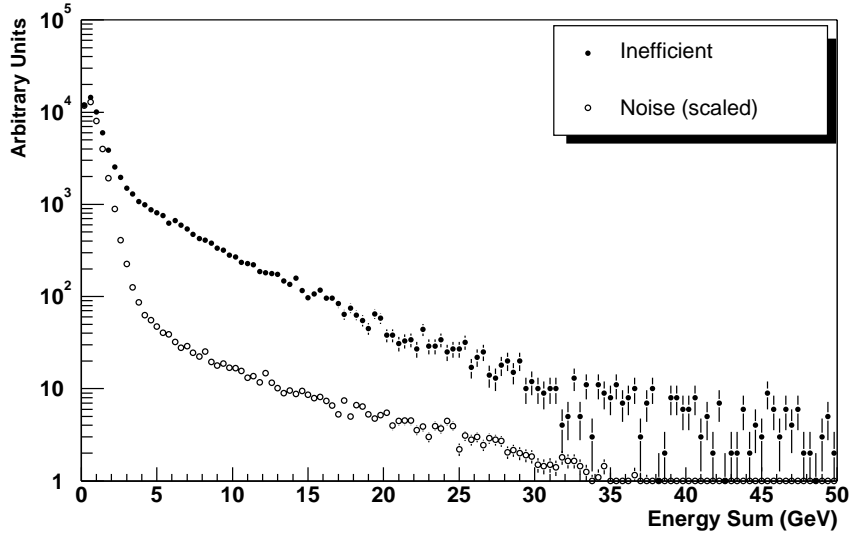
(b) South

Figure 4.2:  $E_{\text{sum}}$  for the efficient sample  $N \cdot S$





(a) North



(b) South

Figure 4.3:  $E_{\text{sum}}$  for the inefficient+SD samples (a)  $\overline{N} \cdot \overline{S}$  and (b)  $N \cdot \overline{S}$  and the noise sample  $\overline{N} \cdot \overline{S}$ , normalised at the first bin.

The number of inefficient events in the inefficient+SD samples is estimated in two ways which are described in the following sections.

### Subtraction method

In the first method the noise distribution is simply subtracted from the inefficient+SD distribution. The results are shown in Figure 4.4. The efficiency of the North detector given that the South is on,  $(\epsilon_{N,S})_{sub}$ , is calculated from the number of entries in the North subtracted distribution and the number in the efficient sample:

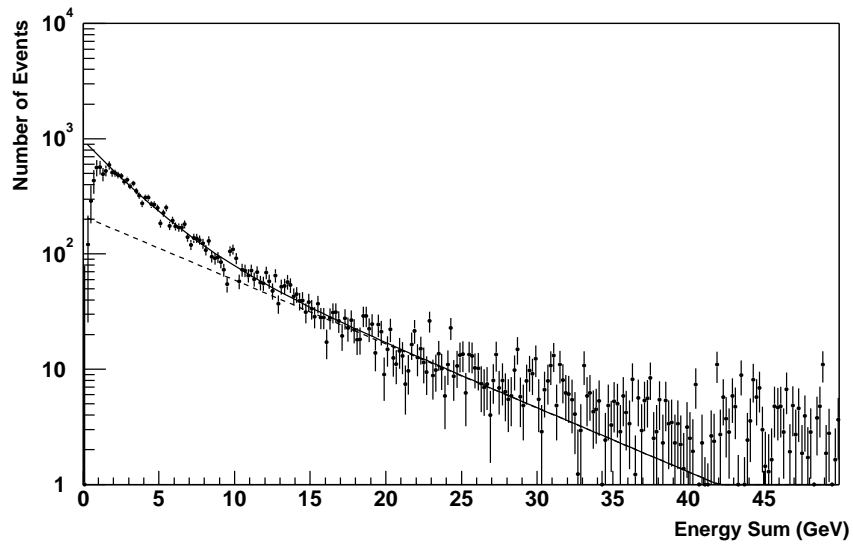
$$(\epsilon_{N,S})_{sub} = \frac{N_{\text{efficient}}}{N_{\text{efficient}} + N_{\text{North subtracted}}} . \quad (4.2)$$

This is referred to as the subtracted efficiency. It is similarly repeated for the South side.

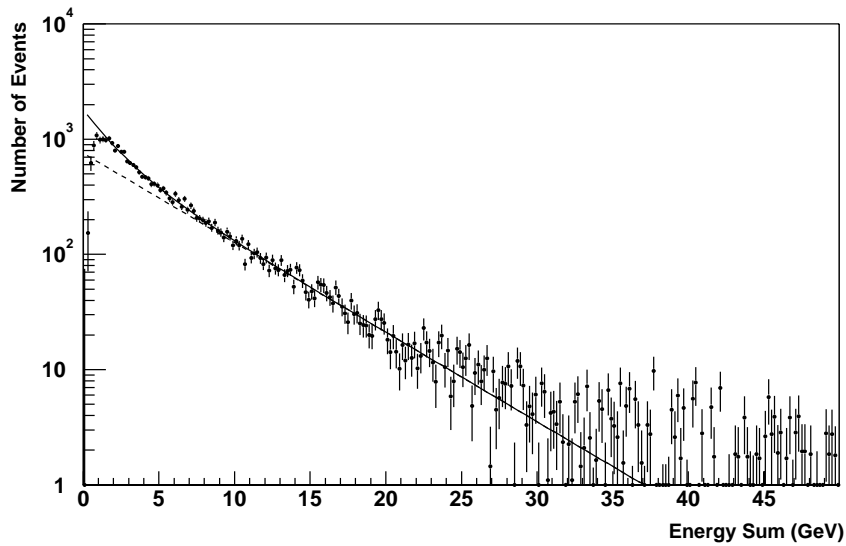
This is an upper limit for the efficiency. There may be some additional inefficient events that are not counted because their energies are below the calorimeter cell energy threshold. The next section describes the method to find the lower limit for the efficiency.

### Extrapolation method

The subtracted distribution is fitted with a sum of two exponentials over the range 1.5 – 20 GeV. The fit function is drawn in Figure 4.4 along with one of the exponentials to illustrate the change between the two. The function is extrapolated to the y-axis and in the region with  $E_{\text{sum}} < 1.5$  GeV the integral is used as the number of inefficient events. Above this boundary the integral of the histogram is used as before. The two parts are added together to give the extrapolated sample,



(a) North



(b) South

Figure 4.4:  $E_{\text{sum}}$  for the (a) North and (b) South subtracted histograms. The fit function is the sum of two exponentials, in the range 1.5-20 GeV. One exponential is shown as a dashed line.

from which the extrapolated efficiency  $(\varepsilon_{N,S})_{ext}$  is derived:

$$(\varepsilon_{N,S})_{ext} = \frac{N_{\text{efficient}}}{N_{\text{efficient}} + N_{\text{North extrapolated}}} .$$

The extrapolated and subtracted results are used as lower and upper bounds for the detector efficiencies:

$$96.6\% < \varepsilon_{N,S} < 97.2\%$$

$$94.7\% < \varepsilon_{S,N} < 95.6\% .$$

The bounds are used as an estimation of the systematic uncertainty; statistical uncertainties are an order of magnitude smaller.

### 4.3.2 Parameter variation

The stability of the measurement is checked with variations in the analysis. The first change excludes events from the noise sample that have a vertex. This is to ensure that the efficiency is not overestimated because real energy in the noise sample would give too large a subtraction from the inefficient+SD distribution, and the inefficient sample would be too small. A typical definition of a good primary vertex is one that has at least three matched tracks. In a sample of more than 0.8M  $\overline{N}\cdot\overline{S}$  events, none has a vertex that passes this requirement. Events that have vertices with two matched tracks are excluded from the sample and this has negligible effect on the result:

$$96.6\% < \varepsilon_{N,S} < 97.1\%$$

$$94.6\% < \varepsilon_{S,N} < 95.5\%$$

The parameters are varied for the energy sum and the bunch crossing position with respect to the superbunches. The bunch crossing position tests the effect of pile-up from previous interactions and the resulting baseline subtraction in the calorimeter. This can be different in the first and last ticks of the superbunches because of the varying probability of energy signals from previous interactions overlapping the event.

There are also variations in the subtraction method, by altering the bin used for normalising the two samples and the bin width of the distributions. Changing the bin for normalisation results in negative entries in the subtracted distribution, which are not included in the integration. The parameter sets are summarised below, and the results are shown in Fig. 4.5. The upper and lower limits of the error bars correspond to the subtraction and extrapolation methods respectively.

1. Original parameters
2. Events with vertices excluded from noise sample
3. Pseudorapidity range of  $E_{\text{sum}}$  is  $2.8 < |\eta| < 3.7$
4. Pseudorapidity range is  $2.6 < |\eta_{\text{cell}}| < 4.1$
5. Cell energy threshold is 50 MeV
6. Cell energy threshold is 200 MeV
7. First tick of superbunches
8. Last tick of superbunches
9. Normalise noise distribution to  $2^{\text{nd}}$  bin of inefficient+SD sample

10. Normalise noise distribution to 3<sup>rd</sup> bin
11. Normalise noise distribution to average of 1<sup>st</sup> and 2<sup>nd</sup> bin
12. Bin width is 100 MeV

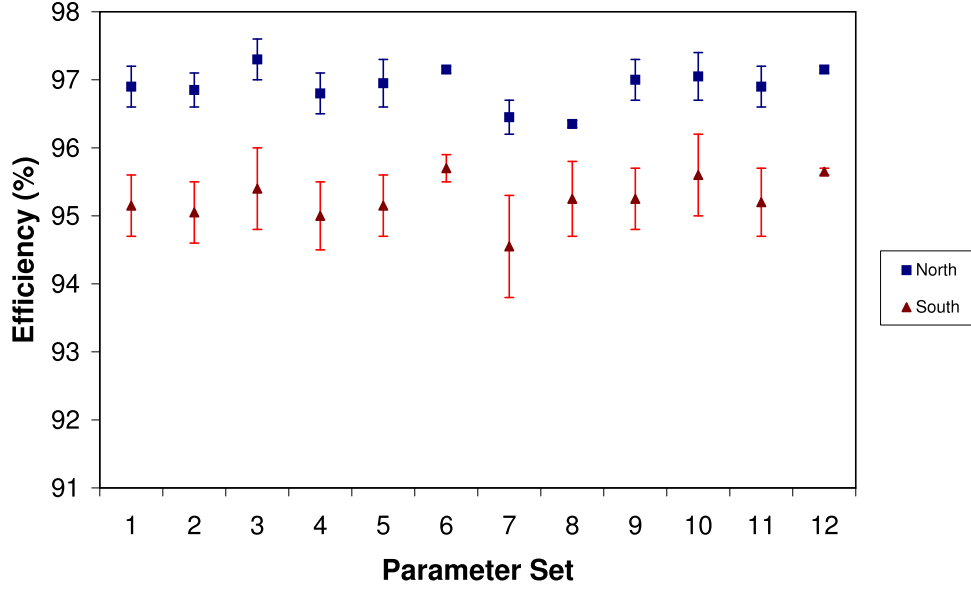


Figure 4.5: Effect of parameter variations on North and South detector efficiencies

The parameters of the extrapolation method, the fit range and the dividing line between integration of the fit function and histogram, are also varied (Fig. 4.6).

The results are consistent with the measurements shown in Fig. 4.5.

13. Fit range is 2.5–20 GeV
14. Fit range is 1.5–10 GeV
15. Fit range is 3.0–30 GeV

16. Integral boundary is 1.0 GeV

17. Integral boundary is 2.0 GeV

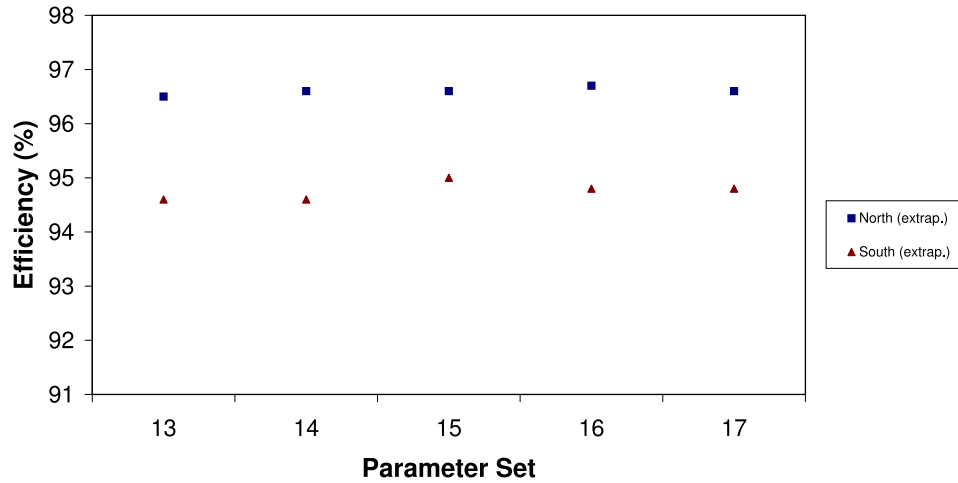


Figure 4.6: Effect of varying fit range and integration boundary on the lower limits of the North and South detector efficiencies

A study using earlier data indicates another component of the detector efficiency. This is the ‘electronics efficiency.’ Occasionally an error occurs in the detector signal path where the charge passes the discrimination threshold but the detector term is not set. This problem fortunately does not affect the timing terms. The dataset for the analysis described so far was taken after changes were made to the electronics to remove this inefficiency. The following analysis is carried out for three earlier time periods: in the first and second, no changes had been made; the second was after an experiment shutdown; and the third was after the change to the South term.

1. 21<sup>st</sup> April '02 – January '03 shutdown

2. January '03 shutdown – South detector term change
3. South detector term change – North detector term change

The results are shown in Fig. 4.7 and show the improvement in the South side efficiency during the third period. The North side efficiency is also improved between these measurements and those in the main analysis dataset. Only the main dataset is used for the detector efficiency measurements for the luminosity constant, because the electronics efficiency does not affect the *FastZ* term.

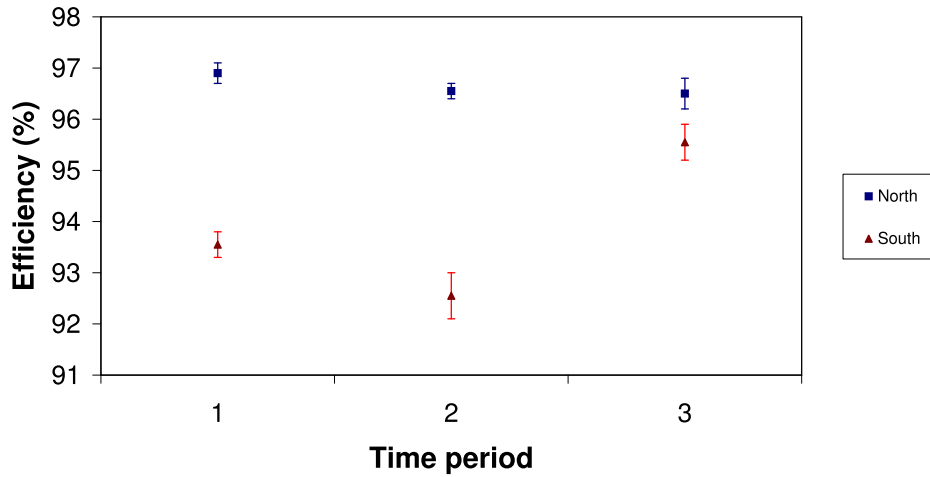


Figure 4.7: Single detector efficiency limits as a function of time

Two cross-checks for the LM detector efficiencies were performed with other methods using the calorimeter energy and found to be consistent with the results in Figs. 4.5 and 4.6 [50]. It was decided to take the range of these measurements as the systematic uncertainty, resulting in the values

$$\varepsilon_{N,S} = (97 \pm 1)\%$$



$$\varepsilon_{S,N} = (95 \pm 1.2)\%$$

for the individual LM detector efficiencies.

### 4.3.3 Combined detector efficiency

If the two detector efficiencies are uncorrelated it has no effect on one side if the other detector fired. The efficiency for the North side, with no requirement on the South, is given by Eq. 4.2 using additional components from events in which the South detector did not fire:

$$\varepsilon_N = \frac{N_{N,S} + N_{(N,\bar{S}) \text{ real}}}{N_{N,S} + N_{(N,\bar{S}) \text{ real}} + N_{(\bar{N},S) \text{ real}} + N_{(\bar{N},\bar{S}) \text{ real}}}$$

where  $N_{N,S}$  is the number of events with the North and South detectors on, and the suffix ‘real’ refers to the number of inefficient events in that sample. It is assumed that  $N_{(\bar{N},\bar{S}) \text{ real}} = 0$  because none of the events in this sample have a good vertex, and the other components have been determined as described. The results for the independent North and South efficiencies,  $\varepsilon_N$  and  $\varepsilon_S$ , are  $\varepsilon_N = 97.1\%$  and  $\varepsilon_S = 95.2\%$ . These are consistent with  $\varepsilon_{N,S}$  and  $\varepsilon_{S,N}$  so it can be assumed that the two sides are uncorrelated. The efficiency for both detectors to fire in events within acceptance is the product of the two efficiencies,  $\varepsilon_{NS} = 92 \pm 1.6\%$ .

### 4.3.4 Classification efficiency

If both detectors fire then 91.9% of events are classified as *FastZ*, 6.0% as *PHalo*, 0.5% as *AHalo* and 1.6% as none of these. The *AHalo* rate is much smaller than

the *PHalo* rate because the antiproton beam intensity is 1/10 that of the proton beam.

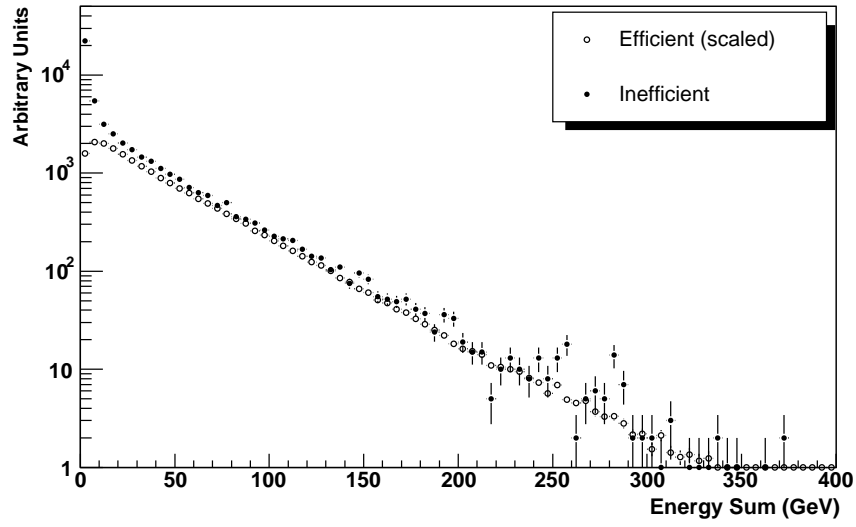
Events that do not fire *FastZ* are a mixture of inelastic collisions, when the vertex has  $|z_{vtx}| > 97$  cm or an early halo hit causes it to be misreconstructed there, and empty bunch crossings where halo particles hit both detectors. For the classification efficiency it is necessary to separate the inefficient events from the empty bunch crossings.

New event samples are defined: efficient events are  $N \cdot S \cdot FastZ$  and ‘inefficient+halo’ events are  $N \cdot S \cdot \overline{FastZ}$ . Figure 4.8 shows the energy distributions for these two sets of events. The efficient distribution is normalised to the inefficient+halo distribution in the high energy region. The normalisation scale is determined from an exponential fit of both distributions in the range 80 – 160 GeV, where the scale factor for the efficient sample is the ratio of the intercepts. The inefficient+halo sample has two components: a peak at low energy, from empty bunch crossings, and a high energy distribution from inelastic interactions. The number of real interactions is estimated as the number of events in the scaled efficient sample. The classification efficiency is

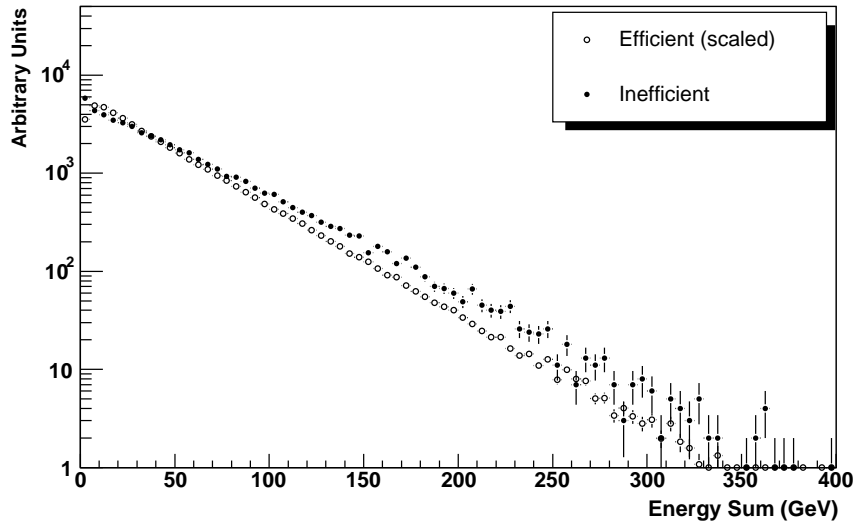
$$\epsilon_{Ncal} = \frac{N_{\text{efficient}}}{N_{\text{efficient}} + N_{\text{scaled efficient}}},$$

where the subscript *Ncal* refers to the side of the calorimeter used in the energy sum distributions. The results are in Table 4.4 for three different fit ranges.

The measurements using the South calorimeter are significantly lower than those using the North side. This is investigated by dividing the inefficient+halo sample into three: events that fire *PHalo*, *AHalo* or *none* of the timing terms respectively. The analysis is repeated on each of these samples to determine the source of the



(a) North



(b) South

Figure 4.8:  $E_{\text{sum}}$  for the  $N \cdot S \cdot \overline{\text{FastZ}}$  sample and the normalised efficient sample,  $N \cdot S \cdot \text{FastZ}$

Fit range (GeV)	$\epsilon_{Ncal}$ (%)	$\epsilon_{S cal}$ (%)
80-160	96.5	92.4
50-100	95.5	92.9
30-80	95.3	93.3

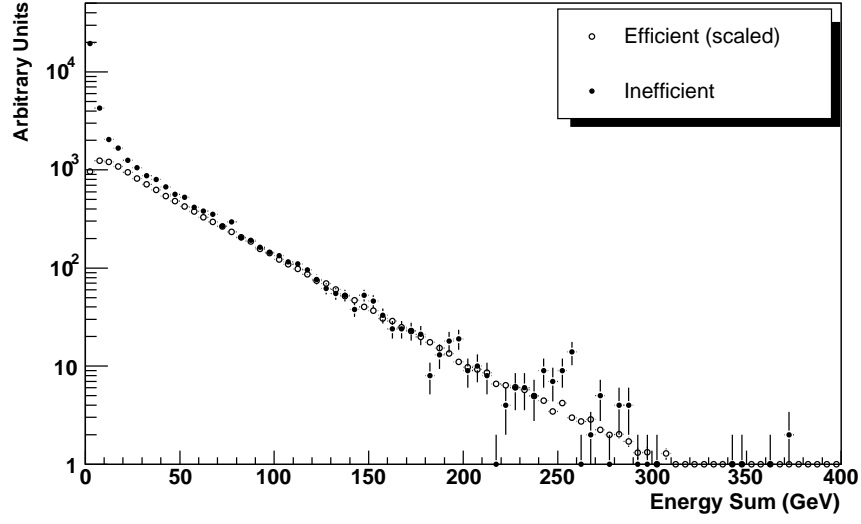
Table 4.4: Classification efficiencies measured using various fit ranges

asymmetry (Figs. 4.9-4.11). The fit range for each is 80-160 GeV. The results are given in Table 4.5.

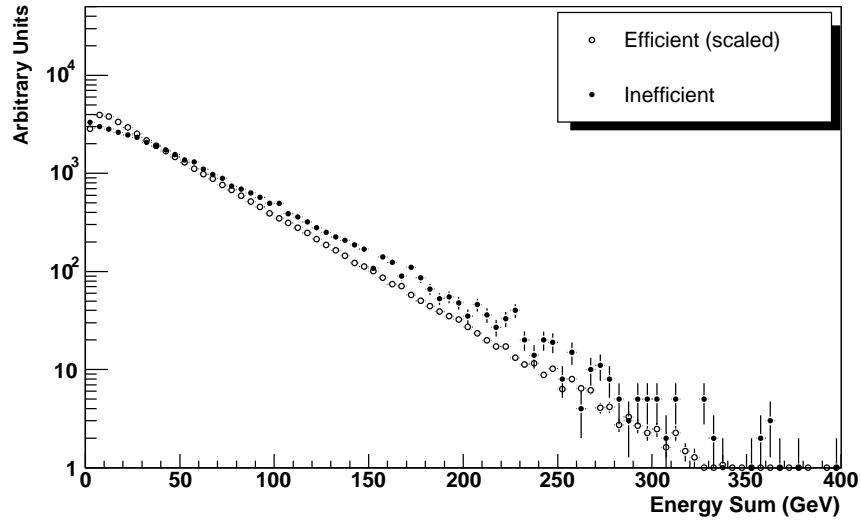
Inefficiency	$\epsilon_{Ncal}$ (%)	$\epsilon_{S cal}$ (%)
<i>PHalo</i>	97.8	93.7
<i>AHalo</i>	99.5	99.8
<i>none</i>	98.9	98.5

Table 4.5: Efficiencies due to events being misclassified as *PHalo*, *AHalo* or *none*

The largest source of the asymmetry is misclassification of events as proton halo. Fig. 4.9 shows that the energy in the South calorimeter in  $N \cdot S \cdot PHalo$  events is larger than in the North calorimeter, with no low energy peak. It may be that the empty bunch crossings in which *PHalo* fires are not empty in this region because proton beam losses produce additional showering and energy deposition in the outgoing proton (South) direction. This also seems to occur in the opposite direction in events that fire the *AHalo* term (Fig. 4.10). The events that fire none of the timing terms also show a small asymmetry consistent with the *PHalo* sample (Fig. 4.11). The misclassification rates are much smaller for the *AHalo* and *none* categories, so the asymmetry has a smaller effect.

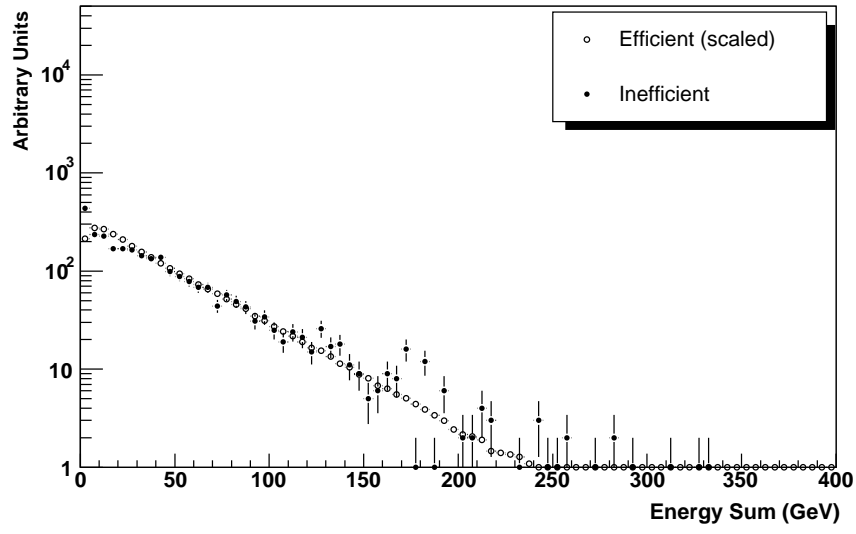


(a) North

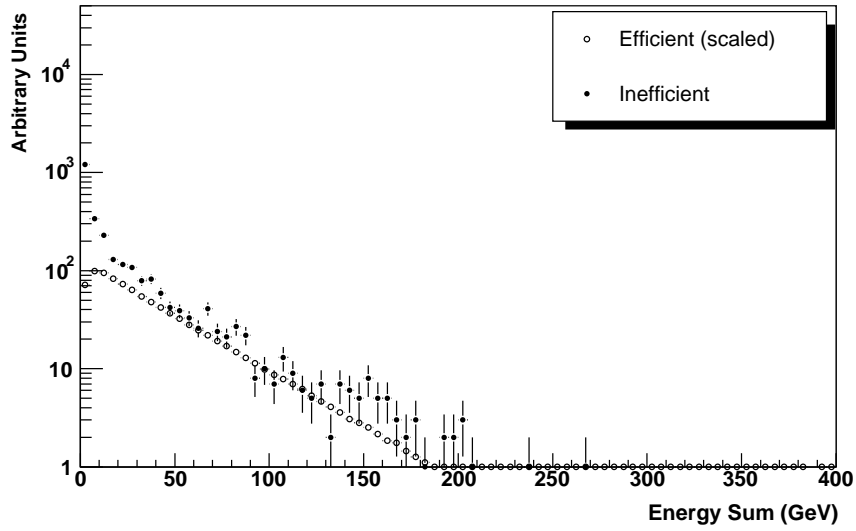


(b) South

Figure 4.9:  $E_{\text{sum}}$  for the  $N \cdot S \cdot PHalo$  sample and the normalised efficient sample,  $N \cdot S \cdot FastZ$

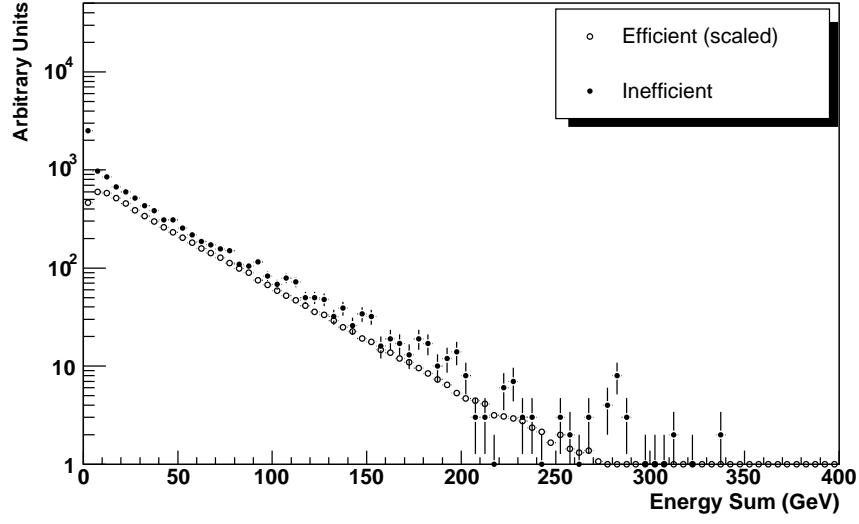


(a) North

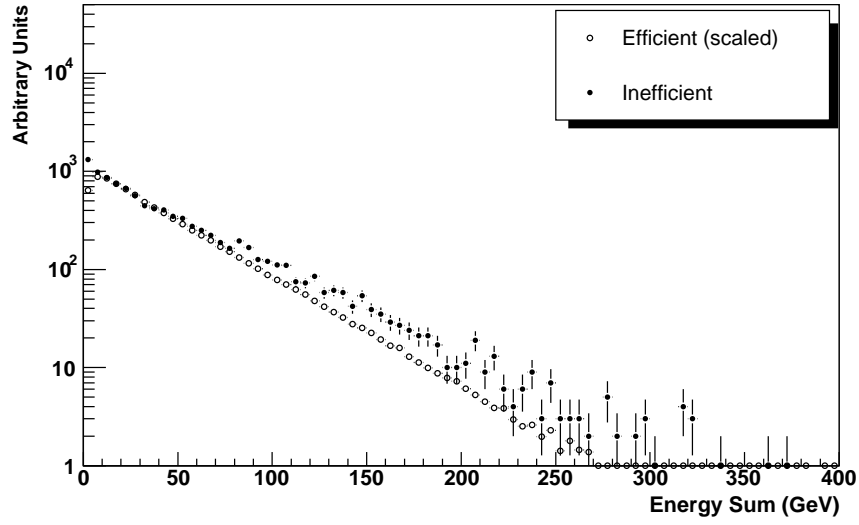


(b) South

Figure 4.10:  $E_{\text{sum}}$  for the  $N \cdot S \cdot AHalo$  sample and the normalised efficient sample,  $N \cdot S \cdot FastZ$



(a) North



(b) South

Figure 4.11:  $E_{\text{sum}}$  for the  $N \cdot S \cdot \text{none}$  sample and the normalised efficient sample,  $N \cdot S \cdot \text{FastZ}$ .

It was decided to treat the halo components of the classification efficiency separately and incorporate only the misclassification of events as *none* of the timing terms in the LM efficiency. The effect of halo in reducing the rate of events firing *FastZ* is corrected for online (during the store) [54]. A cross check of the classification efficiency using another method [50] gave results with a lower limit of 98.2%, and the median value of the range is used:  $\varepsilon_{class} = 98.6 \pm 0.4\%$ .

The LM efficiency is

$$\varepsilon_{LM} = \varepsilon_N \times \varepsilon_S \times \varepsilon_{class} = (90.9 \pm 1.8)\% ,$$

where the uncertainty includes an additional component for luminosity dependent effects [55]. The resulting luminosity constant is  $\sigma_{eff} = (46 \pm 3)$  mb, in which the largest part of the 6.5% uncertainty is from the total  $p\bar{p}$  cross section.



# Chapter 5

## Analysis of Diffractive $Z \rightarrow \mu^+ \mu^-$

### Interactions

This chapter describes the first search for diffractive  $Z$  boson production ( $p + \bar{p} \rightarrow p + Z + X$  and the charge conjugate) in the muon decay channel, and work towards the measurement of the cross section for this process. The fractional momentum loss of the intact proton is measured in  $Z \rightarrow \mu^+ \mu^-$  interactions, using the calorimeter and muon system and corrected with events simulated by POMWIG. The momentum loss is used to select diffractive candidate events. The efficiencies of the selection criteria and the background contamination rates are estimated, and the systematic uncertainties for these are explored. It is concluded that further work is required to understand the uncertainties before the cross section can be determined.

## 5.1 Z Boson Candidate Selection

### 5.1.1 Dataset

The data for this analysis were taken by the DØ detector during the period 27th February – 7th September 2003. Earlier data are not used for the analysis because the dimuon triggers at that time required that there were hits in the Luminosity Monitor which therefore vetoes diffractive events. The last date marks the beginning of a detector shutdown for which the experiment was halted for repairs and upgrades for a period of several weeks. The data period is the same as the third period in a recent  $Z \rightarrow \mu^+\mu^-$  analysis [56]. Data quality cuts are applied by excluding runs and luminosity blocks in which the SMT, CFT, calorimeter or muon detector systems are not functioning correctly or in which the integrated luminosity cannot be calculated. The total integrated luminosity is  $109 \pm 7 \text{ pb}^{-1}$ .

### 5.1.2 Selection Criteria

The selection criteria require that events have two muons of at least ‘loose’ quality [56] matched to two central detector tracks, and the following:

- Both muons are within the geometrical acceptance of the muon detector (defined below).
- $p_T > 15 \text{ GeV}$  for both muons.
- $M_{\mu\mu} > 40 \text{ GeV}$ , where  $M_{\mu\mu}$  is the dimuon invariant mass.

- At least one muon passes both of these isolation criteria, or both muons pass at least one of them:
  - The sum of the transverse momenta of all tracks in a cone of radius  $R = 0.5$  around the muon is required to be  $\Sigma_{tracks,i} p_T^i < 3.5$  GeV, where  $R = \sqrt{(\Delta\eta)^2 + (\Delta\phi)^2}$ .
  - The sum of the transverse energies of the calorimeter cells in an annular ring  $0.1 < R < 0.4$  around each muon is required to be  $\Sigma_{cells,i} E_T^i < 2.5$  GeV (EM and FH cells only).
- The muons have opposite charge.
- The acolinearity between the two muon tracks is limited to  $\Delta\alpha_{\mu\mu} > 0.05$  radians. Acolinearity is defined as  $\Delta\alpha_{\mu\mu} = |\Delta\phi_{\mu\mu} + \Delta\theta_{\mu\mu} - 2\pi|$
- The distance of closest approach  $dca$ , which is the distance of the muon track from the beam in the plane transverse to the beam, is limited to  $dca < 0.02$  cm for muon tracks with SMT hits and  $dca < 0.2$  cm for muon tracks with no SMT hits.
- The event fulfilled the requirements of one of a set of six dimuon triggers, 2MU\_A\_L2M0, 2MU\_A\_L2M0\_TRK(5,10), 2MU\_A\_L2M0\_L3L(6,15) and 2MU\_A\_L2ETAPHI, or the single muon trigger MUW\_W\_L2M3\_TRK10. The parentheses indicate a pair of trigger names, one with each of the specified endings; the trigger names are explained below.

The  $p_T$  of the muons is measured in the central tracking system, since this has a better resolution than the local muon detector measurement. If a muon track does

not have hits in the SMT detector the  $p_T$  is corrected by constraining the track to the  $(x,y,z)$  position of the beam.

The acceptance cuts exclude the parts of the muon detector with reduced coverage: the regions nearest the beampipe,  $|x_A| < 110$  cm and  $|y_A| < 110$  cm, where  $x_A$  and  $y_A$  are the  $x$  and  $y$  positions measured in the muon chamber A-layer, and the region of the bottom gap,  $4.25 < \phi < 5.15$  for  $|\eta_A| < 1.25$ , where  $\eta_A$  is also measured in the A-layer. The requirements on muon isolation reduce the background from  $b\bar{b}$  events in which muons are produced inside jets.

The acolinearity requirement reduces the background from cosmic ray muons, which enter the muon detector system from above. If a cosmic ray muon passes through the interaction region it can appear to be two tracks that originate from the beam pipe. The tracks are exactly back-to-back, with  $\Delta\phi = \Delta\theta = \pi$  radians, so the cut on acolinearity reduces the background from these events. The limit on the distance of closest approach,  $dca$ , also reduces the background from cosmic rays because it requires the distance between the muon tracks and the beam location to be small in the plane transverse to the beam.

The background contamination rates from  $Z \rightarrow \tau^+\tau^-$  events in which both taus decay to a muon,  $W \rightarrow \mu\nu$  events with an additional muon from a jet, and di-boson ( $WW$ ,  $WZ$ ,  $ZZ$ ) events are estimated in [56] and these are listed in Section 5.6.6.

In the muon trigger names, the abbreviations MU and 2MU refer to the requirements for one or two ‘tight’ muon signals found in the scintillator detectors at L1 respectively. The abbreviations A and W refer to the requirement that the signal may be anywhere or within  $|\eta| < 1.5$  respectively. Triggers that have L2M0 in the name require there is a ‘medium’ quality muon found at L2, and those with L2M3

also require that this muon has  $p_T > 3$  GeV. The name L2ETAPHI refers to the requirement that the event has two muons found at L2 that are well separated. The terms TRK(5,10) indicate that the event is required to have a central track found at L3 with  $p_T > (5, 10)$  GeV, and L3L(6,15) indicates that the event is required to have a muon found at L3 with  $p_T > (6, 15)$  GeV. [56]

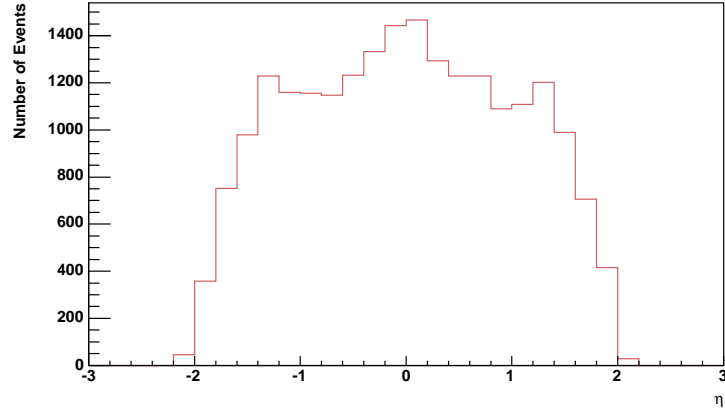
The number of selected  $Z$  boson candidates is 10794. The pseudorapidity and the invariant mass of the two highest  $p_T$  muons in the event are shown in Figs. 5.1(a) and Fig. 5.1(b), and the rapidity and  $p_T$  of the  $Z$  boson candidates are shown in Figs. 5.2(a) and 5.2(b). Events are referred to throughout as  $Z \rightarrow \mu^+\mu^-$  but these also include  $\gamma^* \rightarrow \mu^+\mu^-$  interactions.

## 5.2 Reconstructing the Momentum Loss

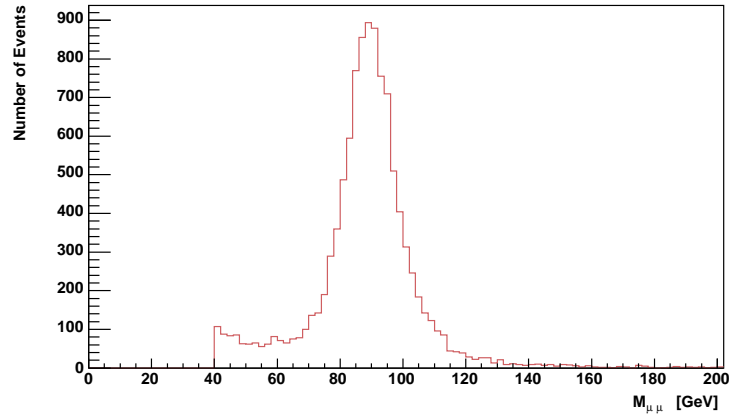
The momentum loss  $\xi$  of a beam particle is reconstructed from the final state using

$$\xi \approx \frac{\sum_i E_{Ti} e^{\pm\eta_i}}{\sqrt{s}}, \quad (5.1)$$

where  $i$  is an index over all particles except the intact beam particle, and the positive and negative signs are for the proton and antiproton beam respectively. The calorimeter and muon system are used to measure the final state; selection criteria for the detector signals are described in the following sections. The information from the calorimeter was not recorded in three of the 10794 events and these are excluded from the sample.

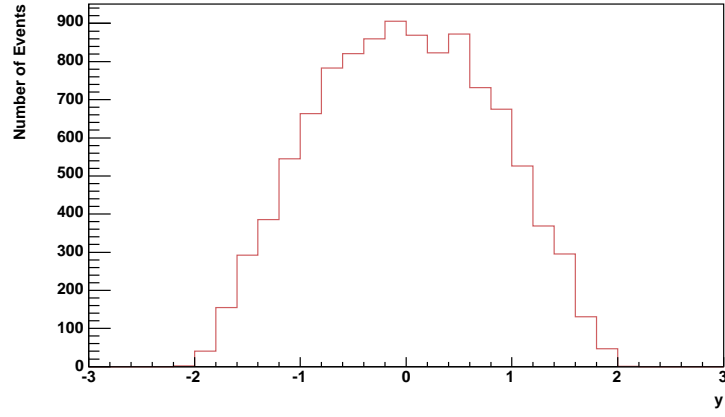


(a)

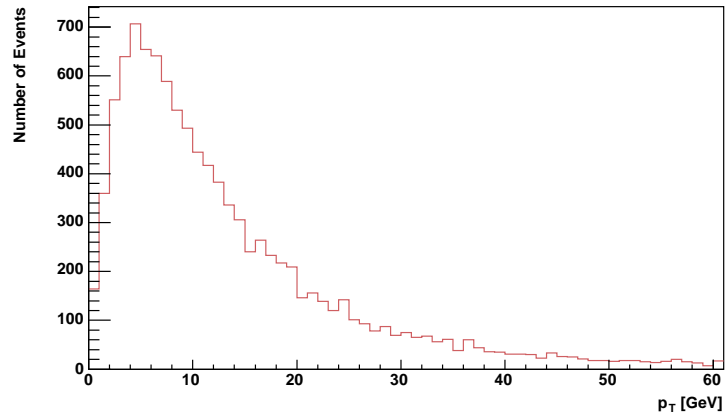


(b)

Figure 5.1:  $Z \rightarrow \mu^+\mu^-$  candidate events, showing the (a) pseudorapidity, with two entries per event, and (b) invariant mass of the two highest  $p_T$  muons



(a)



(b)

Figure 5.2:  $Z \rightarrow \mu^+\mu^-$  candidate events, showing the (a) rapidity and (b) transverse momentum of the  $Z$  boson candidate

### 5.2.1 Muon information

The two muons associated with the  $Z$  boson are added to the  $\xi$  reconstruction using Eq. 5.1. There can be additional low  $p_T$  muons in the event from  $b$ -quark decay or signals in the muon system from high energy jets that go through the calorimeter outer layers. Additional muon signals can come from other sources such as fake muon detector hits, muons from beam losses or cosmic rays. Muon signals that are not associated with the  $Z$  boson are required to be at least loose quality and have a matched track in the central tracker in order to be added to the  $\xi$  reconstruction. About 2.6% of the events have muons that pass these criteria. The transverse momentum of these muons is shown in Fig. 5.3.

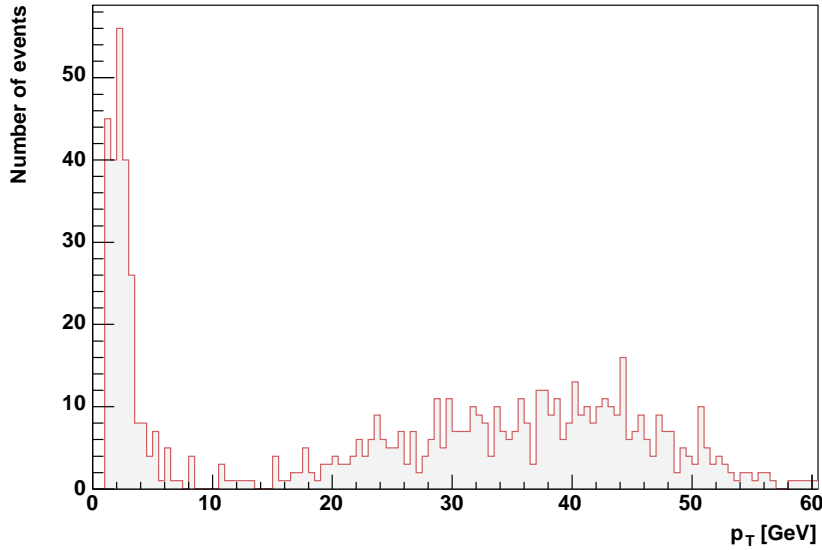


Figure 5.3: Transverse momentum of muons not associated with the  $Z$  boson decay that are at least loose quality with a matched track in the central tracking detector



## 5.2.2 Calorimeter information

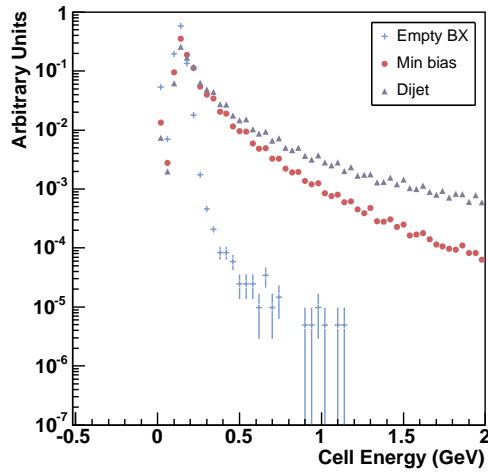
The response of the calorimeter layers is not uniform, due to the different types of cell construction (Section 3.2.3). Figure 5.4 shows the cell energies in two regions of the calorimeter for three types of event: empty bunch crossing, minimum bias and dijet events. The empty bunch crossing (empty BX) data are taken with the zero bias trigger, and interactions are excluded by requiring that no LM And/Or term is on (*N*, *S*, *FastZ*, *PHalo* or *AHalo*) and events have no vertices or jets. ‘Min bias’ events are collected with the minimum bias trigger which requires that the *FastZ* term is on. The dijet events are required to have at least two jets with  $p_T > 15$  GeV that pass the jet identification criteria [57].

The figure shows the cell energies in the EM1 and CH1 layers in the South central region,  $-2.6 < \eta < 0$ . In the CH1 layer the empty BX distribution is very similar to the physics samples, which indicates that the cells are firing randomly. The ICD and MG layers have similar distributions, and in addition the calorimeter is not calibrated in these layers. Only the eight layers of the EM and FH are therefore used in this analysis.

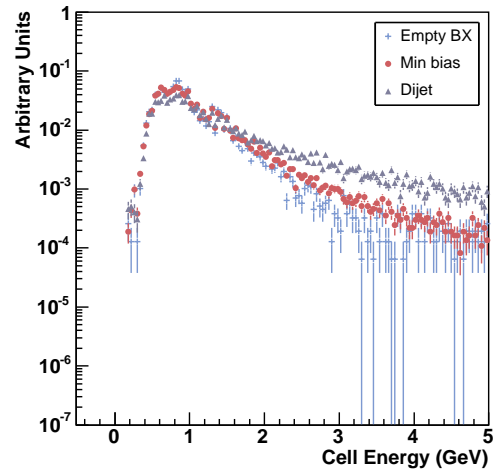
The calorimeter is currently being calibrated in order to correct each cell signal during data processing. For this analysis the best available calibration constants are applied.

### Hot cell killing

A ‘hot cell killing’ algorithm was developed for this analysis to remove noisy calorimeter cells. This is necessary because a rapidity gap requirement is made (Section 5.4) for diffractive candidates: a hot cell in the gap region of a diffractive



(a) EM1



(b) CH1

Figure 5.4: Cell energies in the range  $-2.6 < \eta < 0$  in the layers (a) EM1 and (b) CH1 for empty bunch crossing, minimum bias and dijet events. The distributions are normalised to unity.

interaction would lead to rejection of the event.

The algorithm uses events taken with the zero bias trigger and analyses every *ieta* strip in every EM and FH layer, in every run that has at least 500 zero bias events. The mean energy  $\bar{E}$  and standard deviation  $\sigma_E$  are calculated for all cells in the strip, including those with no signal. A threshold is set at  $\bar{E} + n \sigma_E$  and cells are excluded if their average energy over the run is above the threshold.

Using a threshold of  $4\sigma$  removes an average of about 280 cells per run, and a  $3\sigma$  threshold removes about 570 cells. The more restrictive  $3\sigma$  threshold is used. The improvement in data quality can be seen by comparing the cell energy distributions in empty BX events before and after hot cell killing (Figs 5.5 and 5.6). Hot cell killing is performed in 75% of the  $Z \rightarrow \mu^+\mu^-$  runs due to statistical limitations in the zero bias dataset.

### Calorimeter noise

An energy threshold is applied to the calorimeter cells to reduce low-level noise. In the empty bunch crossing sample, around 98% of the cell energies are lower than about 150-350 MeV in the EM region (depending on the layer) and 400-550 MeV in the FH region. The cell energy threshold for the analysis is set at a level such that the average observed momentum loss  $\xi_{obs}$  in empty BX events is  $\xi_{obs} \approx 0$ . Using an energy threshold of  $E = 300$  MeV, about 75% of empty BX events have  $\xi < 1 \times 10^{-4}$ . With a threshold of  $E = 500$  MeV, 96% have  $\xi < 1 \times 10^{-4}$  and 98% have  $\xi < 1 \times 10^{-3}$ . The latter threshold is used. Figure 5.7 shows the energy of cells in all  $Z \rightarrow \mu^+\mu^-$  events before the threshold is applied.

Coherent noise, such as the ‘Ring-of-Fire’ problem that causes all cells with the

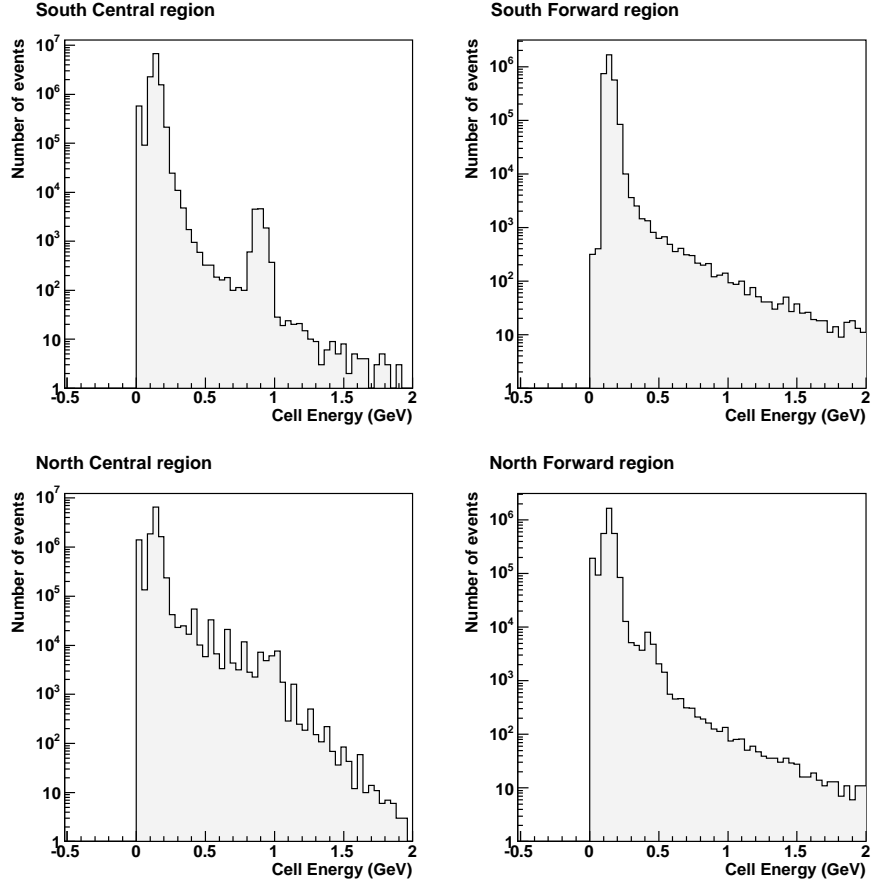


Figure 5.5: Cell energy in the EM1 layer for empty BX events before hot cell killing is performed. The layers are divided into four regions, with boundaries at  $\eta = 0$  (North-South) and  $|\eta| = 3.2$  (Central-Forward)

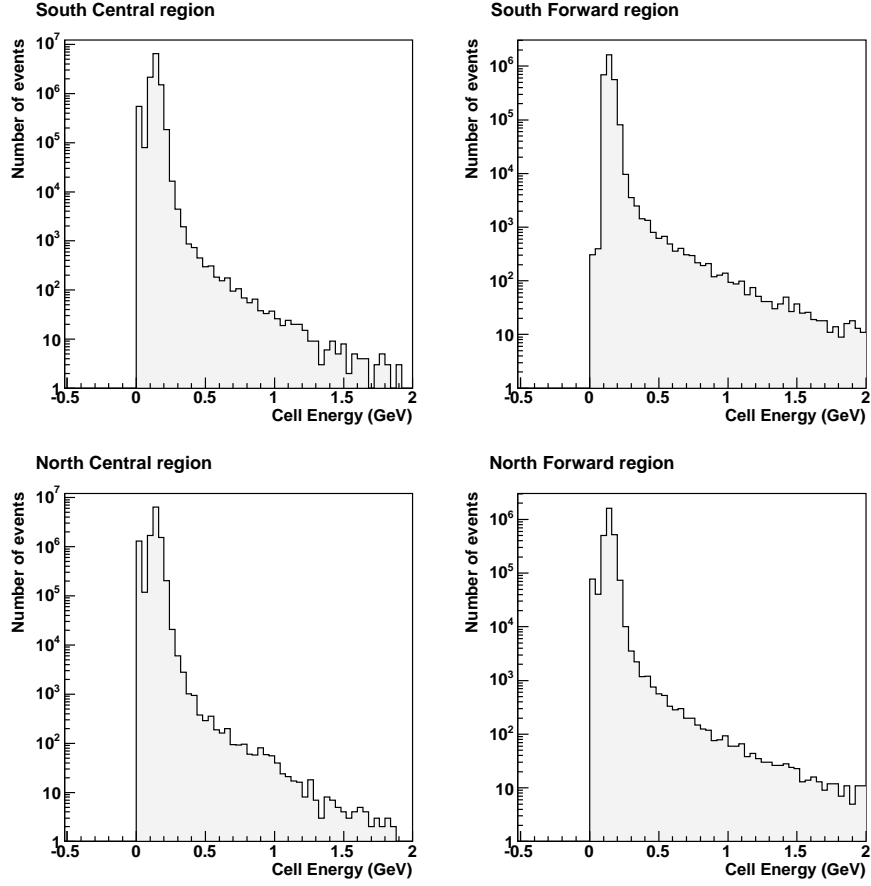


Figure 5.6: Cell energy in the EM1 layer for empty BX events after hot cell killing is performed. The layers are divided into four regions, with boundaries at  $\eta = 0$  (North-South) and  $|\eta| = 3.2$  (Central-Forward)

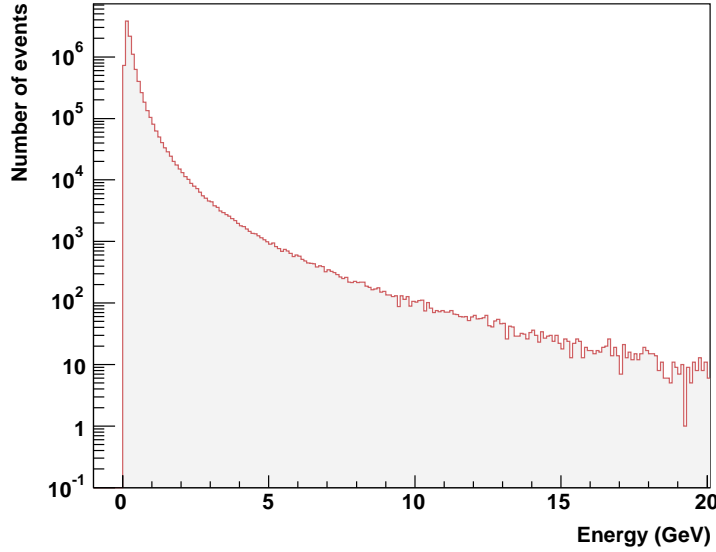


Figure 5.7: Energy of cells in all  $Z \rightarrow \mu^+\mu^-$  events, before the threshold is applied

same *ieta* to output a large noise signal at the same time, cannot be found with a hot cell algorithm. All known sources of coherent noise are removed by excluding the luminosity blocks categorised as bad by the Jet/Missing  $E_T$  group.

The observed momentum loss  $\xi_{obs}$  in  $Z \rightarrow \mu^+\mu^-$  events is shown in Fig. 5.8, and the fraction of  $\xi_{obs}$  contributed by the muons is shown in Fig. 5.9.

### 5.3 POMWIG simulation of diffractive $Z \rightarrow \mu^+\mu^-$

The Monte Carlo samples used in this analysis are generated by POMWIG. The events are  $\bar{p} + p \rightarrow \bar{p} + (Z/\gamma)^* + X$ , in which the  $Z$  boson decays to muons, and the interactions proceed via reggeon or pomeron exchange. Events were generated in the kinematic range  $\xi < 0.3$  and  $M_{\mu\mu} > 30$  GeV. The default H1 ‘fit 2’ pomeron

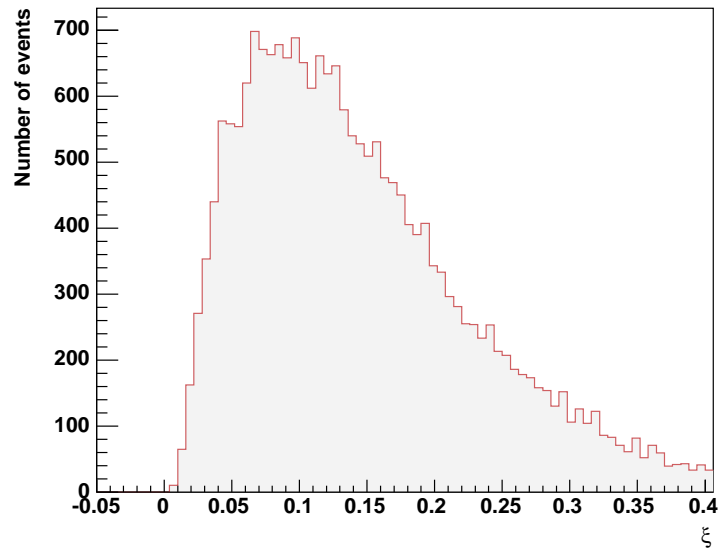


Figure 5.8: Observed momentum loss  $\xi_{obs}$  in all  $Z \rightarrow \mu^+\mu^-$  events

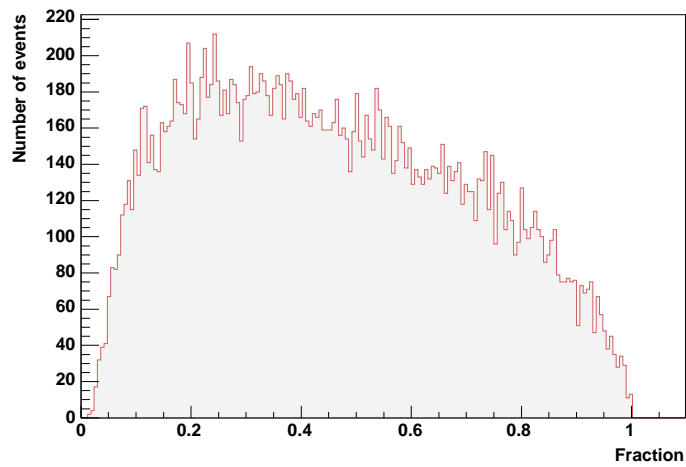


Figure 5.9: Fraction of the observed momentum loss contributed by the muons, in all  $Z \rightarrow \mu^+\mu^-$  events

structure function was used (Section 2.3).<sup>1</sup> The outgoing antiproton direction defines the  $z$  axis, and therefore corresponds to positive pseudorapidity.

It is found that a small fraction of the events have unexpected distributions of particle pseudorapidity: they have a few particles at high pseudorapidity (close to the outgoing antiproton), usually two to three pions with  $\eta \gtrsim 5$  and  $E \gtrsim 50$  GeV, and a large rapidity gap in the region  $2 \lesssim \eta \lesssim 5$ . The interactions are mostly reggeon exchange, and almost all have  $\xi \gtrsim 0.1$ . POMWIG does not model the scenario in which an interaction has a rapidity gap and the beam particle then dissociates into a soft system of very forward particles. These events are therefore high  $\xi$  events with large rapidity gaps in the dissociative system. Since the calorimeter coverage only extends to  $|\eta| < 5.2$ , these events will look like low  $\xi$  events when the acceptance cuts (Section 5.3.1) are made on the Monte Carlo sample, and therefore affect the acceptance corrections calculated from the Monte Carlo. It therefore has to be decided whether these generated events are ‘real physics’ or an artefact of the HERWIG hadronisation process.

The existence of these events is probably due to a limitation in the HERWIG hadronisation model (used by POMWIG), which leads to rapidity gaps between clusters of particles in the final state. It has already been noted [58] that HERWIG generates an excess number of rapidity gap events.

Events are rejected if they have particles with  $\eta > 5.2$ , which corresponds to the pseudorapidity limit of the calorimeter, and a rapidity gap in the range  $3.2 < |\eta| < 5.2$ , which is the region of the rapidity gap requirement made in the analysis of the data (Section 5.4). This requirement ensures that the sample is suitable for

---

<sup>1</sup> A sample was also generated with H1 ‘fit 3’ and used for a cross-check of the systematic uncertainties (Sections 5.6.3 and 5.6.4).



simulation of the data. It rejects 12.6% of the reggeon events and 1.9% of the pomeron events.

### 5.3.1 Acceptance cuts

The DØ detector simulation is not used because the Run II calorimeter response is very poorly modelled in the simulation available for this dataset [59]: there is insufficient material in front of the calorimeter; the short charge collection time of Run II is not simulated; and the calorimeter in Run II has higher levels of noise than in Run I, which is reflected in the lower energy thresholds used in Run I diffractive analyses [10]. Several acceptance cuts are applied to the simulated events in order to model the data. These exclude the following particles:

- Neutrinos
- Particles outside the calorimeter range ( $|\eta| > 5.2$ )
- Muons outside the muon detector range ( $|\eta| > 2.0$ )
- Particles with  $E < 1.0$  GeV

The Monte Carlo simulation does not include a corrected energy scale, resolution effects or the effects of backscattering (for example, particles scattering from detector components into the rapidity gap). However, there is good agreement between the simulated events and the data (Section 5.5). Events are selected in the appropriate kinematic region by requiring that the two highest  $p_T$  muons have  $|\eta| < 2.0$  and  $p_T > 15$  GeV, and that the dimuon invariant mass is  $M_{\mu\mu} > 40$  GeV.

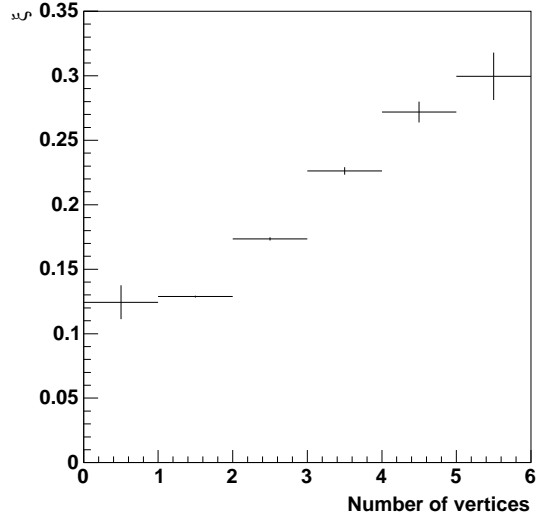
This sample is used for motivating the kinematic range of the measurement (Section 5.4) and for correcting the measurement of the momentum loss (Section 5.5).

## 5.4 Rapidity Gap Requirement

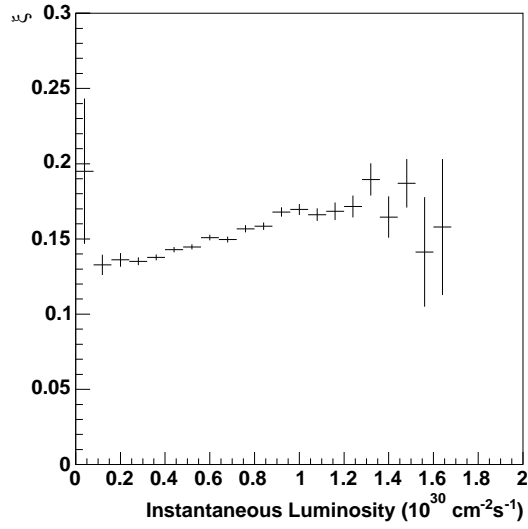
Diffraction candidate events are required to have a forward rapidity gap in the region  $3.2 < |\eta| < 5.2$  by requiring that the maximum pseudorapidity  $\eta_{max}$  of the calorimeter signals is  $\eta_{max}^p < 3.2$  in the proton direction or  $\eta_{max}^{\bar{p}} > -3.2$  in the antiproton direction. The rapidity gap requirement is made for two reasons: firstly, to restrict the sample kinematically to the low  $\xi$  region (where  $\xi$  is well reconstructed); and secondly, to reject events with multiple interactions, which occur when there is more than one  $p\bar{p}$  collision in the same bunch crossing. Multiple interactions lead to misreconstruction of the momentum loss because they contribute to the observed final state. This is seen in Fig. 5.10, which shows the average  $\xi$  increasing as a function of the number of vertices in the event and also with increasing instantaneous luminosity of the tick.

The number of vertices in the event is not used for excluding multiple interactions because the current vertex-finding algorithm at DØ is not sufficiently accurate at counting vertices. The algorithm is optimised for locating the vertex of the high  $p_T$  interaction and is prone to overcounting, especially at higher luminosities, by asserting that there are two or more at the same location. For Fig. 5.10(a), a requirement is made that additional vertices are at least 0.2 cm from the primary vertex.

The LM detectors are not used for confirming the rapidity gap, as they were in a



(a)



(b)

Figure 5.10: Average momentum loss  $\xi_{obs}$  versus (a) number of vertices and (b) instantaneous luminosity in all  $Z \rightarrow \mu^+ \mu^-$  events

previous version of the analysis [47], because they provide only a binary signal over a fixed pseudorapidity range.

### 5.4.1 Choice of event kinematics

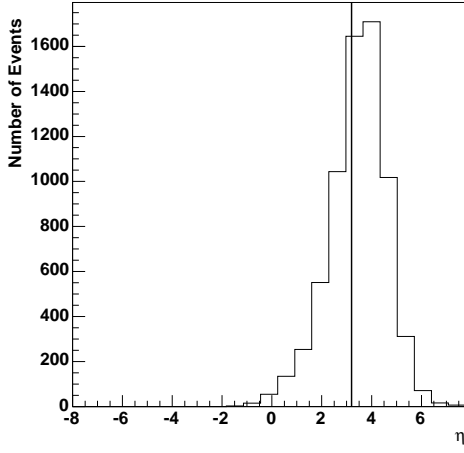
The rapidity gap edge at  $|\eta| = 3.2$  is about 1.25 units of pseudorapidity from the edge of the calorimeter (two units from the final two layers of the hadronic region: Fig. 3.7). This choice is made in order to identify that the rapidity gap is from a diffractive interaction [15, 60]. In non-diffractive interactions, statistical fluctuation of particle multiplicities can lead to small rapidity gaps, but the rate of these is exponentially suppressed by the size of the rapidity gap (Section 2.2.1).

Figures 5.11 and 5.12 show the size of the rapidity gap in POMWIG events increasing as the momentum loss decreases. In Fig. 5.11(a), the events have momentum loss  $\xi < 0.05$ . The distribution shows the maximum pseudorapidity  $\eta_{max}^{all}$  of all the particles in the event. The vertical line indicates the edge of the rapidity gap: events with  $\eta_{max}^{all}$  to the right of the line fail the gap cut. Figures 5.11(b), 5.12(a) and 5.12(b) show the effect of lowering the momentum loss threshold to  $\xi < (0.03, 0.02, 0.01)$ , in that the distributions move towards lower values of  $\eta_{max}^{all}$  and a higher fraction of events pass the gap cut.

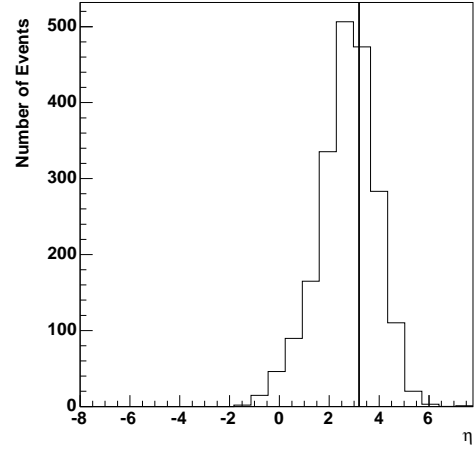
The kinematic range for the measurement is chosen to be  $\xi < 0.02$ , so that about 85% of the events pass the rapidity gap cut at  $|\eta| = 3.2$  (Section 5.6.3).

After the rapidity gap cut is made in the detector, the numbers of  $Z \rightarrow \mu^+ \mu^-$  events with a gap in the proton direction,  $N_{gap}^p$ , and in the antiproton direction,  $N_{gap}^{\bar{p}}$ , are:

$$N_{gap}^p = 156 \pm 12 \text{ (stat.)}$$

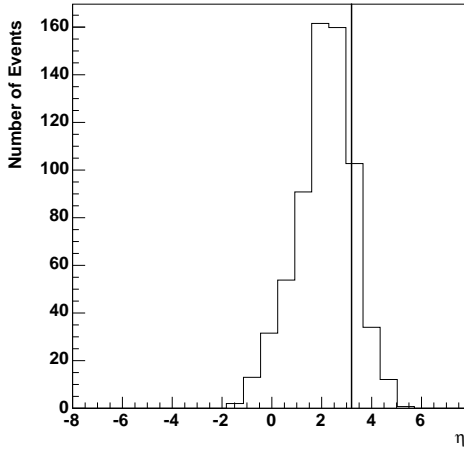


(a)  $\xi < 0.05$

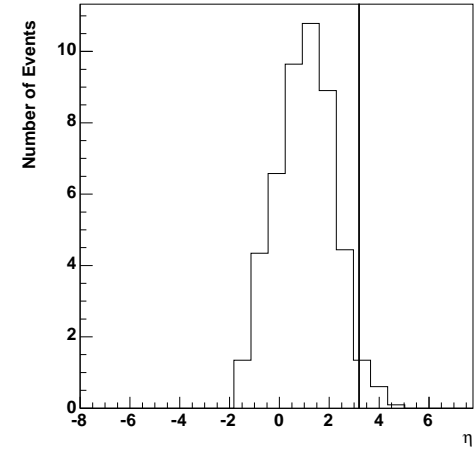


(b)  $\xi < 0.03$

Figure 5.11: Pseudorapidity of most forward particle in POMWIG  $Z \rightarrow \mu^+\mu^-$  events with (a)  $\xi < 0.05$  and (b)  $\xi < 0.03$



(a)  $\xi < 0.02$



(b)  $\xi < 0.01$

Figure 5.12: Pseudorapidity of most forward particle in POMWIG  $Z \rightarrow \mu^+\mu^-$  events with (a)  $\xi < 0.02$  and (b)  $\xi < 0.01$

$$N_{gap}^{\bar{p}} = 139 \pm 12 \text{ (stat.)} .$$

No cut on  $\xi$  is made. Thirteen of the events have a rapidity gap in both directions, giving a total of 282 candidate events, which is 2.6% of the sample.

## 5.5 Momentum Loss Correction

The observed momentum loss is corrected for the detector acceptance using POMWIG events. Figure 5.13 shows the observed momentum loss  $\xi_{obs}$  in  $Z \rightarrow \mu^+\mu^-$  events that pass the rapidity gap cut. Overlaid on the figure is the POMWIG prediction for the distribution, normalised to the data. The prediction is made by calculating the ‘reconstructed’ momentum loss  $\xi_{reco}$  from the particles that pass the acceptance cuts (Section 5.3.1). The events in the Monte Carlo (MC) distribution have passed the rapidity gap cut, made by requiring that the most forward particle that passes the acceptance cuts has  $\eta_{max} < 3.2$ . The POMWIG distribution is in good agreement with the data.

Figure 5.14 shows  $\eta_{max}$  for the most forward calorimeter signal in  $Z \rightarrow \mu^+\mu^-$  candidate events that have  $\xi_{obs} < 0.02$ . The distribution for events with an antiproton-side gap has the  $x$ -axis reversed, and is added to the distribution for events with a proton-side gap in order to increase the size of the sample. Overlaid on the figure is the POMWIG prediction for the distribution, which is  $\eta_{max}$  of the particles that pass acceptance cuts in events with  $\xi_{reco} < 0.02$ . This also shows good agreement with the data. The fraction of events with  $\eta_{max} < 3.2$  is lower than in Fig. 5.12(a), which shows  $\eta_{max}$  for events with  $\xi < 0.02$ , because it includes a higher reggeon component. This arises because there are events with high  $\xi$  that

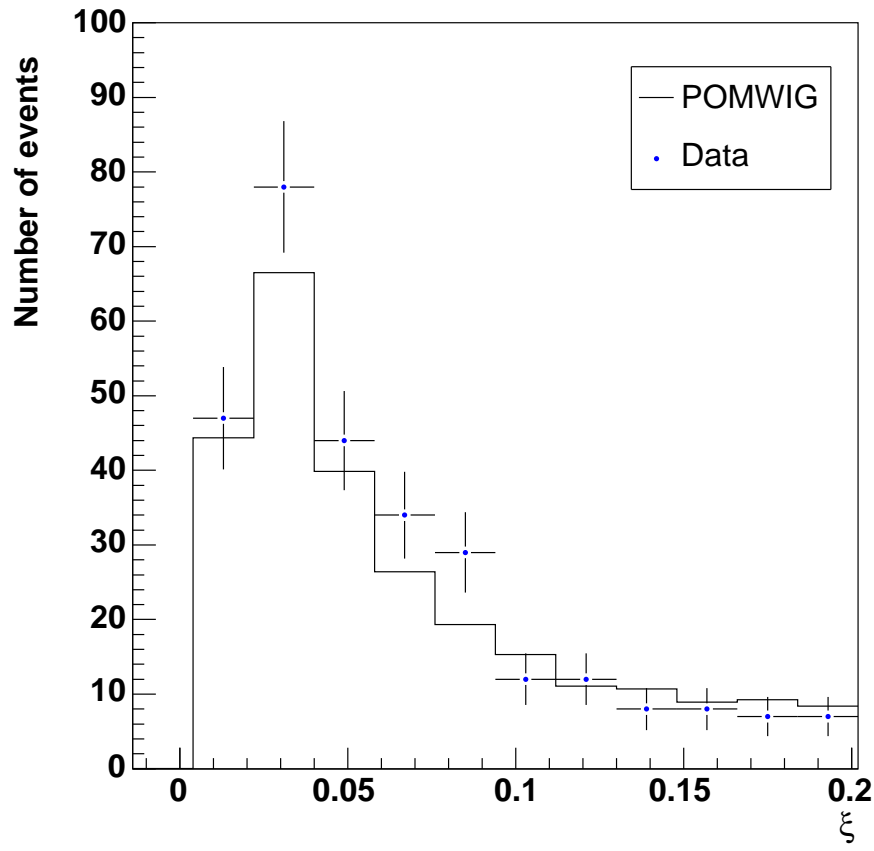


Figure 5.13: Observed momentum loss  $\xi_{obs}$  in  $Z \rightarrow \mu^+\mu^-$  events with a rapidity gap. The POMWIG prediction is shown, scaled to the data distribution.

are mis-reconstructed and have a low  $\xi_{obs}$ . These are removed by the rapidity gap requirement.

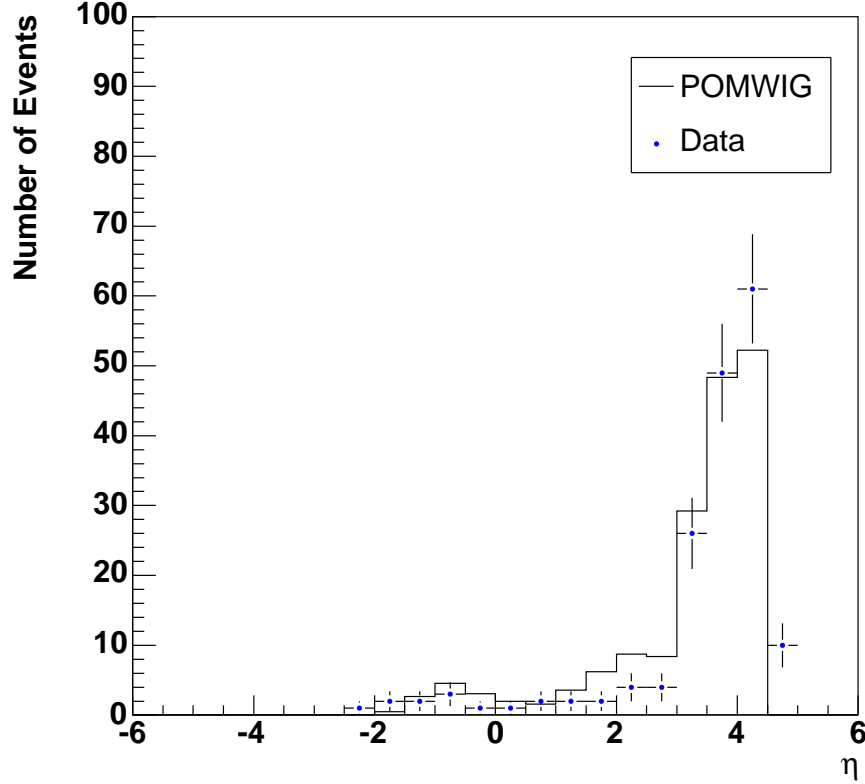


Figure 5.14: Pseudorapidity of most forward cell in  $Z \rightarrow \mu^+\mu^-$  events with momentum loss  $\xi_{obs} < 0.02$ , where the antiproton-side distribution is reversed and added to the proton distribution. The POMWIG prediction is also shown, scaled to the data distribution, which includes a requirement that particles are within  $|\eta| < 4.45$ .

The particle energy threshold in the acceptance cuts,  $E = 1$  GeV, is chosen such that there is the minimum deviation of the  $\xi_{reco}$  distribution in MC from the  $\xi_{obs}$  distribution in data over the range  $0 < \xi_{reco} < 0.2$  (Fig. 5.13).



The correction to the measurement of  $\xi_{obs}$  in the data is calculated using  $\xi_{reco}$  in the Monte Carlo. Figure 5.15 shows  $\xi_{reco}$  as a fraction of the true beam  $\xi$ , in bins of  $\xi_{reco}$ , for POMWIG events with a rapidity gap. This figure provides a series of correction factors for the data, the inverse of the y-axis value, which are applied to each event according to the value of  $\xi_{obs}$ . The corrections are applied after the rapidity gap selection is made, because POMWIG predictions become more uncertain at high  $\xi$  due to the poor understanding of reggeon exchange (Section 2.3).

The largest correction factor, which is applied to events with very low  $\xi_{obs}$ , is about 1.25. In the analysis of diffractive  $W$  boson production at DØ in Run I [10], a single correction factor  $1.5 \pm 0.3$  is applied to the momentum loss in all events. The factor is derived using a sample of POMPYT  $W$  boson events with the full detector simulation applied, and it corrects for energy in the FH region which is not included in the reconstruction of  $\xi$ . The correction factors are not expected to be large because the contribution to  $\xi$  from particles travelling in the opposite direction to the intact proton is small (Eq. 5.1). However, the correction does assume that the events are diffractive, with no final state particles close to the intact proton. If there are non-diffractive events that pass the rapidity gap requirement – for example, if all the calorimeter signals in the gap region are below the energy threshold – then the applied correction factors in these events are too small, and there may remain some high  $\xi$  events in the diffractive candidate ( $\xi < 0.02$ ) sample. The contribution due to non-diffractive events is estimated in Section 5.7.2.

The momentum loss  $\xi$  in events with a rapidity gap, with correction factors applied, is shown in Fig. 5.16. The average  $\xi$  is shown as a function of number of vertices and instantaneous luminosity in Fig. 5.17, demonstrating that there is no longer a contribution from multiple interactions. About 1% of the rapidity gap

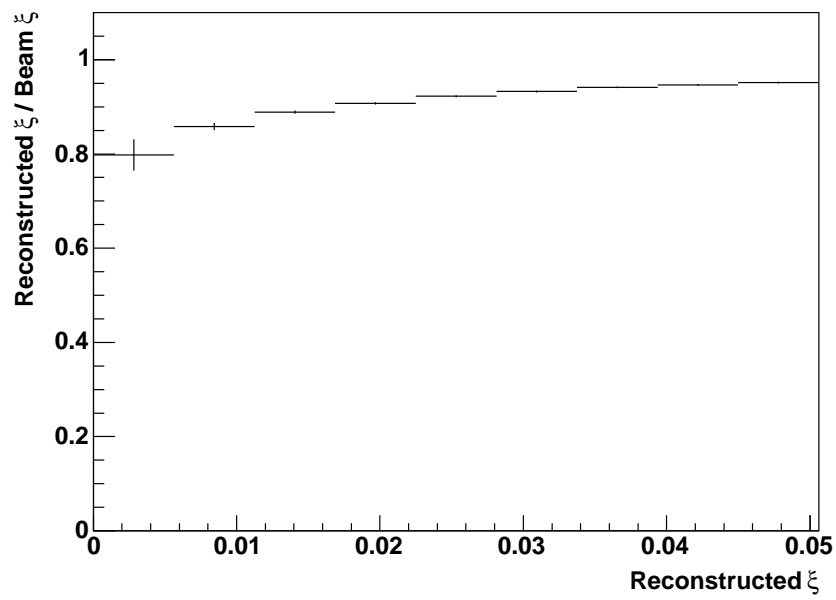


Figure 5.15: POMWIG prediction for the fraction of true beam  $\xi$  which is reconstructed in the detector,  $\xi_{reco}/\xi$ , as a function of  $\xi_{reco}$

candidates have two vertices: this is not a concern because the fraction of the sample is smaller than the systematic uncertainties (Section 5.6.2).

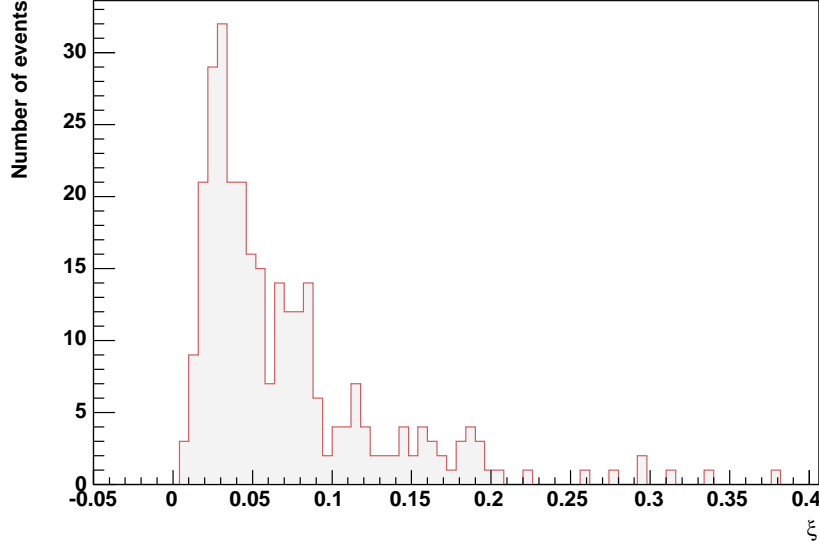


Figure 5.16: Momentum loss in  $Z \rightarrow \mu^+\mu^-$  events with a rapidity gap

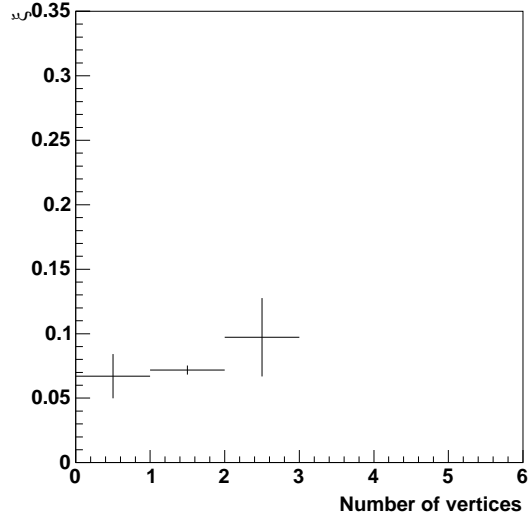
After the momentum loss threshold is applied, the numbers of diffractive  $Z \rightarrow \mu^+\mu^-$  candidate events with  $\xi_p < 0.02$  in the proton direction,  $N_{cand}^p$ , and  $\xi_{\bar{p}}$  in the antiproton direction,  $N_{cand}^{\bar{p}}$ , are:

$$N_{cand}^p = 10 \pm 3 \text{ (stat.)}$$

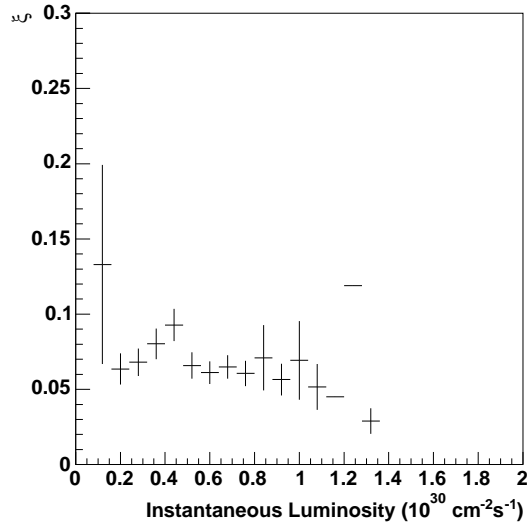
$$N_{cand}^{\bar{p}} = 14 \pm 4 \text{ (stat.)} .$$

There are no events with  $\xi_p < 0.02$  and  $\xi_{\bar{p}} < 0.02$ , so the total number of diffractive candidate events is 24, which is 8.5% of the rapidity gap sample and 0.2% of the inclusive sample.

Figure 5.18 shows one of the diffractive candidate events. The upper figure shows the calorimeter signals, opened out to show  $\eta$  versus  $\phi$  with the muon signals



(a)



(b)

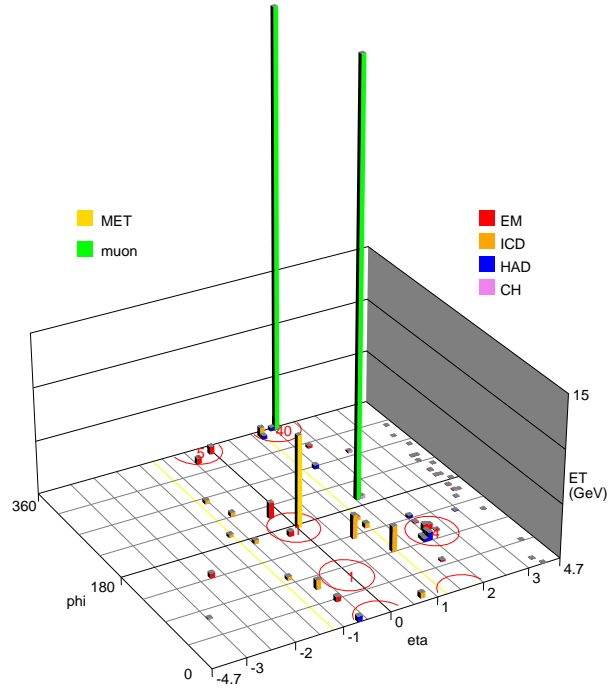
Figure 5.17: Average momentum loss versus (a) number of vertices and (b) instantaneous luminosity in  $Z \rightarrow \mu^+ \mu^-$  events with a rapidity gap

superimposed. Proton dissociation can be seen at the high pseudorapidity edge of the detector, and there is no dissociation on the opposite side. The lower figure shows the side view of the tracking and calorimeter detectors, and the asymmetric distribution along the collision axis of the particles in the events. The momentum loss in this event is  $\xi_{\overline{p}} = 0.017$ .

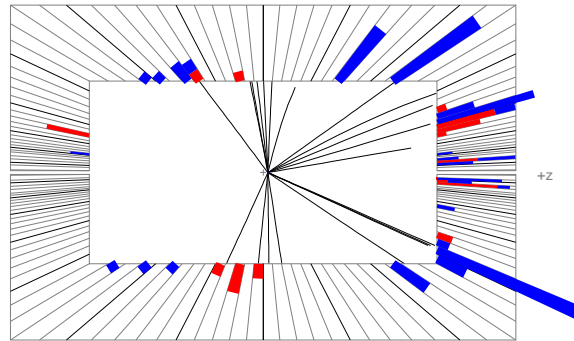
Figure 5.19 shows the fraction of  $\xi_{obs}$  contributed by the muons in the diffractive candidate events, which may be compared with Fig. 5.9 for all  $Z \rightarrow \mu^+\mu^-$  events. In the diffractive sample, the muon contribution dominates  $\xi_{obs}$ . This indicates that the success of POMWIG in modelling the data despite the absence of detector simulation is due to the relatively low contribution to  $\xi_{obs}$  from the calorimeter, although this has not been studied in detail.

Figures 5.20(a) and 5.20(b) show the pseudorapidity and invariant mass of the two highest  $p_T$  muons in diffractive candidate events, and Figs. 5.21(a) and 5.21(b) show the rapidity and  $p_T$  of the diffractive  $Z$  boson candidates. Overlaid are the POMWIG predictions for these distributions, normalised to the data. The POMWIG events have been passed through the fast detector parameterisation PMCS [61], which smears the muon momenta to match the resolution measured in the data. The POMWIG distributions in Figs. 5.20 and 5.21 are corrected for the muon detector acceptance and muon identification efficiencies, as described in Section 5.6.4.

The Drell-Yan ( $\gamma^* \rightarrow \mu^+\mu^-$ ) component of the dimuon invariant mass distribution is larger in the POMWIG events, and perhaps in the diffractive data, than in the inclusive  $Z \rightarrow \mu^+\mu^-$  data. This effect can be explained because there is a kinematic bias in the diffractive events towards low mass final states ( $M_X = \sqrt{\xi s}$ ).



(a)  $\eta$ - $\phi$  view



(b) Side view

Figure 5.18: Diffractive candidate event, showing the (a) calorimeter in  $\eta$ - $\phi$  view, with muons superimposed, and the (b) calorimeter and central tracking in side view, where the outgoing proton direction is towards the right of the figure

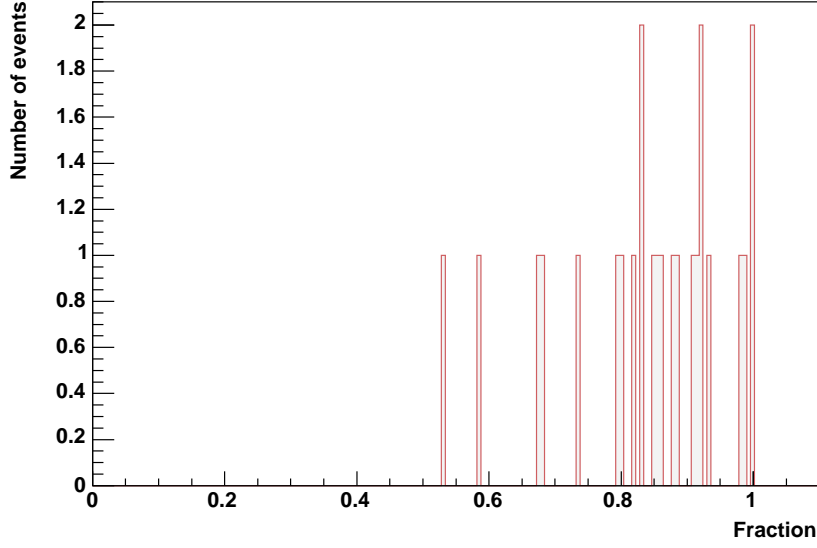


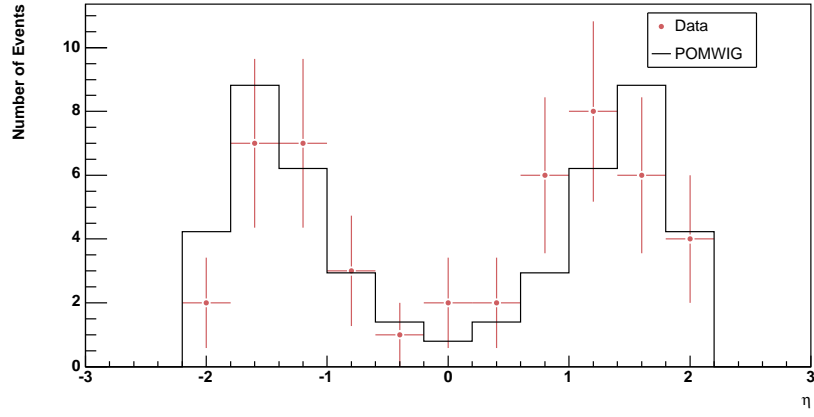
Figure 5.19: Fraction of the momentum loss  $\xi_{obs}$  contributed by the muons, in diffractive  $Z \rightarrow \mu^+ \mu^-$  candidate events

## 5.6 Components of the Cross Section

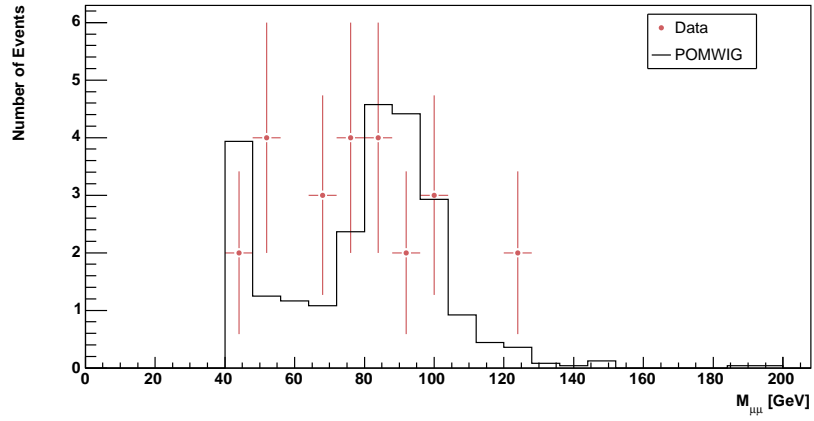
The cross section times branching ratio,  $\sigma \times \text{Br}$ , is calculated from the number of candidates,  $N_{\text{cand}}$ , and the integrated luminosity,  $\int \mathcal{L} dt$ , using the equation

$$\sigma \times \text{Br} ((Z/\gamma)^* \rightarrow \mu^+ \mu^-, \xi < 0.02) = \frac{N}{\int \mathcal{L} dt} \cdot \frac{(1 - f_{\text{bb}} - f_{\text{cos}}) (1 - f_{\tau\tau}) (1 - f_W)}{\varepsilon_{\text{gap}} \varepsilon_{\text{MC}} \varepsilon_{\text{opp-q}} \varepsilon_{\text{isol}} \varepsilon_{\text{cosmic}}}, \quad (5.2)$$

where  $f$  denotes a correction factor for a background contamination fraction and  $\varepsilon$  denotes an efficiency. Each component is described in the following sections.



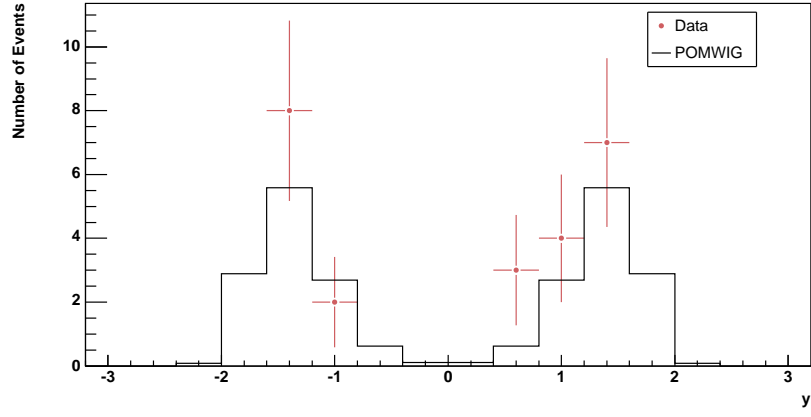
(a)



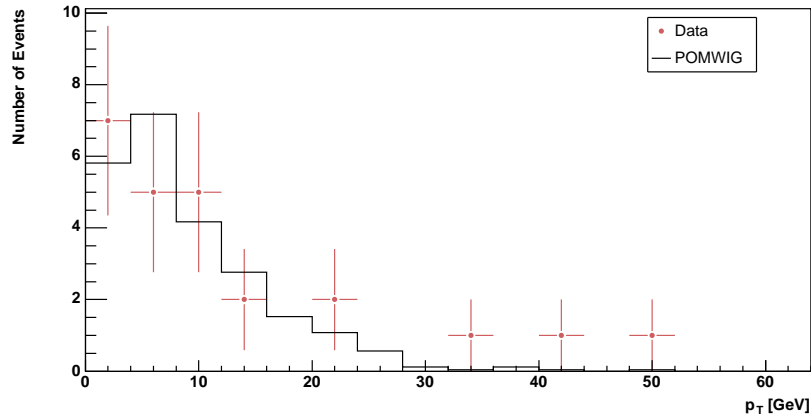
(b)

Figure 5.20: Diffractive  $Z \rightarrow \mu^+ \mu^-$  candidate events, showing the (a) pseudorapidity of each muon and (b) invariant mass of the Z boson candidate. The POMWIG prediction is shown, scaled to the data distribution.





(a)



(b)

Figure 5.21: Diffractive  $Z \rightarrow \mu^+\mu^-$  candidate events, showing the (a) rapidity and (b) transverse momentum of the  $Z$  boson candidate. The POMWIG prediction is shown, scaled to the data distribution.

### 5.6.1 Number of candidates

This section describes the correction to the number of candidates for multiple interactions; the systematic uncertainty in the number of candidates is studied in Section 5.6.2.

Diffraction events that have additional  $p\bar{p}$  interactions in the same bunch crossing are excluded by the rapidity gap cut, and the number of candidates must be corrected for this loss. In each tick, the average fraction of interactions not accompanied by any other interactions,  $F(s.i.)$ , can be calculated from the average number of interactions per bunch crossing  $\mu$ :

$$F(s.i.) = \frac{P(1)}{1 - P(0)} = \frac{\mu e^{-\mu}}{1 - e^{-\mu}}$$

where  $\mu$  is calculated from the instantaneous luminosity (Section 4.2). The average number of interactions that are within the acceptance of the DØ detector and can therefore be vetoed by the gap requirement,  $\mu_{LM}$ , is calculated for each event from the instantaneous luminosity of the tick,  $\mathcal{L}$ , using:

$$\mu_{LM} = A_{LM} \frac{\sigma_{p\bar{p}} \mathcal{L}}{f}$$

where  $A_{LM}$  is the acceptance of the Luminosity Monitor,  $A_{LM} = 0.833 \pm 0.037$ ,  $\sigma_{p\bar{p}}$  is the total inelastic  $p\bar{p}$  cross section,  $\sigma_{p\bar{p}} = (60.7 \pm 2.4)$  mb, and  $f$  is the rotation frequency of the tick,  $f = 47.7$  kHz. The uncertainty in the instantaneous luminosity is 6.5%.

The number of  $Z \rightarrow \mu^+\mu^-$  events in single interaction bunch crossings,  $N_Z^{s.i.}$ , is estimated with

$$N_Z^{s.i.} = \sum_n F(s.i.)_n$$

where the sum is over all  $Z \rightarrow \mu^+\mu^-$  events (before diffractive selection cuts). The ratio of all  $Z \rightarrow \mu^+\mu^-$  events to the number in single interaction bunch crossings is used to correct the number of diffractive candidates, with:

$$N_{corr} = N_{cand} \times \frac{N_Z}{N_Z^{s.i.}}$$

where  $N_{cand}$  is the number of diffractive candidates in single interaction bunch crossings, and  $N_{corr}$  is the number of diffractive candidates in all bunch crossings.

The number of diffractive candidates is  $N_{cand} = 24$ , and the ratio is  $N_Z/N_Z^{s.i.} = 1.40 \pm 0.04$ , so the corrected number of candidates is

$$N_{corr} = 33.7 \pm 6.9 \text{ (stat.)} \pm 1.1 \text{ (sys.)}$$

where the systematic uncertainty is calculated by propagating the luminosity-related uncertainties to the correction ratio. The statistical uncertainty dominates.

## 5.6.2 Systematic investigations

Systematic uncertainties are investigated by varying the parameters of the analysis and comparing the corrected number of candidates for each variation. Systematic uncertainties are quoted throughout.

### Uncertainty due to North-South asymmetry

The number of events in the proton-side rapidity gap sample is larger than in the antiproton-side sample, and the antiproton-side diffractive sample is larger than the proton-side diffractive sample. As the differences are within the statistical uncertainties, and in the opposite direction for the rapidity gap and diffractive

samples (Section 5.4), it is assumed that there is no contribution to the systematic uncertainty from North-South asymmetry in the calorimeter, whether from detector noise or beam halo showering as discussed in Section 4.3.4.

### Uncertainty due to rapidity gap boundary

The effect of the hot cell killing on the rapidity gap candidate selection is estimated by performing the analysis only in the set of runs in which hot cell killing is available (Section 5.2.2). The number of rapidity gap candidates when using the  $3\sigma$  energy threshold, and when performing no hot cell killing, are shown in Table 5.1. As expected, the number of gap candidates is reduced when there is no hot cell killing. However, there is no difference in the number of diffractive candidates between the two analyses: the number of candidates is  $N_{corr} = 29.4 \pm 6.4$ . The uncertainty due to the hot cell killing is negligible in a sample of this size.

Threshold	$N_{gap}^p$	$N_{gap}^{\bar{p}}$
$3\sigma$	$120 \pm 11$	$113 \pm 11$
None	$116 \pm 11$	$112 \pm 11$

Table 5.1: Effect of hot cell killing on the number of rapidity gap candidates, in runs where hot cell killing is available

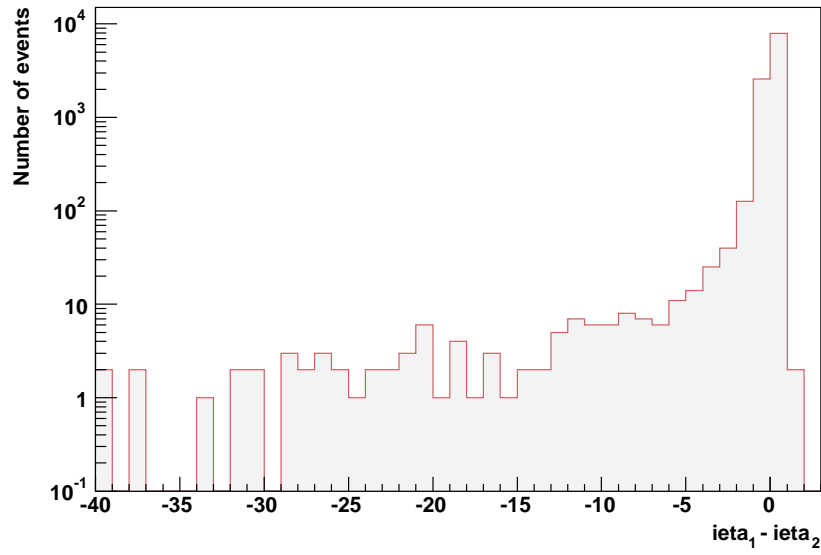
The rapidity gap boundary is tested by examining the second most forward calorimeter signal in the event, for which the pseudorapidity is referred to as  $\eta_{max}^{2nd}$ . If the two most forward cells in a gap event are far apart in pseudorapidity, it may be that the most forward signal is a hot cell in the gap region. The analysis is repeated using  $\eta_{max}^{2nd}$  to define the rapidity gap boundary, which results in a much

larger number of candidates:  $N_{corr} = 65.9 \pm 9.6$ , an increase of 96%.

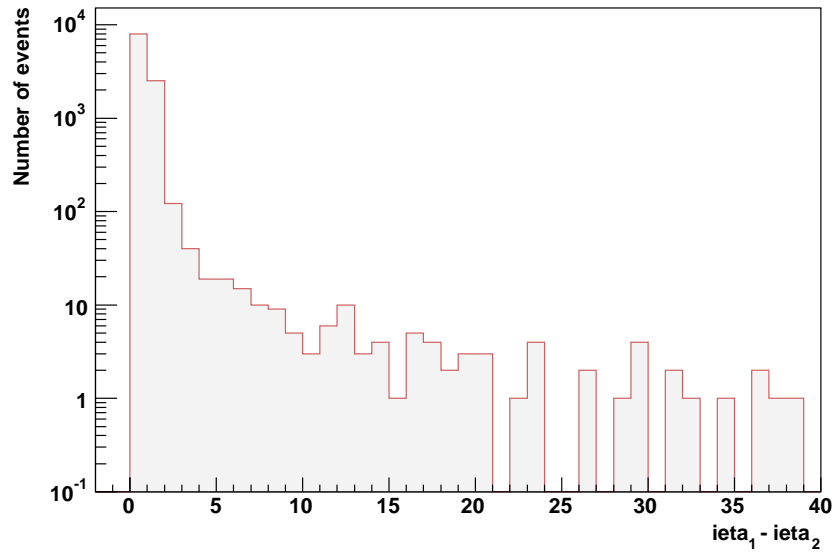
Figures 5.22 and 5.23 show the difference in  $ieta$  between the two cells at  $\eta_{max}$  and  $\eta_{max}^{2nd}$ , in all  $Z \rightarrow \mu^+\mu^-$  events and those with a gap respectively. This indicates whether or not the cells are neighbours; a distribution of  $\eta_{max} - \eta_{max}^{2nd}$ , which are measured using the physics pseudorapidity (Section 3.2), would be misleading because of the varying widths of the cells in the forward region. The inclusive sample is shown with a logarithmic y-axis and the gap sample is not. The two most forward cells are nearest neighbours in  $ieta$  in 97% of the  $Z \rightarrow \mu^+\mu^-$  events. In the rapidity gap events, the fraction is much lower, at 40%. For the other events there are several possibilities: the most forward cell may be noise that was not found by the hot cell algorithm; it may be energy from an additional soft interaction in the event, or it may be energy from the same interaction where no cells pass the energy threshold in the intermediate region.

The characteristics of the rapidity gap candidates are different when selected using  $\eta_{max}$  or  $\eta_{max}^{2nd}$  in the event. When using  $\eta_{max}$ , the LM detector term is off for the gap side in 38% of the proton-side gap candidate events and 35% of antiproton-side gap candidates. The fraction is expected to be low because the rapidity gap does not cover all of the LM range ( $2.7 < |\eta| < 4.4$ ), and the LM detectors can also be hit by muons from halo, or particles with energy below the cell energy threshold. Using the second cell method, the percentage of gap candidates in which the LM detector term is off is lower: 31% of proton-side gap events and 24% of antiproton-side gap events. This may indicate that in several of the additional events selected with  $\eta_{max}^{2nd}$ , the most forward object is not detector noise but a particle which passes through the LM detector into the calorimeter.

Another measure of the rapidity gap candidate characteristics is the number of

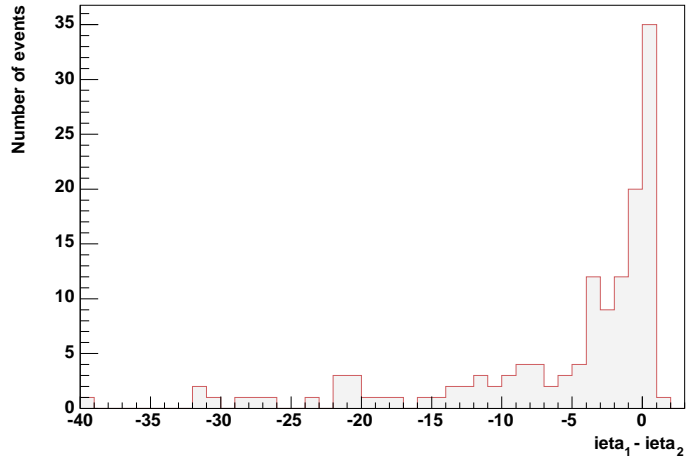


(a) antiproton

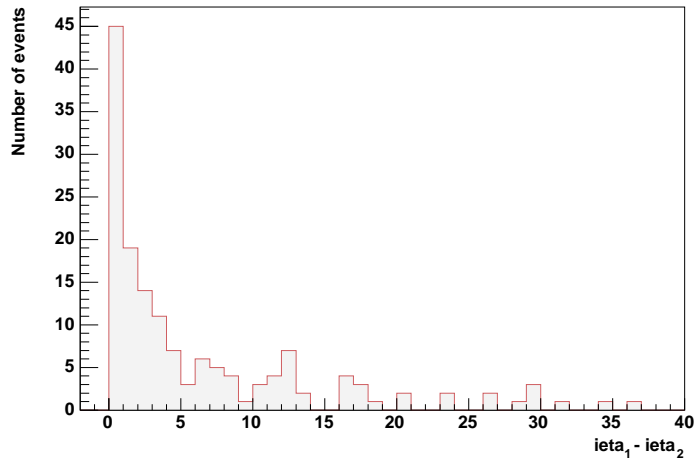


(b) proton

Figure 5.22: Difference in  $i\eta$  between the two most forward cells in all  $Z \rightarrow \mu^+\mu^-$  events



(a) antiproton



(b) proton

Figure 5.23: Difference in  $\eta$  between the two most forward cells in  $Z \rightarrow \mu^+\mu^-$  events with a rapidity gap

vertices in the event. The fraction of gap candidates with no vertices is higher in those selected using  $\eta_{max}$  (5%) than in those selected with  $\eta_{max}^{2nd}$  (3%), and in addition the fraction of gap candidates with two vertices is higher in the  $\eta_{max}^{2nd}$  sample (4%) than in the  $\eta_{max}$  sample (1%). This may indicate that using  $\eta_{max}^{2nd}$  for the rapidity gap increases the contamination from multiple interaction events. Figures 5.24(a) and 5.24(b) show the average  $\xi$  in events with a rapidity gap using  $\eta_{max}^{2nd}$ , as a function of the number of vertices and the instantaneous luminosity; there appear to be more events with multiple interactions when compared with the  $\eta_{max}$  sample in Fig. 5.17.

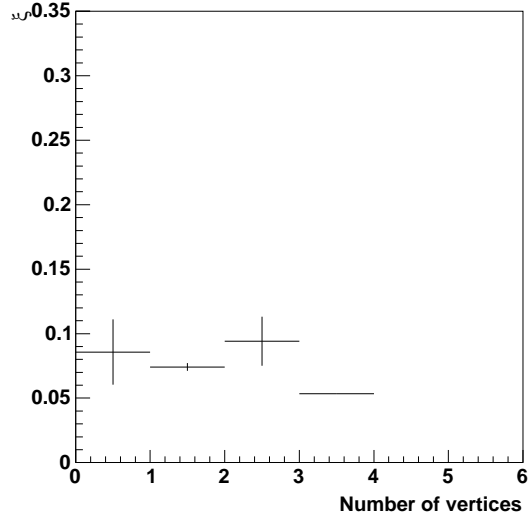
These comparisons begin to probe the characteristics of the most forward calorimeter cell in the events. However, as there is no clear separation in the additional gap candidates between gap events and background, it is concluded that this study is outside the scope of this analysis.

### **Uncertainty due to measurement of $\xi$**

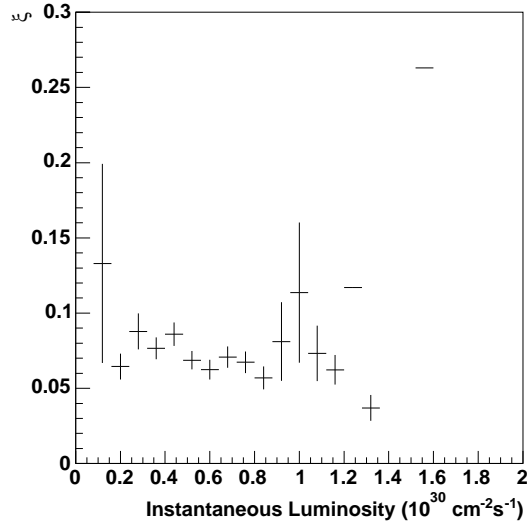
The uncertainty in measuring  $\xi$  propagates to uncertainty in the number of candidates because events may migrate above or below the threshold at  $\xi < 0.02$ . The two sources of uncertainty are the measurement of  $\xi_{obs}$  and the correction to the measurement.

The dominant uncertainty in reconstructing  $\xi_{obs}$  is in the calibration of the calorimeter. There are no uncertainties available for the calibration constants in this dataset, but an estimation can be made by performing the analysis with no calibration [59]. The number of candidates obtained with this method is  $N_{corr} = 25.3 \pm 6.0$ , which is 25% lower than the calibrated result.





(a)



(b)

Figure 5.24: Average momentum loss versus (a) number of vertices and (b) instantaneous luminosity in  $Z \rightarrow \mu^+ \mu^-$  events with a rapidity gap, in which the most forward cell is excluded from the analysis

$E_{data}$ (GeV)	$E_{MC}$ (GeV)	$N_{corr}$	Change (%)
0.5	0.8	$36.5 \pm 7.2$	+8
0.5	1.2	$30.9 \pm 6.6$	-8
0.6	1.2	$44.9 \pm 7.9$	+33
0.7	1.4	$61.7 \pm 9.3$	+83

Table 5.2: Effect of varying the data cell energy threshold,  $E_{data}$ , and the MC particle energy threshold,  $E_{MC}$ , on the number of candidates  $N_{corr}$ , with the percentage change shown in the final column.

The uncertainty due to the correction of  $\xi_{obs}$  is investigated by forming the analysis with various sets of correction factors. The first set uses the correction factors  $c_i$  (for every bin  $i$  in  $\xi$ ) increased by the uncertainty in the distribution in Fig. 5.15,  $\Delta c_i$ ; the second set has every correction factor decreased by the same amount. This assumes 100% correlation between the uncertainties in each bin. This yields little change in the results:  $N_{corr} = 33.7 \pm 6.9$  using  $c_i + \Delta c_i$ , and  $N_{corr} = 35.1 \pm 7.0$  using  $c_i - \Delta c_i$ .

The uncertainty in the correction factors is tested further by varying the particle energy threshold in the Monte Carlo with respect to the cell energy threshold in the data, and by increasing both thresholds by the same fraction. The results are in Table 5.2. There is an 83% increase in the number of candidates when using a data threshold  $E_{data} = 0.7$  GeV and a MC threshold  $E_{MC} = 1.4$  GeV: this may be due to raising the cell energy threshold by too much, although in principle the increase in MC energy threshold should correct for this. This is another area which requires further study.

The geometric acceptance cut in POMWIG events,  $\eta_{accept}$ , is decreased as a further check of the stability of the measurement. Two sets of correction factors are made, with acceptance cuts at  $|\eta_{accept}| < 4.45$  and  $|\eta_{accept}| < 4.1$ , the edges of the first two FH layers and the EM region respectively. Both of these analyses produce a small change in the result:  $N_{corr} = 35.1 \pm 7.0$ , which is an increase of 4%.

### Discussion of systematic uncertainties

The large deviations in the number of candidate events when parameters are changed indicate that the analysis is not yet fully understood. This simple Monte Carlo simulation, using particle cuts instead of a full detector simulation, lacks many effects that are present in the data: for example, Fig. 5.25 shows that the  $p_T$  balance in the diffractive candidate events is not correctly modelled in the Monte Carlo. The  $p_T$  balance is  $p_T^Z - p_T^{hadrons}$ , where the hadronic part is measured with the calorimeter cells. Two candidate events are not shown: in one, the  $p_T$  balance is greater than 100 GeV, and in the other, the  $p_x$  and  $p_y$  of the muons is not known. The POMWIG distribution is less broad than the data, and this indicates that further work using a full detector simulation is required before the diffractive  $Z \rightarrow \mu^+\mu^-$  production cross section times branching ratio can be presented. However, the other components of the cross section (Eq. 5.2) are described in the following sections.

#### 5.6.3 Efficiency of rapidity gap requirement

The efficiency of the rapidity gap cut,  $\varepsilon_{gap}$ , in selecting events with  $\xi < 0.02$  is calculated using the POMWIG event sample (Section 5.4). In the pomeron

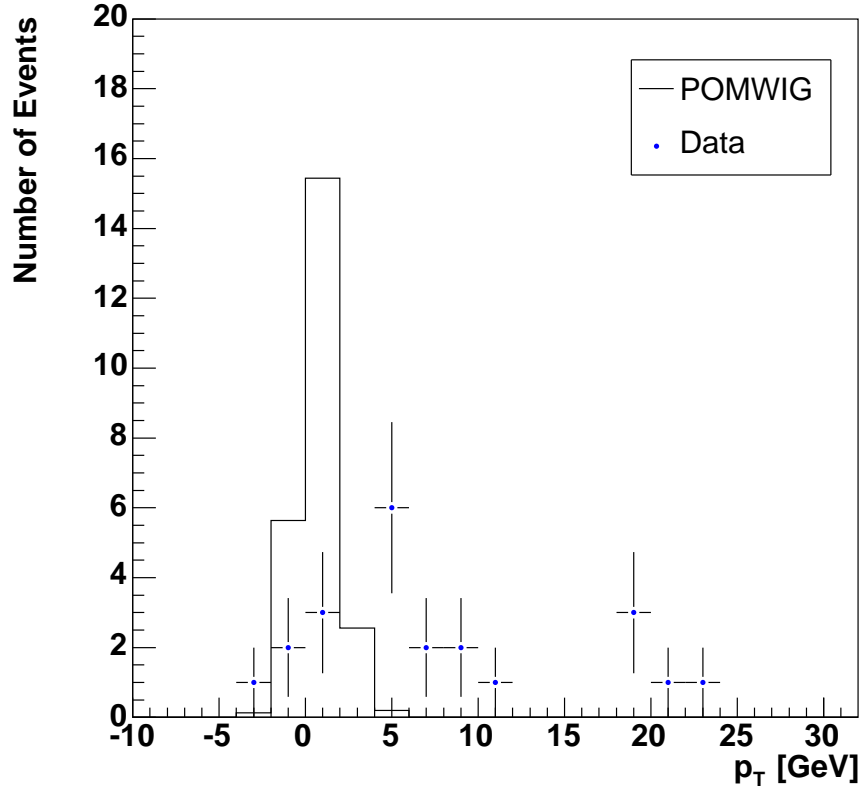


Figure 5.25: Balance of transverse momentum,  $p_T^Z - p_T^{hadrons}$ , for diffractive candidate events, where the hadron  $p_T$  is measured with the calorimeter cells. The POMWIG prediction is shown, scaled to the data distribution.

sample, 90% of the events with  $\xi < 0.02$  have a rapidity gap ( $\eta_{max} < 3.2$  in the particles that pass the acceptance cuts). In the reggeon sample, 77% of events pass the rapidity gap cut. The uncertainties  $\Delta\varepsilon$  are calculated using  $\Delta\varepsilon = \sqrt{\varepsilon(1-\varepsilon)/N}$ , where  $N$  is the total number of events. The results are

$$\varepsilon_{gap}^{IP} = 0.901 \pm 0.003$$

$$\varepsilon_{gap}^{IR} = 0.77 \pm 0.03$$

for the pomeron and reggeon samples respectively. The pseudorapidity distributions of the particles are determined by the pomeron and reggeon structure functions. The default ‘fit 2’ pomeron structure function is used to calculate the value of  $\varepsilon_{gap}^{IP}$  stated above, so as a cross-check  $\varepsilon_{gap}^{IP}$  is calculated using the ‘fit 3’ structure function (Section 2.3). The result is

$$\varepsilon_{gap}^{IP} = 0.916 \pm 0.009 \text{ (fit 3)}$$

which is consistent with the previous measurement.

The efficiencies are combined with

$$\varepsilon_{\text{tot}} = \frac{\varepsilon_{IR} \sigma_{IR} + \varepsilon_{IP} \sigma_{IP}}{\sigma_{IR} + \sigma_{IP}}, \quad (5.3)$$

where the cross sections predicted by POMWIG for the kinematic range of the events,  $\xi < 0.02$ ,  $M > 40$  GeV and with two muons with  $p_T > 15$  GeV and  $|\eta| < 2$ , are

$$\sigma_{IP} = 0.14 \text{ pb}$$

$$\sigma_{IR} = 0.08 \text{ pb}$$

for pomeron and reggeon exchange. The cross section for reggeon exchange is assigned an uncertainty of 50% [60] due to the normalisation of the reggeon flux

(Section 2.3). The result for the rapidity gap efficiency is

$$\varepsilon_{\text{gap}} = 0.85 \pm 0.14 .$$

#### 5.6.4 Efficiency of muon detection

In the inclusive  $Z$  cross section measurement in [56] the ‘efficiency MC’ ( $\varepsilon_{\text{MC}}$ ) combines the geometric acceptance of the muon detector, the efficiency of the cut on muon  $p_T$ , and the efficiencies of the central tracking detector, muon triggers and muon identification criteria. PYTHIA  $(Z/\gamma)^* \rightarrow \mu^+\mu^-$  events are used for the calculation: the vertex  $z$  position in the events is smeared with a Gaussian distribution of width 28 cm; the events are passed through PMCS; and the geometric acceptance and  $p_T$  cuts (Section 5.1.2) are applied to the muon tracks. Muons that pass these cuts are subjected to the efficiencies of the tracking, trigger and muon identification: these are measured in the data as functions, where appropriate, of the muon  $\eta$  and the  $z$ -position of the vertex. Thus a given muon has a particular probability of being selected in the final sample, according to the location and transverse momentum of the central track. The fraction of PYTHIA events that pass these criteria is  $\varepsilon_{\text{MC}}$ ; the result in the inclusive analysis is  $\varepsilon_{\text{MC}} = 0.322 \pm 0.006$ .

This efficiency is re-calculated for this analysis because the muon  $p_T$  and  $\eta$  distributions are different in diffractive  $Z \rightarrow \mu^+\mu^-$  events; the same method is used with POMWIG events [61]. The results are

$$\varepsilon_{\text{MC}}^{\text{IP}} = 0.104 \pm 0.004$$

$$\varepsilon_{\text{MC}}^{\text{IR}} = 0.089 \pm 0.004$$

where the systematic uncertainty from the efficiencies measured in the data is

calculated to be 1.5%. The resulting distributions for the properties of the muons and Z boson candidates are shown in Figs. 5.20 and 5.21.

The cross sections predicted by POMWIG for the kinematic range  $\xi < 0.02$ ,  $M > 40$  GeV are

$$\sigma_{IP} = 0.75 \text{ pb}$$

$$\sigma_{IR} = 0.42 \text{ pb} .$$

As in Section 5.6.3, the efficiencies for the pomeron and reggeon samples are combined using Eq. 5.3, and the uncertainty in the reggeon normalisation is set at 50%, with the result

$$\varepsilon_{MC} = 0.099 \pm 0.016 .$$

Varying the pomeron structure function from fit 2 to fit 3 has negligible effect on this efficiency. This is tested by comparing the pseudorapidity of the muons in events with  $\xi < 0.02$ : the geometric acceptance is the dominant contribution to  $\varepsilon_{MC}$  [62].<sup>2</sup> For the fit 2 structure function, a fraction  $0.538 \pm 0.006$  of the muons have  $|\eta| < 2.0$ ; for the fit 3 structure function, this fraction is  $0.540 \pm 0.007$ , so the two are consistent.

### 5.6.5 Cosmic muon background

Analysis of diffractive  $Z \rightarrow \mu^+\mu^-$  bosons using only rapidity gaps to select the candidates (as in Appendix A) may be susceptible to enhanced background from cosmic ray muons: a cosmic muon can be selected as a Z boson event, and unless there is an overlapping  $p\bar{p}$  interaction then the event has no activity in the

---

<sup>2</sup> A calculation of  $\varepsilon_{MC}$  using the fit 3 sample was not available.

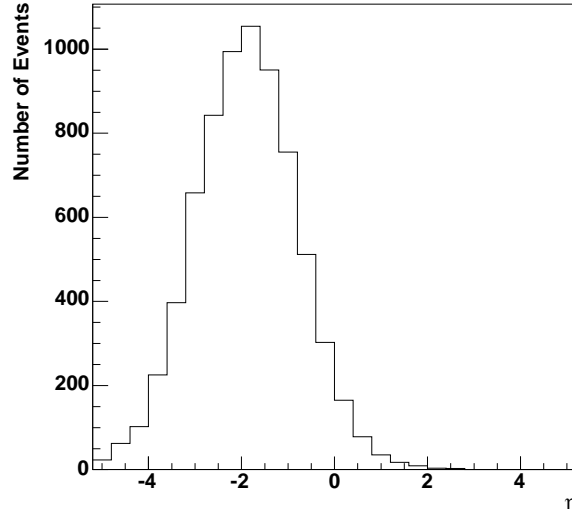


Figure 5.26: Pseudorapidity of two highest  $p_T$  muons in POMWIG  $Z \rightarrow \mu^+\mu^-$  events with  $\xi < 0.02$ : the geometric acceptance of the muon detector is approximately  $|\eta| < 2$

calorimeter and passes the rapidity gap requirement. However, it is expected that a diffractive sample selected using the  $\xi$  variable will not have this background due to the kinematic requirements (in other words, forward muons) of reconstructing a low  $\xi$ .

The acolinearity of the muon pair in the diffractive candidate events is shown in Fig. 5.27. All of the events have large acolinearity, well above the threshold of  $\Delta\alpha_{\mu\mu} = 0.05$  radians to exclude cosmic ray muons. The cosmic background rate  $f_{cos}$  is assumed to be the same as that of the inclusive sample [56]:

$$f_{cos} = 0.002 \pm 0.002 ,$$

which in this sample is negligible.



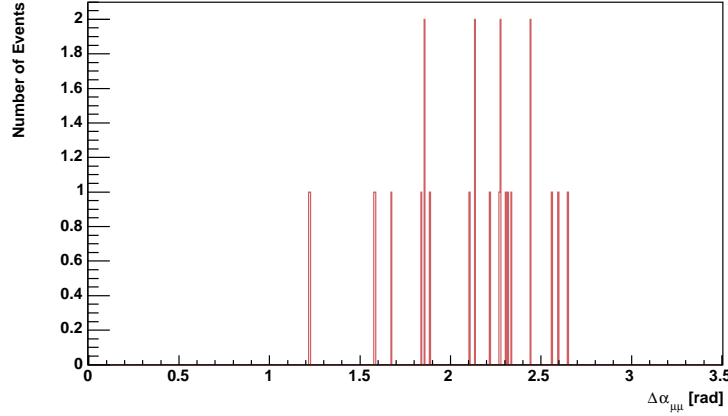


Figure 5.27: Acolinearity of the dimuon pair in diffractive  $Z \rightarrow \mu^+\mu^-$  candidate events

### 5.6.6 Other efficiencies and backgrounds

All other efficiency and background factors, which are listed in Table 5.3, are taken directly from the inclusive measurement. These are the efficiencies for the isolation cuts ( $\epsilon_{\text{isol}}$ ), cosmic cuts ( $\epsilon_{\text{cosmic}}$ ) and the requirement that the muons are oppositely charged ( $\epsilon_{\text{opp-}q}$ ), and the background fractions from  $b\bar{b}$  events ( $f_{b\bar{b}}$ ),  $Z \rightarrow \tau\tau$  events ( $f_{\tau\tau}$ ),  $W$ +jets and diboson events ( $f_W$ ). The background fraction for cosmic ray muons,  $f_{\text{cos}}$ , (Section 5.6.5) is also included in the table. The efficiencies are all extremely high with respect to  $\epsilon_{\text{gap}}$  and  $\epsilon_{\text{MC}}$ , and the background rates are low, but it is useful to include them for completeness.

Quantity	Value
$\mathcal{E}_{\text{isol}}$	$0.999 \pm 0.001$
$\mathcal{E}_{\text{cosmic}}$	$0.988 \pm 0.006$
$\mathcal{E}_{\text{opp-q}}$	$0.998 \pm 0.001$
$f_{\text{bb}}$	$0.005 \pm 0.003$
$f_{\text{cosmic}}$	$0.002 \pm 0.002$
$f_{\tau\tau}$	$0.005 \pm 0.001$
$f_W$	$0.002 \pm 0.001$

Table 5.3: Efficiencies and backgrounds taken from the inclusive  $Z \rightarrow \mu^+ \mu^-$  cross section

## 5.7 Result

### 5.7.1 Corrected number of candidates

Combining the efficiencies and backgrounds with the corrected number of candidates, using:

$$N_{\text{total}} = N_{\text{corr}} \times \frac{(1 - f_{\text{bb}} - f_{\text{cos}}) (1 - f_{\tau\tau}) (1 - f_W)}{\mathcal{E}_{\text{gap}} \mathcal{E}_{\text{MC}} \mathcal{E}_{\text{opp-q}} \mathcal{E}_{\text{isol}} \mathcal{E}_{\text{cosmic}}}$$

yields a prediction of  $400.9 \pm 81.8$  (stat.) for the total number of candidates for an integrated luminosity [63] of  $\int \mathcal{L} dt = 109 \pm 7 \text{ pb}^{-1}$ . However, the systematic uncertainties are large and as yet undetermined so the cross section is not presented.

### 5.7.2 Contribution from non-diffractive events

The contribution from non-diffractive events,  $\sigma_{nd}$ , is estimated using simulated  $(Z/\gamma)^* \rightarrow \mu^+\mu^-$  events with  $M_{\mu\mu} > 40$  GeV from the PYTHIA event generator. HERWIG is not used because of the excess production of rapidity gaps in the final state (Section 5.3). The acceptance cuts are applied to particles in the PYTHIA events as described in Section 5.3.1. The rapidity gap requirement is made,  $|\eta_{max}| < 3.2$  in the proton or antiproton direction, and 1% of the events pass this cut. The reconstructed momentum loss,  $\xi_{reco}$ , is calculated and the same correction factors are applied to the events as they are in the data (Section 5.5).

Figure 5.28 shows the distribution of  $\xi$  in events that pass the rapidity gap cut: 10% have  $\xi < 0.02$ , or 0.1% of the sample. The PYTHIA prediction for the cross section for  $(Z/\gamma)^* \rightarrow \mu^+\mu^-$  events with  $M_{\mu\mu} > 40$  GeV is 202 pb, giving a predicted non-diffractive contribution of  $\sigma_{nd} = 0.2$  pb.

The inclusive cross section is measured using the full data sample, with 10791 candidates (the effect of excluding three events with no calorimeter information is negligible), and  $\varepsilon_{MC}$  taken from the previous analysis [56]. The result is

$$\sigma \times \text{Br}((Z/\gamma)^* \rightarrow \mu^+\mu^-) = 308 \pm 3 \text{ (stat.)} \pm 6 \text{ (sys.)} \pm 20 \text{ (lumi.) pb}$$

which is consistent with the result in [56]. The PYTHIA prediction is scaled by the ratio of the PYTHIA and data inclusive cross sections,  $R = 308/202$ , so the prediction for the non-diffractive contribution is

$$\sigma_{nd} = 0.3 \pm 0.1 \text{ pb}$$

where the uncertainty is assigned from the difference between the PYTHIA and data inclusive cross sections. For a luminosity of  $109 \text{ pb}^{-1}$ , this predicts 32.7

candidate events: about 8% of the number of candidates in Section 5.7.1.

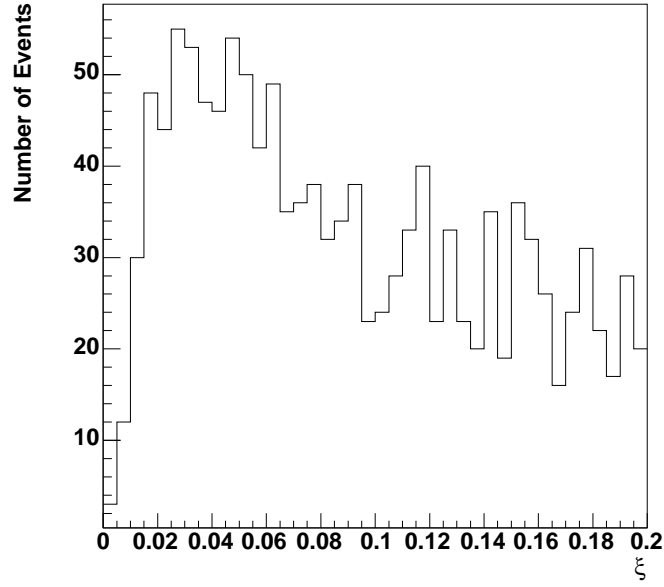


Figure 5.28: Reconstructed  $\xi$  distribution in PYTHIA non-diffractive  $Z \rightarrow \mu^+\mu^-$  events

## 5.8 Discussion

### POMWIG prediction

The POMWIG prediction for the cross section times branching ratio in this kinematic region, with no gap survival probability included, is:

$$\sigma_{MC} = (1.2 \pm 0.2) \text{ pb}$$

where the uncertainty is due to the reggeon cross section normalisation. This is about 0.4% of the measured inclusive cross section. The diffractive  $W$  and  $Z$

boson analyses at DØ and CDF indicate that the fraction of diffractive candidates is around 1% (Section 2.2.2), which is reasonably consistent with the POMWIG prediction given that the kinematic region of these measurements is not defined. But POMWIG does not include gap survival probability, so the naïve expectation is that the complete prediction would be about 10 times smaller. The gap survival probability is not known for diffractive electroweak processes, but it seems that POMWIG may not predict a sensible order of magnitude for the cross section times branching ratio.

The gap survival factor  $s \sim 0.1$  is determined from dijet cross section measurements. Diffractive dijet production and diffractive  $Z$  boson production couple differently to the gluon and quark components of the pomeron (Section 2.3), so a measurement of this cross section at the Tevatron would be the first to directly probe the quark component. This is the first time diffractive electroweak boson production data has been compared with POMWIG. The POMWIG prediction and the factor for the gap survival probability are open questions: this makes diffractive  $Z$  boson production an interesting channel, with the potential to be a sensitive probe for the answers. In addition, it may be possible to measure the normalisation of the reggeon flux through the differential cross section with respect to  $\xi$ .

### **Soft dissociation of the proton**

In order to fully specify the kinematic range of the cross section measurement, it is necessary to know the minimum proton dissociative mass which can be seen in the forward DØ detectors. At H1, this was  $M = 1.6$  GeV: at lower masses the proton final state is not observed. Neither PYTHIA nor POMWIG prediction

models this type of event, in which the proton dissociates and there is a rapidity gap, and in fact a good understanding of this contribution would require detailed MC studies which are currently not available. Therefore the presented diffractive  $Z \rightarrow \mu^+\mu^-$  candidates could include events in which there is proton dissociation into low mass states.

### **Choice of pomeron structure function**

Changing the pomeron structure function from fit 2 to fit 3 made no discernable difference to the calculated efficiencies  $\varepsilon_{gap}$  and  $\varepsilon_{MC}$ . This is expected, because the variation is predominantly in the gluon component which is not strongly probed in diffractive  $Z$  boson production.

### **Analysis of $Z \rightarrow \mu^+\mu^-$ using rapidity gaps**

Previous to the analysis presented in this thesis, the author carried out an analysis of diffractive  $Z$  boson production that used the rapidity gap method to select candidate events [47]. The method used cannot lead to a normalised cross section measurement in a clear kinematic region. The rapidity gap requirement was made using a sum over energy in the forward calorimeter, confirmed by the absence of hits in the LM detector. No corrections were made to the result; these would require a good description of the calorimeter and LM detector in the detector simulation, which is not yet available at DØ. In addition, using the LM to confirm the gap is prone to difficulties: the detector terms are prone to ‘electronics inefficiency’ which results in fake gap signals (Section 4.3); the detectors are sensitive to beam halo particles; and the fixed pseudorapidity range does not allow variation in the

choice of kinematic region. As previously mentioned (Section 5.6.5), a rapidity gap analysis of  $Z \rightarrow \mu^+ \mu^-$  also appears to be more susceptible to background from cosmic ray muons. A description of the analysis is included in Appendix A in the form of conference proceedings written by the author.

### **Future steps in the analysis**

This analysis has made the first steps towards a measurement of a diffractive cross section at DØ. It has made progress in understanding the requirements of the analysis, and identified some of the largest uncertainties: the measurement of the rapidity gap boundary, the correction for the cell energy threshold, the uncertainty due to the reggeon normalisation and the calibration of the calorimeter. The future development of the analysis is discussed below.

The analysis should be carried out with the full DØ detector simulation, providing the low-level calorimeter energy is sufficiently well modelled to be useful. Further studies of the effect of using  $\eta_{max}^{2nd}$  would certainly decrease the uncertainty. The approach could be to make a more sophisticated gap boundary cut, perhaps requiring that two cells are close in pseudorapidity or are in the same tower to define the boundary; it may be useful to examine the additional candidates from the  $\eta_{max}^{2nd}$  analysis (perhaps also  $\eta_{max}^{3rd}$  and  $\eta_{max}^{4th}$ ) to separate the diffractive candidates from the fake gap events. The full detector simulation may help with this, as it was found in the LM acceptance studies (Section 4.2.2) that particles in diffractive events could scatter into the gap from detector components. Future analyses will be able to make use of an improved calorimeter calibration with known uncertainties. Although the hot cell killing algorithm did not appear to affect the results, it is felt that the algorithm is still useful; with a larger dataset and reduced

uncertainties there may be a discernable difference to the measurement. It may be a helpful tool for probing the uncertainty due to the rapidity gap boundary ( $\eta_{max}^{2nd}$ ).

A model of the soft dissociation of the proton would strengthen the measurement, correcting for rapidity gap events in which the proton dissociates into a low mass state and yielding a cross section for  $Z$  boson production with an intact proton.

The choice of kinematic region may be improved, a decision that might best be made after the size of the dataset is increased. Increasing the  $\xi$  threshold would decrease the statistical uncertainties and increase the muon identification efficiency  $\varepsilon_{MC}$ . It would, however, decrease the efficiency of the rapidity gap cut and decrease the pomeron component of the sample. Ideally, with a larger dataset and detailed studies of the efficiencies as a function of  $\xi$ , the measurement  $d\sigma/d\xi$  could be presented.

As a result of the findings in this analysis (Section 5.3), the authors of POMWIG intend to interface the generator with the JETSET hadronisation model used by PYTHIA [52].

## Summary

The first analysis of diffractive  $Z$  bosons in the muon decay channel has been presented, including a comparison of the data with POMWIG. The uncertainties are prohibitively large for a measurement of the cross section times branching ratio, but it is hoped that components of the analysis that have been developed can be used as building blocks in future diffractive analyses at DØ: in particular, the measurement of  $\xi$  from the final state system, the comparison of data with POMWIG and the estimate of the non-diffractive contribution to the low  $\xi$  sample. Measure-



ment of the diffractive  $Z$  boson production cross section could give interesting results with regard to gap survival probability in diffractive electroweak boson production and the validity of transferring the H1 diffractive pdfs to the Tevatron.

# Chapter 6

## Summary

The first part of the thesis, presented in Section 4, provides the first measurement of the efficiency of the DØ Luminosity Monitor, which is used in normalising all cross section measurements. The result is:

$$\varepsilon_{LM} = (90.9 \pm 1.8)\% .$$

The second part (Section 5) presents the first steps towards measuring the  $(Z/\gamma)^*$  boson production cross section times branching ratio in the kinematic region  $\xi < 0.02$ , which is dominated by diffractive exchange. A sample of 24 candidate events are selected, and the data are compared with the Monte Carlo event generator POMWIG. Each component of the cross section is studied, and the systematic uncertainties in the number of candidates are found to be too large and poorly understood to allow the measurement of a cross section.

# Appendix A

## Diffractive Scattering at DØ

The following appendix contains extracts from a conference paper submitted by the author [47], which describes the previous method of searching for diffractively produced  $Z$  bosons in the muon decay channel.

### Abstract

The first search for diffractively produced  $Z$  bosons in the muon decay channel is presented, using a data set collected by the DØ detector at the Fermilab Tevatron at  $\sqrt{s} = 1.96$  TeV between April and September 2003, corresponding to an integrated luminosity of approximately  $110 \text{ pb}^{-1}$ .

### A.1 Introduction

QCD models elastic and single diffractive scattering of hadrons as proceeding via the exchange of a colour singlet object. In the case of elastic proton-antiproton scattering, both protons<sup>1</sup> emerge intact and scattered at a small angle, with no

---

<sup>1</sup> Here the term ‘proton’ is used to refer to both protons and antiprotons.

momentum loss and no other particles produced. In single diffraction, where one proton remains intact with a small momentum loss and the other dissociates, there may be an area devoid of activity (rapidity gap) in the region of the outgoing intact proton. We present here the first ever search for diffractively produced  $Z$  bosons in the muon decay channel.

## A.2 Diffractive $Z$ boson production

### A.2.1 Event selection and data analysis

$Z$  bosons produced via single diffraction are identified by demanding a rapidity gap near the beampipe in either the outgoing proton or antiproton direction. The data set was collected between April and September 2003 by the DØ detector at the Fermilab Tevatron, corresponding to an integrated luminosity of approximately  $110 \text{ pb}^{-1}$ . The DØ detector is described in detail elsewhere [44]. The  $Z$  boson is selected via its decay into two oppositely charged muons each with  $p_T > 15 \text{ GeV}$ . At least one muon must be isolated in the central tracking detector and the calorimeter:  $\Sigma p_T$  of tracks within a cone of radius 0.5 around the muon is required to be less than 3.5 GeV, and in the calorimeter ( $\Sigma E_T$  in a cone of radius of 0.5 around the muon) - ( $\Sigma E_T$  in a cone of radius of 0.1 around the muon) is required to be less than 2.5 GeV, where the cone radius is defined in pseudorapidity  $\eta$  and azimuthal angle  $\phi$  as  $\Delta R = \sqrt{\Delta\eta^2 + \Delta\phi^2}$ . Cosmic ray muon events are vetoed by requiring that the distance of closest approach of muon tracks to the beam position is less than 0.02 cm for tracks with hits in both the Silicon Microvertex Tracker (SMT) and Central Fiber Tracker (CFT), or less than 0.2 cm for tracks with hits only in the CFT. In addition, the muon tracks are required to fulfil  $|\Delta\phi_{\mu\mu} + \Delta\theta_{\mu\mu} - 2\pi| > 0.05$  radians, where  $\theta$  is polar angle.

The rapidity gap search makes use of two detectors, the Luminosity Monitor (LM) and the end calorimeter. The LM comprises two scintillating detectors, one on each side of the interaction region, which cover the pseudorapidity range  $2.7 < |\eta| < 4.4$ . The total output charge is discriminated to give an on/off signal for each detector. The end calorimeter is divided into three regions: (1) four electromagnetic layers closest to the beam, (2) four fine hadronic layers and (3) one coarse hadronic layer furthest from the beam. Each layer is divided into cells in the  $\eta - \phi$  plane. For this analysis, the energy is summed separately on each side (outgoing proton and antiproton) in the range  $2.6 < |\eta| < 5.3$ , using electromagnetic cells with  $E_{\text{cell}} > 100$  MeV and fine hadronic cells with  $E_{\text{cell}} > 200$  MeV.

The log of the energy sum on the outgoing antiproton side is plotted in Figure A.1 for bunch crossings in which there are no visible interactions. These are selected from a randomly triggered sample with the requirements that both LM detectors are off and there is no vertex with greater than two associated tracks. These events are used to approximate rapidity gap events, in which there is no activity in the outgoing antiproton direction. The log of the energy sum on the outgoing antiproton side is also shown for a sample of minimum bias events in the figure. These are selected requiring hits in both detectors of the LM within a small time window. A third (25 GeV jet) sample is selected by requiring a vertex with at least three tracks, and at least one jet with  $p_T > 25$  GeV that passes jet quality cuts. Jet events in which the highest  $p_T$  jet lies in the region  $|\eta| > 2.4$  are excluded. The minimum bias and jet samples are dominated by events in which both protons dissociate.

Events with no interaction and events with antiproton dissociation are separated by applying a cut at an energy sum of 10 GeV. This is also the case in the outgoing proton direction. To select single diffractive candidates in the Z boson sample the LM detector is required to be off and the energy sum less than 10 GeV on one

side, and the LM detector is required to be on and the energy sum greater than 10 GeV on the other side.

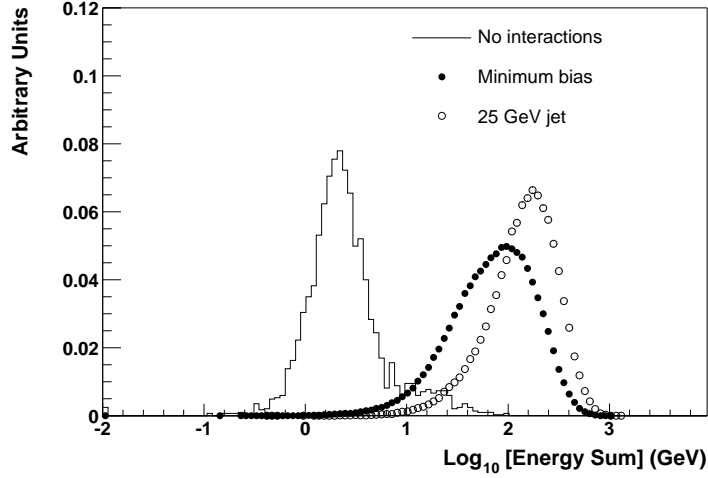
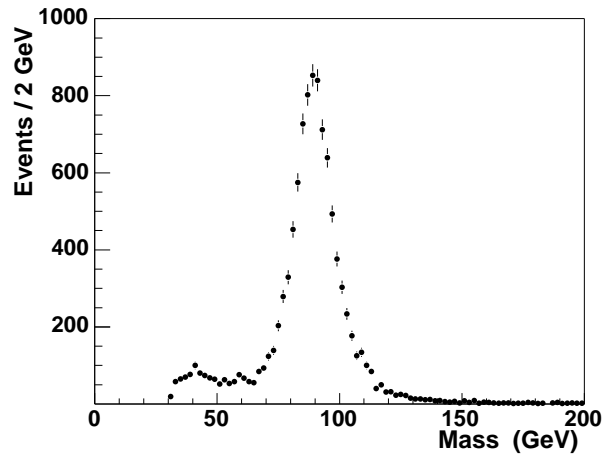


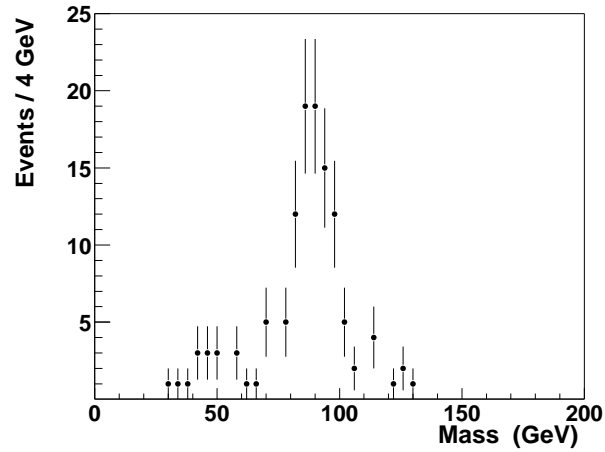
Figure A.1: Log of energy sum in the outgoing antiproton direction ( $-5.3 < \eta < -2.6$ ), comparing events with no visible interactions with events in which both protons dissociate. Areas are normalised to unity. An energy sum cut is applied at 10 GeV for rapidity gap candidates.

## A.2.2 Results

Figure A.2 shows the di-muon invariant mass distribution for two samples. Fig. A.2(a) shows those events that fail the two rapidity gap cuts on both the outgoing proton and antiproton sides. These are strong candidates for non-diffractive production of  $Z$  bosons. A resonant peak is observed together with a small background contribution, arising mainly from the  $(Z/\gamma)^*$  continuum. Fig. A.2(b) shows those events that pass both rapidity gap cuts on one side and fail both on the other. These are candidates for single diffractively produced  $Z$  bosons, where one proton is intact and the other dissociates.



(a)



(b)

Figure A.2: The dimuon invariant mass distribution for Z boson candidates with (a) no rapidity gap and (b) a single rapidity gap. A rapidity gap is defined as one LM detector off and energy sum less than 10 GeV in the same region (see text for details).

## Summary

A search for diffractively produced  $Z$  bosons in the muon channel has been presented. The sample is large enough to allow a study of the kinematic properties of the  $Z$  bosons for the first time.



# Bibliography

- [1] J. Breitweg *et al.* [ZEUS Collaboration], Eur. Phys. J. C **12** (2000) 411 [Erratum-ibid. C **27** (2003) 305] [arXiv:hep-ex/9907010].
- [2] C. Adloff *et al.* [H1 Collaboration], Eur. Phys. J. C **30** (2003) 1 [arXiv:hep-ex/0304003].
- [3] J. C. Collins, Phys. Rev. D **57** (1998) 3051 [Erratum-ibid. D **61** (2000) 019902] [arXiv:hep-ph/9709499].
- [4] C. Adloff *et al.* [H1 Collaboration], Z. Phys. C **76** (1997) 613 [arXiv:hep-ex/9708016].
- [5] M. Derrick *et al.* [ZEUS Collaboration], Z. Phys. C **70** (1996) 391 [arXiv:hep-ex/9602010].
- [6] B. E. Cox, K. Goulianos, L. Lonnblad and J. J. Whitmore, J. Phys. G **26** (2000) 667 [arXiv:hep-ph/0001110].
- [7] B. E. Cox, AIP Conf. Proc. **753** (2005) 103 [arXiv:hep-ph/0409144].
- [8] V. A. Khoze, A. B. Kaidalov, A. D. Martin, M. G. Ryskin and W. J. Stirling, arXiv:hep-ph/0507040.
- [9] J. R. Forshaw, arXiv:hep-ph/0508274.
- [10] V. M. Abazov *et al.* [D0 Collaboration], Phys. Lett. B **574**, 169 (2003) [arXiv:hep-ex/0308032].
- [11] G. F. P. Chew and S. C. Frautschi, Phys. Rev. Lett. **7** (1961) 394.
- [12] M. Gell-Mann, Phys. Lett. **8** (1964) 214.
- [13] Y. Nambu, Preludes in Theoretical Physics in Honor of V. F. Weisskopf, ed. by A. De-Shalit, H. Feshbach, and L. Van Hove, North-Holland, Amsterdam, (1966) 133 (1966).

- [14] J. R. Forshaw and D. A. Ross, Cambridge University Press (1997).
- [15] B. E. Cox, PhD thesis, University of Manchester (1998).
- [16] T. Regge, *Nuovo Cim.* **14** (1959) 951.
- [17] T. Regge, *Nuovo Cim.* **18** (1960) 947.
- [18] David Kaiser, *Isis* 93 (June 2002), pp. 229-268: in press.
- [19] G. F. P. Chew and S. C. Frautschi, *Phys. Rev. Lett.* **8** (1962) 41.
- [20] I. Y. Pomeranchuk, *ZhETF* **30** (1956) 423 (SW, **3**, 106); I. Y. Pomeranchuk and L. B. Okun, *ZhETF* **30** (1956) 424 (SW, **3**, 107).
- [21] L. B. Okun, arXiv:physics/0307123.
- [22] I. Y. Pomeranchuk, *Zh. Eksp. Teor. Fiz.* **34** (1958) 725.
- [23] Y. L. Dokshitzer and D. E. Kharzeev, arXiv:hep-ph/0404216.
- [24] A. Donnachie and P. V. Landshoff, *Phys. Lett. B* **296** (1992) 227 [arXiv:hep-ph/9209205].
- [25] S. Donnachie, *CERN Courier* **39** No. 3 (Apr. 1999).
- [26] C. Adloff *et al.* [H1 Collaboration], *Nucl. Phys. B* **497** (1997) 3 [arXiv:hep-ex/9703012]; J. Breitweg *et al.* [ZEUS Collaboration], *Phys. Lett. B* **407** (1997) 432 [arXiv:hep-ex/9707025].
- [27] A. Donnachie and P. V. Landshoff, *Phys. Lett. B* **437** (1998) 408 [arXiv:hep-ph/9806344].
- [28] J. D. Bjorken, SLAC-PUB-6949.
- [29] S. Abatzis *et al.* [WA91 Collaboration], *Phys. Lett. B* **324** (1994) 509.
- [30] D. Barberis *et al.* [WA102 Collaboration], *Phys. Lett. B* **432** (1998) 436 [arXiv:hep-ex/9805018].
- [31] J. C. Collins, arXiv:hep-ph/9705393.
- [32] F. Abe *et al.* [CDF Collaboration], *Phys. Rev. Lett.* **78** (1997) 2698 [arXiv:hep-ex/9703010].
- [33] B. E. Cox and J. R. Forshaw, *Comput. Phys. Commun.* **144** (2002) 104.

- [34] G. Ingelman and P. E. Schlein, Phys. Lett. B **152** (1985) 256.
- [35] J. F. Owens, Phys. Rev. D **30** (1984) 943.
- [36] P. Bruni and G. Ingelman, Phys. Lett. B **311** (1993) 317.
- [37] E. Gotsman, E. Levin and U. Maor, Phys. Rev. D **60** (1999) 094011 [arXiv:hep-ph/9902294].
- [38] V. A. Khoze, A. D. Martin and M. G. Ryskin, Eur. Phys. J. C **14** (2000) 525 [arXiv:hep-ph/0002072].
- [39] A. B. Kaidalov, V. A. Khoze, A. D. Martin and M. G. Ryskin, Eur. Phys. J. C **21** (2001) 521 [arXiv:hep-ph/0105145].
- [40] B. Cox, J. Forshaw and B. Heinemann, Phys. Lett. B **540** (2002) 263 [arXiv:hep-ph/0110173].
- [41] B. E. Cox and A. Pilkington, arXiv:hep-ph/0508249.
- [42] R. Fernow, *Introduction to experimental particle physics*, Cambridge University Press, 1992.
- [43] S. Mishra, FERMILAB-CONF-03-194, *Presented at Particle Accelerator Conference (PAC 03), Portland, Oregon, 12-16 May 2003*.
- [44] V. M. Abazov *et al.* [DØ Collaboration], submitted to Nucl. Instrum. Meth. A; T. LeCompte and H. T. Diehl, Ann. Rev. Nucl. Part. Sci. **50** (2000) 71 [arXiv:physics/0507191].
- [45] J.-R. Vlimant, U. Bassler, G. Bernardi, S. Trincas-Duvoid, DØ Note 4146.
- [46] A. Brandt *et al.* [DØ Collaboration], FERMILAB-PUB-97-377.
- [47] T. Edwards [DØ Collaboration], Apr 2004. 6pp. Published in \*Strbske Pleso 2004, Deep inelastic scattering\* 466-471.
- [48] R. Schwienhorst [DØ Collaboration], Int. J. Mod. Phys. A **20** (2005) 3796 [arXiv:physics/0411135].
- [49] T. Edwards *et al.*, DØ Note 4504.
- [50] T. Edwards *et al.* [DØ Collaboration], FERMILAB-TM-2278-E.
- [51] S. Klimenko, J. Konigsberg and T. M. Liss, FERMILAB-FN-0741.
- [52] T. Sjostrand, Comput. Phys. Commun. **82** (1994) 74.

- [53] K. Goulianos, private communication.
- [54] H. Schellman *et al.*, DØ Note 4292.
- [55] B. Casey, private communication.
- [56] E. L. Nurse, FERMILAB-THESIS-2005-05
- [57] M. A. Strang, FERMILAB-THESIS-2005-23
- [58] C. Adloff *et al.* [H1 Collaboration], Eur. Phys. J. C **24** (2002) 517 [arXiv:hep-ex/0203011].
- [59] J. Stark, private communication.
- [60] B. E. Cox, private communication.
- [61] P. Telford, PhD thesis, University of Manchester (in preparation).
- [62] P. Telford, private communication.
- [63] M. Verzocchi, private communication.
- [64] J. Molina and V. Oguri, Nov 2002. Available at:  
<[http://alpha1.lafex.cbpf.br/~molina/elastic\\_mc/](http://alpha1.lafex.cbpf.br/~molina/elastic_mc/)>
- [65] J. Barreto and J. Montanha, Jan 2003. Available at:  
<[http://www.ifi.unicamp.br/~montanha/fpd/sources/quadrupoles/pot\\_ver.for](http://www.ifi.unicamp.br/~montanha/fpd/sources/quadrupoles/pot_ver.for)>
- [66] A. I. Drozhdin *et al.*, FERMILAB-FN-0734.
- [67] A. Breakstone *et al.* [AMES-BOLOGNA-CERN-DORTMUND-HEIDELBERG-WARSAW Collaboration], Nucl. Phys. B **248**, 253 (1984);  
A. Breakstone *et al.*, Phys. Rev. Lett. **54**, 2180 (1985);  
R. Battiston *et al.* [UA4 Collaboration], Phys. Lett. B **127**, 472 (1983);  
M. Bozzo *et al.* [UA4 Collaboration], Phys. Lett. B **155**, 197 (1985);  
D. Bernard *et al.* [UA4 Collaboration], Phys. Lett. B **171**, 142 (1986);  
N. A. Amos *et al.* [E-710 Collaboration], Phys. Lett. B **247**, 127 (1990).
- [68] M. Block *et al.*, Phys. Rev. D **41**, 978 (1990).